COMPUTATIONAL MODELING AND SIMULATIONS
OF HYDRODYANMICS FOR AIR-WATER
EXTERNAL LOOP AIRLIFT REACTORS

by

Deify Law

Dissertation submitted to the faculty of the Virginia Polytechnic Institute and State University in partial fulfillment of the requirements for the degree of

Doctor of Philosophy
In

Mechanical Engineering

Francine Battaglia, Committee Chair
Eugene F. Brown, Committee Member
Theodore J. Heindel, Committee Member
Mark A. Stremler, Committee Member
Pavlos P. Vlachos, Committee Member

May 27, 2010

Blacksburg, Virginia

COMPUTATIONAL MODELING AND SIMULATIONS OF HYDRODYNAMICS FOR AIR-WATER EXTERNAL LOOP AIRLIFT REACTORS

Deify Law

ABSTRACT

External loop airlift reactors are widely used for biochemical applications such as syngas fermentation and wastewater treatment. To further understand the inherent gas-liquid flow physics within the reactors, computational modeling and simulations of hydrodynamics for air-water external loop airlift reactors were investigated. The gas-liquid flow dynamics in a bubble column were simulated using a FORTRAN code developed by Los Alamos National Laboratory, CFDLib, which employs an Eulerian-Eulerian ensemble averaged method. A two-dimensional Cartesian coordinate system was used to conduct an extensive grid resolution study; it was found that grid cells smaller than the bubble diameter produced unstable solutions. Next, closure models for drag force and turbulent viscosity were investigated for a simple bubble column geometry. The effects of using a bubble pressure model and two drag coefficient models, the White model and the Schiller-Naumann model, were investigated. The bubble pressure model performed best for homogeneous (low velocity) flows and the Schiller-Naumann model was best for all flow regimes. Based on the studies for bubble column flows, an external loop airlift reactor was simulated using both two- and three-dimensional coordinates and results for gas holdup and riser velocity agreed better with experimental data for the 3D simulations. It was concluded that when performing 2D and 3D simulations, care must be taken when specifying the effective bubble diameter size, especially at high flow rates.

Population balance models (PBM) for bubble break-up and coalescence were implemented into CFDLib, validated with experiments, and simulated for the external loop airlift reactor at high inlet superficial gas velocities. The PBM predictions for multiple bubble sizes were comparable with the single bubble size simulations; however, the PBM simulations better predicted the formation of the gas bubble in the downcomer. The 3D PBM simulations also gave better predictions for the average bubble diameter size in the riser. It was concluded that a two-dimensional domain is adequate for gas-liquid flow simulations of a simple bubble column geometry, whereas three-dimensional simulations are required for the complex airlift reactor geometry. To conclude, a two-fluid Eulerian-Eulerian model coupled with a PBM is needed for quantitative as well as physical predictions of gas-liquid external loop airlift reactor flows at high inlet superficial gas velocities.

ACKNOWLEDGEMENTS

TABLE OF CONTENTS

LIST OF FIGURES

LIST OF TABLES

CHAPTER 1. INTRODUCTION

1.1. Background and Motivation

Multiphase flows are ubiquitous phenomena that commonly occur in science, industry, and everyday life [1]. For instance, multiphase flows occur in vaporized gas emitted from vehicle exhaust, synthesis gas fermentation, wastewater treatment, combustion or gasification of coal, and chemical vapor deposition in the semiconductor industries. Multiphase flows, which are generated by a mixture of different materials or different phases of the same material, are defined here as flows exhibiting interpenetrating motion on a macroscopic scale. The interpenetrating motion is inherently accompanied by fluctuations in the velocity and pressure that have an important effect on the mean flow behavior [1].

The subject of this dissertation, hydrodynamics of gas-liquid flows, is a subset of multiphase flows, referred to as two-phase flows. Gas-liquid flows encompass numerous industrial applications within agricultural, biochemical, chemical, electronic, and pharmaceutical industries. For example, one significant application involves bioreactors, which are used to treat waste water or manufacture synthesis gas products for use in alternative energy. The bioreactor configuration may be as simple as a bubble column reactor (section 1.1.1) or complex as an airlift reactor (section 1.1.2). Despite its widespread use in industrial applications, the dynamics of gas-liquid flow in a bioreactor is not well characterized. A better understanding about the inherent physics of gas-liquid flow is paramount for a reliable design of a bioreactor. Academic and industrial researchers have

studied the flow dynamics and characteristics of gas-liquid flows inside bioreactors over the past decades. The following sections describe the basic physics and underlying issues of these reactors.

1.1.1. Bubble Columns

Bubble column reactors are widely used in the chemical industry due to their simple construction without internals or moving parts, excellent heat and mass transfer capabilities, and effective mixing between the gas and liquid phases with low energy consumption, as the gas phase serves the dual function of aeration and agitation. As reactors, they are used in a variety of chemical processes, such as Fischer-Tropsch synthesis, manufacture of fine chemicals, oxidation and alkylation reactions, effluent treatment, coal liquefaction, and fermentation reactions [2]. A schematic of the bubble column is shown in Figure 1.1a as a single column reactor where the mixing processes mostly occur. The reactor is usually filled with quiescent liquid initially, also known as a semi-batch bubble column, and a gas is aerated through the bottom perforated plate. Dispersed bubbles form in the continuous liquid phase that enhances heat and mass transfer between phases.

Bubble column hydrodynamics have been studied experimentally and computationally for scale-up and design considerations. The performance of bubble column reactors depends on the gas holdup (gas volume fraction), bubble size, bubble rise velocity, bubble-bubble interactions, and mixing rate [3]. Joshi [3] published a review paper discussing the modeling efforts on the hydrodynamics of bubble column reactors published in the last 30 years, with relatively more focus on the last 10 years. He stated that the present status of the design of bubble column reactors is closer to an art than science. This is basically because of the complexity of gas-liquid flow dynamics in these devices. Although

bubble columns are widely applied in the chemical, biochemical fermentation, and biological waste water treatment, solid microorganisms may not be suspended homogeneously at low superficial gas velocity for three-phase bubble columns. This situation can be improved by recirculation of the liquid in the bubble columns, which is a design feature of airlift reactors.

1.1.2. Airlift Reactors

Airlift reactors are essentially modified bubble columns. They exhibit the same advantages as conventional bubble columns and offer additional advantages. The most remarkable advantage of the airlift reactor is the control over liquid circulation so as to reduce the back-mixing of liquid in the reactor. The well-directed liquid circulation pattern obtained in airlift reactors reduces the liquid shear stress, thus facilitating the cultivation of shear sensitive organisms; as a result these reactors are widely used in the biochemical industry and for waste water treatment. For example, the internal (ILALR) and external (ELALR) loop airlift reactors are used in the synthesis gas fermentation process in which biomass is converted to useful bio-based products for the replacement of petroleum-based products with biobased products. Figures 1.1 (b) and (c) show schematics of the ILALR and ELALR, respectively.

The ILALR is made up of a draught tube or internals (e.g., baffles) in the bubble column reactor and its flow characteristics are in-between the performance of the bubble column and ELALR. The ELALR is composed of two vertical columns that are joined together with horizontal connectors to form a loop. Gas is introduced in the form of bubbles in the bottom of the main column, called the riser, to induce mixing between the gas and liquid phases. The gas will enter the second vertical column, namely the downcomer section, through the connector. The gas then travels to the bottom of the reactor where it re-enters the

riser as the liquid phase circulates continuously around the loop.   The liquid circulation is induced by higher gas holdup in the riser than downcomer that causes ensemble density difference between the riser and downcomer and acts as a driving force for the liquid flow.

Riser

Downcomer

Bubble

Baffle

Liquid

Gas inflow

(a) Bubble Column   (b) ILALR   (c) ELALR
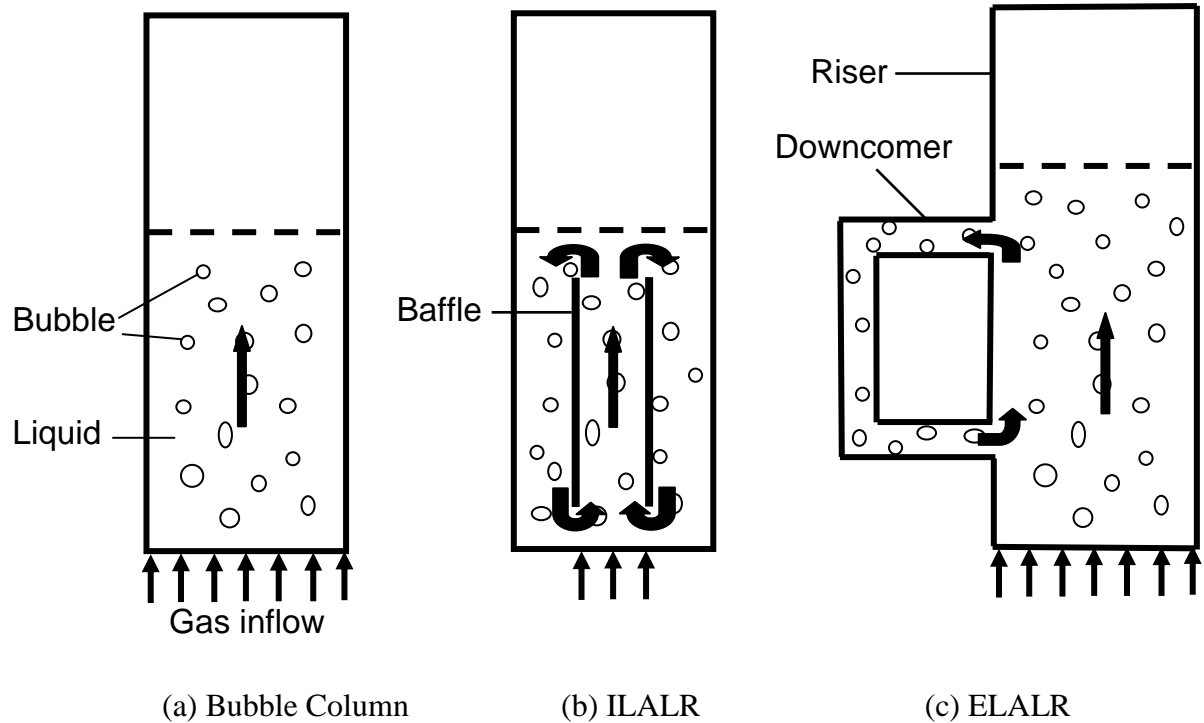
Figure 1.1. Schematic representations of different kinds of reactors, where the arrow indicates primary fluid flow direction.

In spite of numerous advantages offered by the ELALR over bubble column reactors, the hydrodynamics of the reactor remains poorly understood.   For example, the closure models for interfacial momentum transfer and eddy viscosity rely heavily upon experimental data such as bubble size, shape, and flow regime.   Agreement of computational fluid dynamics (CFD) simulations with experimental data is not possible unless appropriate closure models are employed.   Other unresolved issues of hydrodynamics in ELALRs include comparisons between two- and three-dimensional simulations, prediction of regime transition from homogeneous to heterogeneous flow, mixing phenomena, and effects of

reactor geometry on the hydrodynamic behavior. A reliable reactor design can be realized only if detailed knowledge of the complex fluid dynamics such as time-dependant information for pressure, holdup (volumetric fraction), and velocity distributions of each phase in the reactor is acquired.

Both experiments and CFD have been used to gain a better understanding about the underlying physics of gas-liquid ELALR flows. Experiments are conventionally used in the design of gas-liquid ELALR. However, it is often expensive to build pilot-scale facilities in order to study the flow behavior of an ELALR because a laboratory-scale reactor does not exactly exhibit the flow behavior of a real reactor. To resolve this shortcoming, CFD provides an alternate way to understand the gas-liquid behavior by providing the transient flow information that most experiments are unable to offer. As a result, it motivates the current research to utilize novel CFD techniques such as the ensemble-averaged Eulerian-Eulerian method with empirical closure models to predict two-phase flow dynamics accurately for design and scale-up of the ELALR.

1.2. Problem Statement and Approaches

This research investigates the hydrodynamic behavior of an air-water ELALR by employing CFD as a tool for providing two-phase flow information and validates the simulations with available experimental data from the literature. An ensemble-averaged Eulerian-Eulerian model is used to simulate the air-water ELALR hydrodynamics. The numerical code, CFDLib, will be used as the computational tool. Prior to successful CFD predictions of air-water ELALR hydrodynamics, a grid resolution study with an effective bubble diameter will be performed for a two-dimensional air-water bubble column reactor. The closure models such as drag force between gas and liquid phases and eddy viscosity for

5

different flow regimes will also be tested. The next task is to analyze and simulate hydrodynamics of an ELALR in two- and three-dimensional systems with appropriate closure models obtained from the first task. Temporal and spatial average gas holdup will be simulated over a range of superficial gas velocities and different operating modes. Comparison of simulations with experiments will also be performed. Superficial gas velocity is defined as the total volume gas flow rate at the inlet divided by the cross-sectional area of the distributor plate. The second task is followed by the study of whether two-dimensional (2D) modeling is valid by comparing it with three-dimensional (3D) simulations of gas-liquid flows. This task plausibly alleviates the time-intensive 3D computations by executing 2D simulations for gas-liquid reactor flows. Flow behavior over a range of inlet superficial gas velocities that encompasses from homogeneous to heterogeneous flow regimes will also be investigated. The last task is to implement bubble break-up and coalescence closure models into the CFDLib code, validate the implemented code, and investigate the effects of models on the simulations of external loop airlift reactor flows at the high superficial gas velocities.

1.3. Outline of the Dissertation

A survey of literature on the experimental, computational modeling, and simulation methods of hydrodynamics of airlift reactors is presented in Chapter 2. The governing equations and numerical methods are described in detail in Chapter 3. The closure models for the equations such as interfacial momentum transfer and eddy viscosity are presented. The detailed discretization methods of governing equations for spatial and temporal coordinates are also demonstrated. Chapter 4 presents the hydrodynamic simulations of a bubble column reactor in a two-dimensional system and they are validated with experimental data. Grid resolution and closure models are investigated extensively in this chapter.

Chapter 5 presents simulations of the ELALR in two- and three-dimensional systems and compares CFD predictions with experiments over a range of superficial gas velocities and different operating modes. Chapter 6 validates the implemented code of bubble break-up and coalescence closure models with simulations and experiments as well as discusses effects of the models on the simulations of the ELALR. Chapter 7 concludes the dissertation work and discusses the future work.

References

[1]   Kashiwa, B.A., 1987, "Statistical Theory of Turbulent Incompressible Multimaterial Flow", University of Washington. Ph.D. Dissertation.

[2]   Sanyal, J., Vasquez, S., Roy, S., Duduković, M.P., 1999., "Numerical Simulation of Gas-Liquid Dynamics in Cylindrical Bubble Column Reactors", Chemical Engineering Science, 54, 5071-5083.

[3]   Joshi, J.B., 2001, "Computational Flow Modeling and Design of Bubble Column Reactors", Chemical Engineering Science, 56 (21-22), pp. 5893-5933.

CHAPTER 2. LITERATURE REVIEW

The hydrodynamics of airlift reactors are characterized by the buoyancy driven flow due to the rising bubbles in the riser section of the reactor. Gas-liquid flow dynamics in airlift reactors were studied extensively in the past three decades using experimental, modeling, and simulation techniques. This chapter presents the previous contributions made by researchers to further understand fundamentals of the reactor hydrodynamics.

2.1. Experimental Techniques

2.1.1. Internal Loop Airlift Reactor

Hydrodynamic parameters such as gas holdup, liquid velocity, and mass transfer rate were measured locally and globally in airlift reactors by a variety of experimental techniques. Bello et al. [1] are considered the earliest researchers who investigated the hydrodynamics of internal loop airlift reactors (ILALRs) experimentally. Bello et al. [1] studied the effects of geometry such as downcomer to riser cross-sectional area ratio. Gas holdup at the riser and downcomer sections and overall mass transfer characteristics were investigated with manometric method, which the differences of hydrostatic pressures were measured by electronic pressure sensors, and liquid solution tracer technique, respectively. They observed that the overall mass transfer increases as the downcomer to riser cross-sectional area ratio decreases and approached bubble column mode eventually. Both the riser gas holdup and overall volumetric mass transfer coefficient were found to increase with increasing superficial gas velocity and the corresponding specific gasing power input. They were

followed by Chisti et al. [2] who measured liquid circulation velocity in an ILALR using liquid solution tracer techniques.

Lu et al. [3] investigated the liquid mixing and velocity in the riser and downcomer, and the overall liquid mixing characteristics of ILALRs using a liquid solution tracer method. Overall axial dispersion coefficient was used to quantify the degree of mixing. They found that the overall axial dispersion coefficient in the riser was higher than that in the downcomer. The two-phase system exhibited a higher degree of mixing than that of a three-phase system. In addition, the liquid mixing was found to increase as the aeration rate and draft tube length increased, respectively. Lu et al. [4] also investigated liquid velocity and gas holdup in three-phase ILALRs with liquid solution tracer and manometric techniques, respectively. They found that the liquid velocity increased with an increase in aeration rate or draft tube length, whereas it decreased as the diameter of the particles increased. Moreover, they observed that both of the liquid velocity and gas holdup decreased as the solids loading increased. Lo and Hwang [5] studied the local hydrodynamics of the gas phase in an ILALR. They measured the hydrodynamic properties including gas holdup, bubble velocity, and bubble chord length with dual electrical resistivity probes. Most bubbles were found to rise along the riser central axis and resulted in higher gas holdup in the axis. They also concluded that the bubble rise velocity and bubble size for the three-phase system are lower than that of the two-phase system.

The effects of geometry on the hydrodynamics of an internal loop airlift reactor were researched by several investigators experimentally [6, 7, 8, 9]. Wei et al. [6] concluded that the gas holdup and liquid velocities in convergence-divergence draft tubes are greater and less than that in a conventional draft tube, respectively. Klein et al. [7] investigated the effect

of a gas-liquid separator on the hydrodynamics and flow regimes in an ILALR. They measured the liquid velocity and gas holdup in all sections of the internal loop airlift reactor using magnetic tracer and manometric methods, respectively. At low superficial gas velocity, the separator had no influence on gas holdup, liquid circulation velocity, and turbulence intensity in the downcomer and separator; however, higher and lower downcomer gas holdup and liquid velocity, respectively, were observed at the airlift reactor with the separator than that of without the separator for the high superficial gas velocity. On the other hand, the separator had some influence on the gas holdup in the riser. Blazej et al. [8] showed that industrial size reactor can significantly increase the riser gas holdup and overall liquid circulation velocity of the two-phase gas-liquid flow in an internal loop airlift reactor, especially in the heterogeneous regime. They further mentioned that it is advisable to use larger reactor volumes to avoid unfavorable influences due to wall effects so as to increase the gas holdup and reduce the mixing time. Kilonzo et al. [9] studied the effects of baffle clearances, which the clearance is between the liquid free surface and top of the baffle, and between the distributor plate and bottom of the baffle, on the hydrodynamics of an internal loop airlift reactor. They found that the liquid circulation velocity increased and remained unchanged as the clearances increased to some degree.

Wu and Merchuk [10] and Lin et al. [11] are considered the most recent researchers who utilized cutting-edge non-invasive experimental techniques. Wu and Merchuk [10] used an optical trajectory-tracking system and Lin et al. [11] used a particle image analyzer to probe the hydrodynamics of an internal loop airlift reactor. For both works, neutrally buoyant particles were used to follow the flow and a high speed, high resolution camera to

record the images of the flow field. Instantaneous and time-averaged flow behaviors in a gas entrainment regime for an internal loop airlift reactor were provided by both investigators.

2.1.2. External Loop Airlift Reactor

Merchuk and Stein [12] and Weiland and Onken [13] pioneered experimental investigations into the hydrodynamics of external loop airlift reactors (ELALRs) in 1981. Merchuk and Stein [12] measured liquid circulation velocity and local gas holdup of an ELALR using a magnetic flow meter and a differential pressure, respectively. They correlated liquid velocity to gas flow rate with a simple exponential function and local gas velocity with total flow rate of the mixture using a simple linear relationship. They also observed that local gas holdup varied appreciably along the column and showed a maximum close to the center of the riser in most of the cases. Similarly, Weiland and Onken [13] measured the liquid circulation velocity and gas holdup in an ELALR with the same techniques as Merchuk and Stein [12], and mixing time and dispersion coefficient using conductivity and pulse tracer methods, respectively. They were followed by Bello et al. [1] who investigated the effects of geometry on the hydrodynamics of both ILALRs and ELALRs.

Young et al. [14] are the first investigators to study the local two-phase hydrodynamics in an external loop airlift reactor. They measured the local liquid velocity by hot-film technique, the local gas velocity by the resistivity probe method, and the global and radial gas holdups by the gamma densitometry technique. As a result, they calculated the liquid turbulence intensity and the slip velocity between gas and liquid phases. They observed distinct changes in the radial profiles of fluid flow properties with axial position.

The airlift riser was also observed to create significantly higher frictional effects at the wall than is routinely observed for fully-developed flow.

Snape et al. [15] investigated the effects of liquid properties and sparger design on the hydrodynamics of gas-liquid ELALRs. Gas holdup was measured with a manometric technique that is based on a pressure difference method. Both gas holdup and liquid velocity were strongly influenced by the sparger design whereas the gas holdup was higher in an electrolyte solution as compared to an air-water system.

Gavrilescu and Tudose [16] investigated the mixing behavior of the liquid phase in two external loop airlift reactors of laboratory and pilot scales. The mixing parameters, mixing time and axial dispersion coefficient, were determined using a liquid solution tracer response technique and were analyzed in relation to operating and geometrical parameters. They correlated mixing with the liquid circulation velocity and found that mixing decreases as the liquid circulation velocity increases or downcomer to riser cross-sectional area ratio increases.

Benyahia and Jones [17] tested large and small scale effects on hydrodynamic and mass transfer characteristics of external loop airlift reactors. The gas holdup and oxygen uptake experiments were carried out using manometric and oxygen probe techniques, respectively. Large-scale reactor exhibits higher gas holdup than that of small scale reactor due to greater liquid volume. Both gas holdup and mass transfer coefficient increased as the superficial gas velocity increased.

Al-Masry and Abasaeed [18] carried out experiments to study hydrodynamic and mass transfer characteristics in ELALRs with varying downcomer to riser cross-sectional area ratio. The gas holdup was measured with a manometer whereas the liquid velocity in

the downcomer was measured with electromagnetic flow meters. The liquid velocity in the riser was calculated with the continuity equation. At constant superficial gas velocity, they also found that an increase in the area ratio results in an increase in liquid circulation velocity and reduction in both gas holdup and mass transfer coefficient.

Bentifraounine et al. [19] evaluated the local gas characteristics in an external loop airlift reactor in Newtonian and non-Newtonian fluids with the use of a double-optical fiber probe. They presented the three radial and axial coordinates of the gas holdup, bubbling frequency, and bubble diameter size at three superficial gas velocities of 0.8, 2.3, and 4.6 cm/s for each fluid. In both of the fluids, the gas holdup, bubbling frequency, bubble size, and bubble velocity increased as the superficial gas velocity increased.

Bendjaballah et al. [20] studied the flow regimes in an external loop airlift reactor. The gas holdup and liquid velocity were measured by pressure difference and conductivity pulse methods, respectively. They represented the slip velocity of the gas as a function of the overall fluid velocity in the riser to distinguish between homogeneous and heterogeneous flow regimes. The transition between the flow regimes depended on the resistance to liquid circulation, namely, the change of downcomer diameter by inserting a valve on the downcomer. The flow regime depended on the initial gas distribution and on the size of the reactor. For instance, improvement from single-orifice to multiple-orifice sparger and the increase of column height lead to a more homogeneous flow.

Vial et al. [21] identified regime transition in a bubble column and an ELALR for several spargers based on a pressure fluctuation analysis. They proposed a new method based on an auto-correlation function and it provided quantitative information about the

characteristic time and axial dimension of the flow structure in the prevailing regime. It also allowed regime identification without the need for varying the superficial gas velocity.

Choi K.H. [22] studied flow in an ELALR to determine the effects of the static liquid height, the superficial gas velocity, and the downcomer to riser cross-sectional area ratio on the hydrodynamic characteristics, such as the gas holdup, liquid circulation velocity, and mixing time. The gas holdup in the riser and downcomer, and the mixing time were found to decrease with increasing static liquid height because the liquid circulation velocity increases. Choi K.H. [22] also observed that the riser gas holdup increases as the superficial gas velocity increases, whereas the downcomer gas holdup and mixing time decrease owing to increasing liquid circulation velocity. Lastly, Choi K.H. [22] found that an increasing downcomer to riser cross-sectional area ratio increases the liquid circulation velocity and downcomer gas holdup, and decreases riser gas holdup and mixing time.

Lin et al. [23] obtained detailed local gas-liquid-solid three-phase hydrodynamic parameters for an external loop airlift reactor using a fiber-optic probe and laser Doppler anemometry techniques to measure local gas holdup and liquid circulation velocity, respectively. The provision of detailed local hydrodynamic information was an important contribution to gain a better understanding of the flow in the reactor. The hydrodynamic information can be used for CFD simulations and validation of models. Their experimental results showed that large bubbles tend to gather near the reactor centerline, which led to stronger interactions between the bubbles and results in higher bubble velocities in the central region. Bubble coalescence prevailed near the distributor, while bubble breakup was an important phenomenon in the fully developed reactor part. Along the axial direction, the bubble rise velocity first increased because of the formation of large bubbles and then

decreased because of bubble breakup under the agitation of turbulence kinetic energy from the liquid. They also found that both the gas holdup and liquid circulation velocity decreased with increasing solid volume fraction due to the increase in the viscosity of solid-liquid suspension. The increase in the solid volume fraction also results in an increase of the bubble size and bubble rise velocity in the homogeneous flow regime. Lin et al. [24] also performed another experimental study on the influence of the gas distributor on the local hydrodynamic behavior of an external loop airlift reactor. They found that the porous plate could distribute the gas phase much better than that of perforated plate.

Mohanty et al. [25] studied the hydrodynamics of a multi-stage external loop airlift reactor. They found that the gas holdup in the multi-stage system was 45% higher than the single stage system for the same superficial gas and liquid velocities. A higher gas holdup also results in better mass transfer between the gas and liquid phases.

Liu et al. [26] quantified the mixing between phases by investigating liquid dispersion in an external loop airlift slurry reactor. The gas holdup in the riser was measured with manometric techniques whereas a tracer input-response technique was used to measure the liquid circulation velocity and liquid axial dispersion coefficient. They proposed a liquid dispersion coefficient model based on the Taylor dispersion equation and good agreement was obtained with experiments. The liquid dispersion coefficient was found to increase with an increase in the superficial gas velocity, liquid velocity, or liquid level in the gas-liquid separator, and decrease with increasing concentrations of fine particles or flowing resistance.

2.2. Modeling and Simulations of Airlift Reactors

Several modeling studies have been done in the past on airlift reactors. For example, modeling work was performed to calculate the liquid circulation velocity in two-phase airlift reactors by a combination of macroscopic momentum balance and empirical gas holdup and pressure drop correlations ([27], [28]). Other modeling efforts include using energy balance ([29], [30], [31], [32]), a drift flux model, in combination with a steady-state mechanical energy balance ([12], [4], [33]). Bello et al. [29] used an energy balance on the ELALR to correlate the riser liquid velocity to the riser superficial gas velocity as a function of the reactor geometry, liquid properties, and the flow regime. However, the majority of the modeling studies was based on one-dimensional equations and does not give detailed flow information. Furthermore, the developed correlations and one-dimensional models are restricted to certain flow regimes, reactor geometry, operating conditions, and depend on experimentally determined values such as drag and axial dispersion coefficients. For instance, the liquid circulation velocity predictions of Bello et al. [29] did not compare satisfactorily with the liquid circulation experiments of Herskowitz and Merchuk (1986). Therefore, the CFD simulations are relied upon to predict the hydrodynamics of airlift reactors to compensate for the deficiencies encountered in the aforementioned modeling studies.

Numerical simulations of airlift reactors employing an Eulerian-Eulerian ([34], [35]) model were surveyed and literature on Eulerian-Lagrangian simulations of airlift reactor hydrodynamics were not found. The Eulerian-Eulerian model treats dispersed (gas bubbles) and continuous (liquid) phases as interpenetrating continua, and describes the motion for gas and liquid phases in an Eulerian frame of reference. Although there are a number of airlift

reactor experiments and modeling, the CFD simulations of airlift reactors are still lacking. Several investigators studied the hydrodynamics of internal and external loop airlift reactors with the Eulerian-Eulerian CFD approach in the past. Oey et al. [36] presented 3D CFD simulations in a rectangular internal loop airlift reactor with an Eulerian-Eulerian two-fluid approach. A k-ε turbulence model with extra source terms and a drag force were used to model the effective stress and interfacial momentum transfer of the two-phase flow. They conducted simulations at different superficial gas velocities and observed that the oscillation period of the liquid velocity in the downcomers decreased with increasing superficial gas velocity. The oscillation frequencies also showed minor changes when increasing the static liquid height. The simulations presented upward and downward liquid flows inside and outside the baffles, respectively.

Mudde and Van den Akker [37] performed 2D and 3D CFD simulations of the gas-liquid flow in a rectangular internal loop airlift reactor at low superficial gas velocities using an Eulerian-Eulerian two-fluid model. The effects of the so-called drifting velocity, drag force, virtual mass force as well as bubble induced modifications of the turbulence were accounted in their simulations. They compared the 2D with 3D simulations as well as with the one-dimensional mechanical energy balance and their experiments. The overall liquid velocity and gas holdup were presented for various superficial gas velocities. The 3D simulations showed better agreement with experiments than that of the 2D simulations for both hydrodynamic parameters. The predictions between the 2D and 3D simulations did not present much discrepancy except for the overall gas holdup parameter.

Van Baten et al. [38] studied the hydrodynamics of internal loop airlift reactors for various superficial gas velocities using the Eulerian-Eulerian model and compared the

simulations with experiments. Closure terms for the drag force and the standard k-ε turbulence model were used. The CFD model showed good agreement with the measured data for gas holdup and liquid velocity in the downcomer and riser. The predictions between the 2D and 3D simulations did not exhibit much discrepancy for both of the local gas holdup and liquid velocity parameters at 10 cm/s superficial gas velocity.

As for the external loop airlift reactor simulations, Wang et al. [39] conducted two-dimensional steady-state simulations of a cylindrical external loop airlift reactor using an Eulerian-Eulerian method and showed that the interfacial forces and turbulence have noticeable influence on predicting the hydrodynamic behavior. In addition, Cao et al. [40] performed three-dimensional transient simulations of a rectangular external loop airlift reactor and obtained good agreement between the predicted hydrodynamic parameters and experiments, except in a high gas flow rate regime. The inaccuracy of simulations at high superficial gas velocity was shown to be due to the poor estimation of the turbulence parameters. Roy et al. [41] conducted three-dimensional steady-state simulations of a cylindrical ELALR and found agreement between the CFD Eulerian-Eulerian predictions for gas holdup, axial liquid velocity, and mixing time with experiments. Interfacial forces such as drag, lift, and turbulent dispersion forces and bubble-induced turbulence were used in their simulations. A comparison of predicted and the experimental liquid circulation velocity was presented over a wide range of superficial gas velocity, downcomer to riser cross-sectional area ratio, and riser cross-sectional area. It should be noted that Wang et al. [39] and Cao et al. [40] conducted experiments in addition to numerical simulations.

2.3. Summary

The literature of experimental, modeling, and simulation techniques of airlift reactors were surveyed. It is clear that more CFD studies are needed to validate the large amount of experimental data from the literature in order to gain in-depth understandings of fundamentals of airlift reactor hydrodynamics. In addition, the CFD simulations can provide detailed transient and time-averaged flow information inside of the reactors that are pertinent to the reaction studies. For example, determining local gas holdup and liquid velocities are a challenge to measure experimentally. Furthermore, the extensive grid resolution studies, which are hardly found in the literature, and closure terms such as drag force and turbulence models need to be further tested for an accurate Eulerian-Eulerian gas-liquid airlift reactor simulation. Therefore, future computational modeling and simulations for air-water external loop airlift reactor will advance the knowledge of fundamentals of reactor hydrodynamics. The following section will present the theoretical formulation of gas-liquid airlift reactor before the result findings are discussed in chapters 4 and 5.

References

[1]   Bello, R.A., Robinson, C.W., Moo-Young, M., 1985a, "Gas Holdup and Overall Volumetric Oxygen Transfer Coefficient in Airlift Contactors", Biotechnology and Bioengineering, 27, pp. 369-381.

[2]   Chisti, Y., Moo-Young, M., 1988, "Liquid Circulation in ALR", Chemical Engineering Science, 43, pp. 451-457.

[3]   Lu, W.J., Hwang, S.J., Chang, C.M., 1994, "Liquid Mixing in Internal Loop Airlift Reactors", Industrial & Engineering Chemistry Research, 33(9), pp. 2180-2186.

[4]   Lu, W.J., Hwang, S.J., 1995, "Liquid Velocity and Gas Holdup in Three-Phase Internal Loop Airlift Reactors with Low-Density Particles", Chemical Engineering Science, 50 (8), pp. 1301-1310.

[5] Lo, C.S., Hwang, S.J., 2003, "Local Hydrodynamic Properties of Gas Phase in an Internal Loop Airlift Reactor", Chemical Engineering Journal, 91, pp. 3-22.

[6] Wei, C.H., Xie, B., Xiao, H.L., 2000, "Hydrodynamics in an Internal Loop Airlift Reactor with a Convergence-Divergence Draft Tube", Chemical Engineering Technology, pp. 38-45.

[7] Klein, J., Godo, S., Dolgos, O., Markos, J., 2001, "Effect of a Gas-Liquid Separator on the Hydrodynamics and circulation flow regimes in internal-loop airlift reactors", Journal of Chemical Technology and Biotechnology, 76, pp. 516-524.

[8] Blazej, M., Kisa, M., Markos, J., 2004, "Scale Influence on the Hydrodynamics of an Internal Loop Airlift Reactor", Chemical Engineering and Processing, 43, pp. 1519-1527.

[9] Kilonzo, P.M., Margaritis, A., Bergougnou, M.A., Yu, J.T., Qin, Y., 2006, "Influence of the Baffle Clearance Design on Hydrodynamics of a Two Riser Rectangular Airlift Reactor with Inverse Internal Loop and Expanded Gas-Liquid Separator", Chemical Engineering Journal, 121, pp. 17-26.

[10] Wu, X., Merchuk, J.C., 2003, "Measurement of Fluid Flow in the Downcomer of an Internal Loop Airlift Reactor using an Optical Trajectory-Tracking System", Chemical Engineering Science, 58, pp. 1599-1614.

[11] Lin, T.J., Chen, P.C., 2005, "Studies on Hydrodynamics of an Internal Loop Airlift Reactor in Gas Entrainment Regime by Particle Image Analyzer", Chemical Engineering Journal, 108, pp. 69-79.

[12] Merchuk, J.C., Stein, Y., 1981, "Local Hold-up and Liquid Velocity in Air-lift Reactors", American Institute of Chemical Engineers Journal, 27, pp. 377-388.

[13] Weiland, P., and Onken, U., 1981, "Differences in the Behaviour of Bubble Columns and Airlift Loop Reactors", German Chemical Engineering, 4, pp. 174-181.

[14] Young, M.A., Carbonell, R.G., Ollis, D.F., 1991, "Airlift Bioreactors: Analysis of Two-Phase Hydrodynamics", American Institute of Chemical Engineers, 37 (3), pp. 403-428.

[15] Snape, J.B., Zahradnik, J., Fialova, M., Thomas, N.H., 1995, "Liquid-Phase Properties and Sparger Design Effects in an External Loop Airlift Reactor", Chemical Engineering Science, 50(20), pp. 3175-3186.

[16] Gavrilescu, M., Tudose, R.Z., 1997, "Mixing Studies in External Loop Airlift Reactor", Chemical Engineering Journal, 66, pp. 97-104.

[17] Benyahia, F., Jones, L., 1997, "Scale Effects on Hydrodynamic and Mass Transfer Characteristics of External Loop Airlift Reactors", 69, pp. 301-308.

[18] Al-Masry, W.A., Abasaeed, A.E., 1998, "On the Scale-Up of External Loop Airlift Reactors: Newtonian Systems", Chemical Engineering Science, 53(24), pp. 4085-4094.

[19] Bentifraouine, C., Xuereb, C., Riba, J.P., 1999, "Local Gas Hydrodynamics in an External Loop Airlift Reactor: Newtonian and Non-Newtonian Fluids", Bioprocess Engineering, 20, pp. 303-307.

[20] Bendjaballah, N., Dhaouadi, H., Poncin, S., Midoux, N., Hornut, J.M., Wild, G., 1999, "Hydrodynamics and Flow Regimes in External Loop Airlift Reactors", Chemical Engineering Science, 54, pp. 5211-5221.

[21] Vial, C., Camarasa, E., Poncin, S., Wild, G., Midoux, N., Bouillard, J., 2000, "Study of Hydrodynamic Behaviour in Bubble Columns and External Loop Airlift Reactors through Analysis of Pressure Fluctuations", Chemical Engineering Science, 55, pp. 2957-2973.

[22] Choi, K.H., 2002, "Effect of Unaerated Liquid Height on Hydrodynamic Characteristics of an External Loop Airlift Reactor", Chemical Engineering Communications, 189(1), pp.23-39.

[23] Lin, J., Han, M., Wang, T., Zhang, T., Wang, J., Jin, Y., 2004, "Experimental Study on the Local Hydrodynamic Behavior of a Three-Phase External Loop Airlift Reactor", Industrial and Engineering Chemistry Research, 43(18), pp. 5432-5437.

[24] Lin, J., Han, M., Wang, T., Zhang, T., Wang, J., Jin, Y., 2004, "Influence of the Gas Distributor on the Local Hydrodynamic Behavior of an External Loop Airlift Reactor", Chemical Engineering Journal, 102, pp. 51-59.

[25] Mohanty, K., Das, D., Biswas, M.N., 2006, "Hydrodynamics of a Novel Multi-Stage External Loop Airlift Reactor", Chemical Engineering Science, 61, pp. 4617-4624.

[26] Liu, M., Zhang, T., Wang, T., Yu, W., Wang, J., 2008, "Experimental Study and Modeling on Liquid Dispersion in External Loop Airlift Slurry Reactors", Chemical Engineering Journal, 139, pp. 523-531.

[27] Hsu, T.C., Dudukovic, M.P., 1980, "Gas Holdup and Liquid Recirculation in Gas-Lift Reactors", Chemical Engineering Science, 35, pp. 135-141.

[28] Koide, K., Iwamoto, S., Takasaka, Y., Matsuura, S., Takahashi, E., Kimura, M., Kubota, H., 1984, "Liquid Circulation, Gas Holdup and Pressure Drop in Bubble Column with Draught Tube", Journal of Chemical Engineering Japan, 17, pp. 611-618.

[29] Bello, R.A., Robinson, C.W., Moo-Young, M., 1984, "Liquid Circulation and Mixing Characteristics of Airlift Contactors", The Canadian Journal of Chemical Engineering, 62, pp. 573-579.

[30] Jones, A.G., 1985, "Liquid Circulation in a Draft-Tube Bubble Column", Chemical Engineering Science, 40, pp. 449-462.

[31] Chisti, M.Y., Halard, B., Moo-Young, M., 1988, "Liquid Circulation in Airlift Reactors", Chemical Engineering Science, 43, pp. 451-457.

[32] Garcia Calvo, E., 1989, "A Fluid Dynamic Model for Airlift Reactors", Chemical Engineering Science, 44, pp. 321-323.

[33] Verlaan, P., Tramper, J., van't Riet, K., Luyben, K. Ch. A. M., 1986, "A Hydrodynamic Model for an Airlift Loop Bioreactor with External Loop", Chemical Engineering Journal, 33, pp. B43-B53.

[34] Delhaye, J., 1974, "Jump Conditions and Entropy Sources in Two-Phase Systems", International Journal of Multiphase Flow, 1, pp. 395-409.

[35] Drew, D.A., 1983, "Mathematical Modeling of Two-Phase Flow", Annual Review of Fluid Mechanics, 15, pp. 261-291.

[36] Oey, R.S., Mudde, R.F., van den Akker, H.E.A., 2003, "Numerical Simulations of an Oscillating Internal Loop Airlift Reactor", The Canadian Journal of Chemical Engineering, 81, pp.684-691.

[37] Mudde, R.F., van den Akker, H.E.A., 2001, "2D and 3D Simulations of an Internal Airlift Loop Reactor on the Basis of a Two-Fluid Model", Chemical Engineering Science, 56, pp. 6351-6358.

[38] van Baten, J.M., Ellenberger, J., Krishna, R., 2003, "Hydrodynamics of Internal Loop Airlift Reactors: Experiments versus CFD Simulations", Chemical Engineering and Processing, 42, pp. 733-742.

[39] Wang, T., Wang, J., and Jin, Y., 2004, "Experimental Study and CFD Simulation of Hydrodynamic Behaviours in an External Loop Airlift Slurry Reactor", The Canadian Journal of Chemical Engineering, 82(6), pp. 1183-1190.

[40] Cao, C., Dong, S., and Guo, Q., 2007, "Experimental and Numerical Simulation for Gas-Liquid Phases Flow Structure in an External-Loop Airlift Reactor", Industrial and Engineering Chemical Research, 46, pp. 7317-7327.

[41] Roy, S., Dhotre, M.T., and Joshi, J.B., 2006, "CFD Simulation of Flow and Axial Dispersion in External Loop Airlift Reactor", Chemical Engineering Research and Design, 84(A8), pp. 677-690.

CHAPTER 3. THEORETICAL FORMULATION

In this chapter, the governing equations of the Eulerian-Eulerian formulation and closure models are presented for a two-phase flow. The code CFDLib, a multiphase simulation library developed at Los Alamos National Laboratory [1,2], is used to solve the governing equations for the gas-liquid flow in this study. The numerical formulations of the governing equations will also be discussed.

3.1. Governing Equations

The two-fluid Eulerian-Eulerian model is employed to represent each phase as interpenetrating continua and the conservation equations for mass and momentum for each phase are ensemble-averaged. The variable ϕ represents either the continuous (liquid water) phase c or the dispersed (air bubble) phase d. The continuity equation for phase ϕ, neglecting mass transfer, is:

$$\frac{\partial}{\partial t}\left(\alpha_\phi \rho_\phi\right) + \nabla \cdot \left(\alpha_\phi \rho_\phi \vec{u}_\phi\right) = 0 \tag{1}$$

The momentum equation for phase ϕ is:

$$\frac{\partial}{\partial t}\left(\alpha_\phi \rho_\phi \vec{u}_\phi\right) + \nabla \cdot \left(\alpha_\phi \rho_\phi \vec{u}_\phi \vec{u}_\phi\right) = -\alpha_\phi \nabla P + \nabla \cdot \bar{\bar{\tau}}_\phi + \vec{K}_{\theta\phi}\left(\vec{u}_\theta - \vec{u}_\phi\right) + \vec{F}_{vm} + \rho_\phi \alpha_\phi \vec{g} \tag{2}$$

where θ identifies the opposite phase. The variable α represents volume fraction and the sum of each phasic volume fraction is equal to unity. The terms on the right hand side of Eq. (2) represent, from left to right, the pressure gradient, effective stress, interfacial momentum

exchange (drag and virtual mass forces), and the gravitational force. The closure models for interfacial momentum exchange and turbulence effects are discussed next.

3.1.1. Interfacial Momentum Exchange

The interfacial momentum exchange terms in Eq. (2) for each phase consist of drag and virtual mass force terms. The momentum exchange coefficient for the gas (d) and liquid (c) phases are modeled as:

$$\vec{K}_{\phi\theta} = \frac{3}{4}\rho_c\alpha_c\alpha_d\frac{C_D}{d_b}\left|\vec{u}_\phi - \vec{u}_\theta\right| \tag{3}$$

where C_D is the drag coefficient. The virtual mass force $\vec{F}_{vm}$ is modeled as:

$$\vec{F}_{vm} = 0.5\alpha_d\rho_c\left(\frac{d\vec{u}_\phi}{dt} - \frac{d\vec{u}_\theta}{dt}\right) \tag{4}$$

and the coefficient of 0.5 is used for a spherical bubble [3]. The virtual mass force models the mass inertia added to the liquid phase as the bubble moves through the liquid continuum.

The drag coefficient model proposed by White [4] that is included in CFDLib, is of the expression:

$$C_D = C_\infty + \frac{24}{\text{Re}} + \frac{6}{1+\sqrt{\text{Re}}} \qquad 0 \le \text{Re} \le 2\times10^5 \tag{5}$$

where C_∞ is the drag coefficient when the bubble Reynolds number goes to 2×10^5. In our calculation C_∞, which is the drag coefficient at the particular bubble Reynolds number, is set to 0.5. An alternative drag coefficient model was proposed by Schiller and Naumann [5]. As part of the research herein, the Schiller and Naumann model was implemented into CFDLib, where the drag coefficient is:

$$C_D = \begin{cases} 24(1+0.15\,\text{Re}^{0.687})/\text{Re} & \text{Re} \le 1000 \\ 0.44 & \text{Re} > 1000 \end{cases} \tag{6}$$

The bubble Reynolds number $\mathrm{Re} = \rho_c |\vec{u}_d - \vec{u}_c| d_b / \mu_c$ is based on a characteristic (effective) bubble diameter, the slip velocity between the two phases, and the liquid density and dynamic viscosity. The validity of using these drag coefficient models will be discussed in Chapter 4.

3.1.2. Turbulence Modeling

Turbulence contributions for the continuous and dispersed phases are based on a modified form of the standard multiphase k-ε equations, first presented by Kashiwa [6] and described in detail by Padial et al. [7], to calculate turbulence at the gas-liquid interface in the form of a slip-production energy term. The modified k-ε equations are used here only for high superficial gas velocity flows. The equations for the turbulence kinetic energy and turbulence dissipation, respectively, are:

$$\frac{\partial}{\partial t}\left(\alpha_\phi \rho_\phi k_\phi\right) + \nabla \cdot \left(\alpha_\phi \rho_\phi k_\phi \vec{u}_\phi\right) =$$

$$\nabla \cdot \left(\alpha_\phi \frac{\mu_{t,\phi}}{\sigma_k}\nabla k_\phi\right) + \alpha_\phi G_\phi - \alpha_\phi \rho_\phi \varepsilon_\phi + \sum_{\theta \neq \phi}\beta_{\phi\theta}K_{\phi\theta}\left|\vec{u}_\phi - \vec{u}_\theta\right|^2 + 2\sum_{\theta \neq \phi}E_{\phi\theta}(k_\theta - k_\phi) \tag{7}$$

$$\frac{\partial}{\partial t}\left(\alpha_\phi \rho_\phi \varepsilon_\phi\right) + \nabla \cdot \left(\alpha_\phi \rho_\phi \varepsilon_\phi \vec{u}_\phi\right) =$$

$$\nabla \cdot \left(\alpha_\phi \frac{\mu_{t,\phi}}{\sigma_\varepsilon}\nabla \varepsilon_\phi\right) + \alpha_\phi \frac{\varepsilon_\phi}{k_\phi}\left(C_{1\varepsilon}G_\phi - C_{2\varepsilon}\rho_\phi \varepsilon_\phi\right) + \frac{1}{\tau_{\phi\theta}}\left\{\sum_{\theta \neq \phi}\beta_{\phi\theta}K_{\phi\theta}\left|\vec{u}_\phi - \vec{u}_\theta\right|^2\right\} \tag{8}$$

Again, the subscripts ϕ and θ represent two different phases. The first three terms on the right hand side of Eq. (7) account for diffusion of turbulent kinetic energy, mean flow shear production, and decay of turbulent kinetic energy. These terms are identical to terms that appear in single-phase turbulent flow [8]. The remaining two terms in Eq. (8) are the

production of turbulent energy from slip between phases and the exchange of turbulence energy among phases. The first three terms on the right hand side of Eq. (9) account for the turbulence diffusion, the mean flow velocity gradient production term, and the homogeneous dissipation term, respectively. The last group of terms in Eq. (9) describes the effect of interfacial momentum transfer on the production of turbulence dissipation (refer to Eq. (3)).

The coefficient $\beta_{\phi\theta}$ appearing in Eq. (7) and (8) is given by:

$$\beta_{\phi\theta} = \frac{a_\phi}{a_\phi + a_\theta} \tag{9}$$

where

$$a_\phi = \frac{\alpha_\phi^{1/3}}{\rho_\phi + \rho_c} \tag{10}$$

The turbulence energy exchange rate coefficient $E_{\phi\theta}$ appearing in Eq. (7) is given by:

$$E_{\phi\theta} = \alpha_\phi \alpha_\theta \left(\frac{\rho_\phi \rho_\theta}{\rho_\phi + \rho_\theta} \right) \frac{\sqrt{k_\phi + k_\theta}}{d_b} \left(1 + \mathrm{Re}^{0.6} \right) \tag{11}$$

The time constant $\tau_{\phi\theta}$ (Eq. (8)) is given by the following empirical correlation:

$$\tau_{\phi\theta} = \left\{ 0.01 C_{2\varepsilon} (\alpha_\phi \alpha_\theta)^{0.086} \left[\frac{\rho_\phi \left| \vec{u}_\phi - \vec{u}_\theta \right| d_b}{\mu_\phi} \right]^{0.562} \frac{\left| \vec{u}_\phi - \vec{u}_\theta \right|}{d_b} \right\}^{-1} \tag{12}$$

Padial et al. [9] developed this correlation by fitting predictions of turbulence kinetic energy to data from experiments on homogeneous sedimentation and bubbly systems.

The closure models for the remaining terms appearing in Eqs. (7) and (8) for the turbulent viscosity $\mu_{t,\phi}$ and the production of turbulent kinetic energy G_ϕ of phase ϕ are:

$$\mu_{t,\phi} = \rho_\phi C_{\mu,\phi} \frac{k_\phi^2}{\varepsilon_\phi} \tag{13}$$

$$C_{\mu,\phi} = \frac{C_{\mu}}{1 + (2\sum_{\theta \neq \phi} E_{\phi\theta}k_{\phi})/(\rho_{\phi}\varepsilon_{\phi})} \tag{14}$$

$$G_{\phi} = \left[\mu_{t,\phi}\left(\nabla\vec{u}_{\phi} + (\nabla\vec{u}_{\phi})^{T} - \tfrac{2}{3}\nabla(\vec{u}_{\phi})I\right) - \tfrac{2}{3}\rho_{\phi}k_{\phi}I\right] : \nabla\vec{u}_{\phi} \tag{15}$$

where I is the identity matrix. The form of Eq. (14) models a return-to-isotropy effect due to fluctuating interfacial momentum coupling and reduces the turbulent viscosity from that predicted by single-phase theory. These turbulence parameters are set using standard empirical values for k-ε turbulence modeling, where $C_{1\varepsilon} = 1.44$, $C_{2\varepsilon} = 1.92$, $C_{\mu} = 0.09$, $\sigma_{\phi} = 1.0$, and $\sigma_{\varepsilon} = 1.3$ [10].

3.1.3. Bubble Pressure and Bubble-Induced Turbulence Models

The gas phase pressure consists of kinetic and potential pressure contributions, where the kinetic pressure is important only at low gas volume fraction or low inlet superficial gas velocity [11]. The bubble kinetic pressure represents the transport of momentum arising from bubble-velocity fluctuations caused by the continuous liquid phase, collisions between bubbles, and hydrodynamic interactions between the gas bubble and liquid continuum. The bubble pressure (BP) model refers to the kinetic pressure of the gas phase. Batchelor [11] proposed that the particle kinetic pressure is based on the particle velocity fluctuations for the gas-solid fluidized bed. Similarly, Biesheuvel and Gorissen [12] proposed a bubble pressure model for gas-liquid flows of the form:

$$P_{d} = \rho_{c}C_{BP}\alpha_{d}(u_{d} - u_{c})(u_{d} - u_{c})\left(\frac{\alpha_{d}}{\alpha_{dcp}}\right)\left(1 - \frac{\alpha_{d}}{\alpha_{dcp}}\right) \tag{16}$$

The gradient of P_{d} is added to the right hand side of the gas momentum Eq. (2) when $\phi = d$ for the dispersed phase. The virtual mass coefficient C_{BP} for an isolated spherical bubble is

0.5 [3] and used in this analysis. The bubble pressure is proportional to the slip velocity and gas holdup. The gas holdup at close packing α_{dcp} is set equal to 1.0 in this study.

The BP model is employed with a bubble induced turbulence (BIT) model and both models are only used for low superficial gas velocity flows (typically homogeneous flow). Sato et al. [13] proposed a BIT model proportional to the bubble diameter and slip velocity of the rising bubbles:

$$\mu_{t,c} = \rho_c C_{BT} \alpha_d d_b \left| \vec{u}_d - \vec{u}_c \right| \tag{17}$$

where the value of the proportionality constant C_{BT} is 0.6. Equation (17) replaces Eq. (13) when the BIT model is applied. The BIT model yields an effective viscosity in the liquid (continuous) phase that is the sum of the molecular viscosity of the continuous phase and the turbulent viscosity calculated from the BIT model, whereas the effective viscosity for the dispersed phase is assumed to equal the molecular viscosity of the dispersed phase.

3.2. Numerical Formulations

3.2.1. Basic Marker and Cell Method

CFDLib uses the Marker and Cell (MAC) [14] numerical method to solve the governing equations described in section 3.1. An adaptive time step method which the time step size varies at each time integration step is also used. All simulations use a time step according to the Courant-Friedrich-Lewy (CFL) stability criterion. The formulation of the MAC method is demonstrated next using one-dimensional conservation laws for a single-phase, inviscid, and incompressible flow without gravity. The differential forms of these equations, conservation of mass and momentum, respectively, are:

$$\frac{\partial u}{\partial x} = 0 \tag{18}$$

$$\frac{\partial u}{\partial t} + \frac{\partial u^2}{\partial x} = -\frac{1}{\rho}\frac{\partial p}{\partial x} \tag{19}$$

Here u and p are the velocity and pressure, respectively, which are functions of position x, time t, and ρ is the constant fluid density. m and V are the fluid mass and volume, respectively. The physical position is discretized at cell center as $x_i = (i - 0.5)\Delta x$, for $i = 1, 2, ..., N$, where N is the maximum number of cells. The numerical procedure for finding u^{n+1} and p^{n+1}, the new time-levels, given knowledge of u^n and p^n at time $n\Delta t$ is presented in this section. The fluxing velocity $u_{i+1/2}^{n+1}$, which is at the cell-face, at time t^{n+1} is solved through the time integration of Eq. (18) that involves the i and $i+1$ cell-centered data. The discretized finite-difference form of Eq. (19) is:

$$\frac{u_{i+1/2}^{n+1} - u_{i+1/2}^{n}}{\Delta t} = \frac{\left(u_i^n\right)^2 - \left(u_{i+1}^n\right)^2}{\Delta x} + \frac{1}{\rho}\frac{p_i^n - p_{i+1}^n}{\Delta x} \tag{20}$$

According to Eq. (18), it may be noted that the cell-centered velocity is expressed as:

$$u_i^n = \frac{1}{2}\left(u_{i-1/2}^n + u_{i+1/2}^n\right) \tag{21}$$

By applying a partial derivative with respect to x to Eq. (19), the following conservation equation is obtained based upon the conservation of mass from Eq. (18) and the divergence of the momentum equation (Eq. (20)) produces a potential equation for the pressure:

$$\left[\frac{p_{i+1}^n - 2p_i^n + p_{i-1}^n}{\rho(\Delta x)^2} + \frac{A\left(u_{i+1/2}^n\right) - A\left(u_{i-1/2}^n\right)}{(\Delta x)^2}\right] = 0 \tag{22}$$

The cell-centered pressure p_i^n is solved through Eq. (22) with incomplete Cholesky conjugate gradient iterative method in CFDLib. The advection operator A that has proved very useful for the limiting method is a modified form of the scheme introduced by van Leer [15]:

$$A(u_{i+1/2}) = \left[\tilde{u}_{i+1} \cdot u_{i+1} - \tilde{u}_i \cdot u_i \right] \tag{23a}$$

where:

$$u_{i+1} = \frac{1}{2} \left(u_{i+1/2} + u_{i+3/2} \right) \tag{23b}$$

and

$$\tilde{u}_{i+1} = \begin{cases} u_{i+1/2} + \dfrac{\Delta x}{2} \dfrac{du}{dx}\bigg|_{i+1/2} & u_{i+1} > 0 \\[2ex] u_{i+3/2} - \dfrac{\Delta x}{2} \dfrac{du}{dx}\bigg|_{i+3/2} & u_{i+1} < 0 \end{cases} \tag{23c}$$

with

$$\frac{du}{dx}\bigg|_{i+1/2} = \frac{1}{2\Delta x} \left(u_{i+3/2} - u_{i-1/2} \right)$$

$$\frac{du}{dx}\bigg|_{i+3/2} = \frac{1}{2\Delta x} \left(u_{i+5/2} - u_{i+1/2} \right) \tag{23d}$$

The advection operator can be interpreted as the velocity with which the material flux is formed, given by Eq. (23b). The quantity to be transported, in this case the horizontal momentum per unit mass, is given by Eq. (23c). The expression in Eq. (23c) defines the transported quantity at a cell face as the first two terms in a Taylor series expansion in space about the upstream cell center. The derivative for Eq. (23d) is a second-order numerical estimate of the gradient, also located at the upstream cell center. The face-centered pressure

$p_{i+1/2}^{n}$ which is needed in a finite-volume formulation can also be solved iteratively with Eq.

(22) using velocity data from the $i+1$ and i locations. After obtaining the solutions for

pressure at time $n\Delta t$ at each cell-centered location, the $u_{i+1/2}^{n+1}$ at a new time step can be

updated from Eq. (20) and the u_i^{n+1} from Eq. (21). In addition, the p_i^{n+1} at x_i cell center

location can be obtained from the Eq. (22) with the mentioned iterative method.

3.2.2. Finite Volume Discretization for the Eulerian-Eulerian Models

The continuity (Eq. (1)) and momentum (Eq. (2)) equations are discretized and solved

using the MAC method described in Section 3.2.1. The phasic volume fraction at a new time

step $n+1$ using a cell of volume V can be solved by the discretized continuity equation as:

$$\alpha_\phi^{n+1} = \alpha_\phi^{n} - \frac{\Delta t}{V} A\left(\alpha_\phi^{n}\right) \tag{24}$$

and the condition for the phasic volume fractions is:

$$\alpha_\phi^{n+1} + \alpha_\theta^{n+1} = 1 \tag{25}$$

With the known α_ϕ^{n+1}, the velocity at the $n+1$ step is solved using the MAC method with the

discretized momentum equation shown as follows:

$$\left(\alpha_\phi \vec{u}\right)^{n+1} = \left(\alpha_\phi \vec{u}\right)^{n} - \frac{\Delta t}{V} A\left(\alpha_\phi \vec{u}\right)^{n} - \frac{\Delta t \alpha_\phi^{n}}{V} \sum_a \left(\frac{1}{\rho_\phi} p_{a,c}^{n} - g_a\right) S_a$$

$$+ \frac{\Delta t v_\phi}{V} \sum_a \left(\alpha_\phi\right)_{a,c}^{n} \left(\tilde{D}_\phi\right)_a^{n} \cdot S_a + \frac{\Delta t}{V} \sum_a \left(\tilde{R}_\phi\right)_{a,c}^{n} \cdot S_a + \frac{1}{\rho_\phi} \vec{F}_{\phi\theta}^{n} \tag{26}$$

in which a is the side of the cell, c means central-differencing in the $n\Delta t$ time step, S is the

surface area of the side a, v_ϕ is the kinematic viscosity of the phase ϕ, $\tilde{D}_\phi$ is the mean

deformation rate tensor, expressed as:

$$\left(D_{\phi}\right)_{ij} = \frac{\partial}{\partial x_j}\left(\vec{u}_{\phi}\right)_i + \frac{\partial}{\partial x_i}\left(\vec{u}_{\phi}\right)_j \tag{27}$$

and $\tilde{R}_{\phi}$ is the Reynolds stress tensor, expressed as:

$$\left(R_{\phi}\right)_{ij} = \left(v_{\phi}\right)_t \alpha_{\phi}\left[\left(D_{\phi}\right)_{ij} - \frac{2}{3}\frac{\partial}{\partial x_k}\left(\vec{u}_{\phi}\right)_k \delta_{ij}\right] \tag{28}$$

3.3. Boundary Conditions

The numerical solution of conservation of mass (Eq. (1)) and momentum (Eq. (2)) requires specified boundary conditions. Three important boundary conditions are described in this section. CFDLib uses the ghost cell, a cell that is outside the computational mesh, to treat the boundary condition.

3.3.1 No-Slip Condition

The no-slip boundary condition is specified at the wall of the two-phase flow for the phasic velocity $\vec{u}_{\phi}$. The velocity $\vec{u}_{\phi}$ is equal to $-\vec{u}_{\phi,\mathrm{int}}$ at the cell-center of ghost cell where subscript "int" refers to the interior cell that is adjacent to the ghost cell. As a result, the zero velocity condition will be specified at the boundary of the interior cell that coincides with the cell-face of ghost cell by the equation:

$$\vec{u}_{wall} = \frac{-\vec{u}_{\phi,\mathrm{int}} + \vec{u}_{\phi,\mathrm{int}}}{2} = 0 \tag{29}$$

3.3.2 Inflow Condition

At the inflow boundary, the specified values of the velocity will be placed at the cell-center of the ghost cell. For example, if the right side of a cell (i,j) coincides with a specified inflow boundary, the velocity at the boundary is expressed as:

$$\vec{u}_{i+1,j} = \vec{u}_o \tag{30}$$

where $\vec{u}_o$ is the specified inflow velocity such as the inlet superficial gas velocity that is

defined as the gas volume flow rate divided by the cross-sectional area of the distributor plate.

3.3.3 Zero-Gradient Outflow Condition

The zero-gradient outflow condition is specified at the outlet of the bubble column or

external loop airlift reactors. The term zero-gradient means that there is no spatial gradient in

the state vector at the outflow boundary. For example, if the right side of a cell (*i,j*) coincides

with an outflow boundary, the zero-gradient specifications of velocity and pressure are given

by:

$$\vec{u}_{i+1,j} = \vec{u}_{i,j} \tag{31}$$

$$p_{i+1,j} = p_{i,j} \tag{32}$$

References

[1]	Kashiwa, B.A., Padial, N.T., Rauenzahn, R.M., VanderHeyden, W.B., 1993, "Cell-centered ice method for multiphase flow simulations", Department of Energy, Washington, DC. Report: LA-UR-93-3922.

[2]	Kashiwa, B. A., and Rauenzahn, R. M. 1994, "Multimaterial formalism", Department of Energy, Washington, DC. Report: LA-UR-94-771; CONF-940659-6.

[3]	Crowe, C.T., Sommerfeld, M., Tsuji, Y., 1998, "Multiphase Flows with Droplets and Particles", CRC Press, pp. 81-83.

[4]	White, F.M., Viscous fluid flow, McGraw-Hill, New York, 1974.

[5]	Schiller, L., and Naumann, A., 1933. Uber die grundlegenden berechnungen bei der schwerkraftaufbereitung. Zeitung des vereins deutscher ingenieure, 77- 318.

[6]	Kashiwa, B.A., 1998, "An Extended k-epsilon Turbulence Model for Multiphase Flow", Department of Energy, Report: LA-UR-98-2923.

[7]	Padial, N.T., VanderyHeyden, W.B., Rauenzahn, R.M., Yarbro, S.L., 2000, "Three-Dimensional Simulation of a Three-Phase Draft-Tube Bubble Column", Chemical Engineering Science, 55 (16), pp. 3261-3273.

[8]   Launder, B.E., and Spalding, D.B., 1974, "The Numerical Computation of Turbulent Flows", Computer Methods in Applied Mechanical Engineering, 3, pp. 269-289.

[9]   Padial, N.T., VanderyHeyden, W.B., Rauenzahn, R.M., Yarbro, S.L., 2000, "Three-Dimensional Simulation of a Three-Phase Draft-Tube Bubble Column", Chemical Engineering Science, 55 (16), pp. 3261-3273.

[10] Launder, B.E., and Spalding, D.B., 1974, "The Numerical Computation of Turbulent Flows", Computer Methods in Applied Mechanical Engineering, 3, pp. 269-289.

[11] Batchelor, G.K., 1988, "A New Theory of the Instability of a Uniform Fluidized Bed", Journal of Fluid Mechanics, 193, pp.75-110.

[12] Biesheuvel A, and Gorissen WCM, 1990, "Void Fraction Disturbances in a Uniform Bubbly Fluid", International Journal of Multiphase Flow, 16, pp. 211-231.

[13] Sato, Y., Sadatomi, M., and Sekoguchi, K., 1981, "Momentum and Heat Transfer in Two-Phase Bubble Flow I", International Journal of Multiphase Flow, 7, pp. 167-177.

[14] Harlow, F.H., and Welch, J.E., 1965, "Numerical Calculation of Time-Dependent Viscous Incompressible Flow of Fluid with Free Surface", the Physics of Fluids, 8 (12), pp. 2182-2189.

[15] van Leer, B., 1977, "Towards the Ultimate Conservative Difference Scheme. IV. A New Approach to Numerical Convection", Journal of Computational Physics, 23, pp. 276-299.

CHAPTER 4. MODEL VALIDATION FOR LOW AND HIGH SUPERFICIAL GAS VELOCITY BUBBLE COLUMN FLOWS

A paper published in Chemical Engineering Science[*].

Deify Law[1], Francine Battaglia, [1] and Theodore J. Heindel[2]
Department of Mechanical Engineering
[1]Virginia Polytechnic Institute and State University, Blacksburg, VA 24061
[2]Iowa State University, Ames, IA 50011

Abstract

In the present work, gas-liquid flow dynamics in a bubble column are simulated with CFDLib using an Eulerian-Eulerian ensemble-averaging method in a two-dimensional Cartesian system. The two-phase flow simulations are compared to experimental measurements of a rectangular bubble column performed by Mudde et al. and a cylindrical bubble column performed by Rampure et al. for low and high superficial gas velocities, respectively. The objectives are to obtain grid-independent numerical solutions using CFDLib to reconcile unphysical results observed using FLUENT with increasing grid resolutions, and to validate computational fluid dynamics simulations with experimental data to demonstrate the use of numerical simulations as a viable design tool for gas-liquid bubble column flows. Numerical predictions are presented for the local time-averaged liquid velocity or gas fraction at various axial heights as a function of horizontal or radial position. The effects of grid resolution, bubble pressure model, and drag coefficient models on the numerical predictions are examined. The bubble pressure model is hypothesized to account for bubble stability, thus providing physical solutions.

4.1. Introduction

Bubble column reactors are widely used in the chemical industry due to their excellent heat and mass transfer characteristics, simple construction, and ease of operation. As reactors, they are used in a variety of chemical processes, such as Fischer-Tropsch synthesis, manufacture of fine chemicals, oxidation and alkylation reactions, effluent treatment, coal liquefaction, and fermentation reactions [1]. Bubble column hydrodynamics are studied experimentally and computationally for scale-up and design considerations. The performance of bubble column reactors depends on the gas holdup (volumetric gas fraction), bubble size, bubble rise velocity, bubble-bubble interactions, and mixing rate [2, 3]. Full-scale experimentation in bubble columns is expensive and therefore a more cost-effective approach to exploring these reactors is by using validated computational fluid dynamics (CFD) models.

Numerical simulations of bubble columns either employing Eulerian-Eulerian models [1, 4, 5, 6], Eulerian-Lagrangian models [7, 8, 9], or volume of fluid (VOF) [10] methods were surveyed. The Eulerian-Eulerian model treats dispersed (gas bubbles) and continuous (liquid) phases as interpenetrating continua, and describes the motion for gas and liquid phases in an Eulerian frame of reference. Sokolichin and Eigenberger [6], Pan and Duduković [5] and Monahan et al. [4] performed two-dimensional (2D) simulations of gas-liquid flows for a rectangular bubble column using an Eulerian-Eulerian approach. Sokolichin and Eigenberger [6] and Pan and Duduković [5] predicted time-averaged axial liquid velocity and reported that the liquid primarily traveled up the column center and reduced gas holdup with liquid downflow at the walls. Monahan et al. [4] demonstrated that the two-fluid model can predict flow transitions in bubble columns successfully. Other

investigators such as Rampure et al. [11], who conducted three-dimensional (3D) simulations, and Sanyal et al. [1]), who conducted axisymmetric simulations of a cylindrical bubble column reactor, used the Eulerian-Eulerian method as well. It should be noted that both Rampure et al. [11] and Sanyal et al. [1] conducted experiments in addition to numerical simulations and the time-averaged gas holdup simulations compared qualitatively with the experiments.

In the Eulerian-Lagrangian model, the continuous phase is described in an Eulerian representation while the dispersed phase is treated as discrete bubbles and each bubble is tracked by solving the equations of motion for individual bubbles. Delnoij et al. [7, 8, 9] applied an Eulerian-Lagrangian method to simulate detailed bubble-bubble interactions along with interfacial forces in the laminar bubbly flow regime. They predicted a distinct bubble plume and a time-dependent, multiple staggered vortex mode of circulation that characterized the liquid phase of the bubble column. The computed flow structure qualitatively compared with the experimentally observed flow patterns.

The VOF method solves the instantaneous Navier-Stokes equations to obtain the gas and liquid flow field with an extremely high spatial resolution. The evolution of the gas-liquid interface is tracked using a volume-tracking scheme. Lin et al. [10] used the VOF method to provide time-dependent behavior of a dispersed bubbling flow and to account for the coupling effects of the pressure field and the liquid velocity on the bubble motion based on their 2D bubble column simulations. The computational results indicated the unsteady nature of the flow due to the coupling effects of the pressure field, liquid velocity, and bubble motion. The numerical results compared well both qualitatively and quantitatively with experiments [10].

The main advantage of the Eulerian-Lagrangian formulation comes from the fact that each individual bubble is modeled, allowing consideration of additional effects related to bubble-bubble and bubble-liquid interactions. Mass transfer with and without chemical reaction, bubble coalescence and redispersion, in principle, can be added directly to an Eulerian-Lagrangian hydrodynamic model. The Eulerian-Lagrangian approach, which requires tracking the dynamics of each bubble, is usually applied to cases where a small number of bubbles exist, such as when the superficial gas velocity is low, due to computer limitations. On the other hand, the Eulerian-Eulerian method is often used because memory storage requirements and demand of computer power depend on the number of computational cells considered instead of the number of bubbles. The Eulerian-Eulerian approach can be applied to cases for low and high superficial gas velocities. The disadvantage of using the Eulerian-Eulerian method is that the bubble-bubble and bubble-liquid interactions cannot be considered as straightforward as the Eulerian-Lagrangian method. The VOF method is the most detailed model used to advance the gas-liquid interface through the flow field in an Eulerian mesh and does not require empirical constitutive equations. However, the VOF method is limited to a small number of bubbles, e.g., less than ~10 bubbles in the flow field, due to computational limitations. Most industrial applications require high superficial gas velocities and therefore the Eulerian-Eulerian method is preferred [5].

Law et al. [12] computationally studied bubble column hydrodynamics using the Eulerian-Eulerian method formulated in FLUENT. Unphysical results were observed with increasing grid resolutions, therefore prohibiting a conclusive grid resolution study. An alternate multiphase FORTRAN code, CFDLib, developed at Los Alamos National

Laboratory, is tested in the present work. The hypothesis is that a bubble pressure (BP) model will provide numerical stability and more accurately represent the bubble phase in order to resolve the flow field correctly. For example, Monahan et al. [4] reported that the BP model provided a uniform time-averaged gas holdup profile across the bubble column in the low superficial gas velocity flow regime. The influence of closure models for drag and virtual mass used within the framework of CFDLib was investigated by Rafique and Duduković [13] for bubble column flows. Their findings showed most correlations agreed well with experimental data found in the literature, but they were unable to recommend a specific model due to the lack in accurately measured gas holdup profiles.

In the present work, the gas-liquid flow dynamics in a bubble column are simulated using CFDLib in two-dimensional Cartesian coordinates and compared to previous results using FLUENT. The two-phase flow simulations are compared to the experimental measurements of a cylindrical bubble column with a high superficial gas velocity performed by Rampure et al. [11], and a rectangular bubble column with a low superficial gas velocity performed by Mudde et al. [14]. Numerical predictions are presented for the time-averaged phase variables at various axial heights as a function of radial or horizontal position. The effects of grid resolution, bubble pressure model, and drag coefficient model on the numerical predictions are also examined. The specific objectives of this study are to obtain grid-independent numerical solutions and to validate the CFD simulations with the published experimental data in order to demonstrate the use of numerical simulations as a viable design tool.

4.2. Numerical Formulation

4.2.1. Governing Equations

CFDLib, a FORTRAN code developed at Los Alamos National Laboratory, uses a finite-volume technique to integrate the time-dependent equations of motion that govern multiphase flows. The code is based on an Arbitrary Lagrangian-Eulerian (ALE) scheme as described by Hirt et al. [15]. The name ALE refers to the flexibility of the scheme, which allows for the mesh either to be moved along with the fluid (Lagrangian), to remain in a fixed position (Eulerian), or to be moved in another fashion as selected by the user. The ALE scheme is designed to handle flows at any flow speed, including incompressible and hypersonic flows, and allows for multiphase calculations for an arbitrary number of fluid fields. The two-fluid Eulerian-Eulerian model is employed to represent each phase as interpenetrating continua and the conservation equations for mass and momentum for each phase are ensemble-averaged. The subscript c refers to the continuous (liquid water) phase and the subscript d refers to the dispersed (air bubble) phase. The continuity equations for each phase, neglecting mass transfer, are:

$$\frac{\partial}{\partial t}(\alpha_c \rho_c) + \nabla \cdot (\alpha_c \rho_c \vec{u}_c) = 0 \tag{1}$$

$$\frac{\partial}{\partial t}(\alpha_d \rho_d) + \nabla \cdot (\alpha_d \rho_d \vec{u}_d) = 0 \tag{2}$$

The momentum equations for each phase are:

$$\frac{\partial}{\partial t}(\alpha_c \rho_c \vec{u}_c) + \nabla \cdot (\alpha_c \rho_c \vec{u}_c \vec{u}_c) = -\alpha_c \nabla p + \nabla \cdot \overline{\overline{\tau}}_c + \vec{K}_{dc}(\vec{u}_d - \vec{u}_c) + \vec{F}_{vm} + \rho_c \alpha_c \vec{g} \tag{3}$$

$$\frac{\partial}{\partial t}(\alpha_d \rho_d \vec{u}_d) + \nabla \cdot (\alpha_d \rho_d \vec{u}_d \vec{u}_d) = -\alpha_d \nabla p + \nabla \cdot \overline{\overline{\tau}}_d + \vec{K}_{cd}(\vec{u}_c - \vec{u}_d) - \vec{F}_{vm} + \rho_d \alpha_d \vec{g} \tag{4}$$

The terms on the right hand side of Eqs. (3) and (4) represent, from left to right, the pressure gradient, effective stress, interfacial momentum exchange (drag and virtual mass forces), and the gravitational force. The closures for turbulence modeling and interfacial momentum exchange are discussed next.

4.2.2. Turbulence Modeling

Turbulence contributions for the continuous and the dispersed phases are modeled through a set of modified standard k-ε equations that calculate the turbulence generated at the gas-liquid interface in the form of a slip-production energy term [16, 17]. The modified k-ε equations are used only for the high superficial gas velocity case and the equations for a general phase k are:

$$\frac{\partial}{\partial t}(\alpha_k \rho_k k_k) + \nabla \cdot (\alpha_k \rho_k k_k \vec{u}_k) = \nabla \cdot \left(\alpha_k \frac{\mu_{t,k}}{\sigma_k} \nabla k_k \right) + \alpha_k G_k - \alpha_k \rho_k \varepsilon_k + \sum_{l \neq k} \beta_{kl} K_{kl} \left| \vec{u}_k - \vec{u}_l \right|^2 + 2 \sum_{l \neq k} E_{kl} (k_l - k_k)$$

(5)

$$\frac{\partial}{\partial t}(\alpha_k \rho_k \varepsilon_k) + \nabla \cdot (\alpha_k \rho_k \varepsilon_k \vec{u}_k) = \nabla \cdot \left(\alpha_k \frac{\mu_{t,k}}{\sigma_\varepsilon} \nabla \varepsilon_k \right) + \alpha_k \frac{\varepsilon_k}{k_k} (C_{1\varepsilon} G_k - C_{2\varepsilon} \rho_k \varepsilon_k) + \frac{1}{\tau_{kl}} \left\{ \sum_{l \neq k} \beta_{kl} K_{kl} \left| \vec{u}_k - \vec{u}_l \right|^2 \right\}$$

(6)

where

$$\mu_{t,k} = \rho_k C_{\mu,k} \frac{k_k^2}{\varepsilon_k}$$

(7)

$$G_k = \mu_{t,k} (\nabla \vec{u}_k + (\nabla \vec{u}_k)^T) : \nabla \vec{u}_k$$

(8)

$$C_{\mu,k} = \frac{C_\mu}{1 + (2 \sum_{l \neq k} E_{kl} k_k) / (\rho_k \varepsilon_k)}$$

(9)

The form of Eq. (9) models a return-to-isotropy effect due to fluctuating interfacial momentum coupling and reduces the turbulent viscosity from that predicted by the single-phase model. The turbulence energy exchange rate coefficient E_{kl} is given by:

$$E_{kl} = \alpha_k \alpha_l \left(\frac{\rho_k \rho_l}{\rho_k + \rho_l} \right) \frac{\sqrt{k_k + k_l}}{d_b} \left(1 + \text{Re}^{0.6} \right).$$

(10)

Re is the bubble Reynolds number and the expression will be discussed in section 2.4.

The first three terms on the right hand side of Eq. (5) account for turbulent diffusion, mean flow shear production, and decay of turbulence kinetic energy of phase k. The fourth term on the right hand side of Eq. (5) accounts for production of turbulence energy from slip between phases. The coefficient β_{kl} is given by:

$$\beta_{kl} = \frac{a_k}{a_k + a_l}$$

(11)

where

$$a_k = \frac{\alpha_k^{1/3}}{\rho_k + \rho_c}$$

(12)

and ρ_c is the continuous phase density. The last term in Eq. (5) accounts for the exchange of turbulence energy among phases.

The first three terms on the right hand side of Eq. (6) account for the diffusion of turbulence dissipation, the mean flow velocity gradient production term, and the homogeneous dissipation term. The last group of terms in Eq. (6) describes the effect of interfacial momentum transfer on the production of turbulence dissipation. The time constant τ_{kl} is given by the following empirical correlation:

$$\tau_{kl} = \left\{ 0.01 C_{2\varepsilon} (\alpha_k \alpha_l)^{0.086} \left[\frac{\rho_k \left| \vec{u}_k - \vec{u}_l \right| d_b}{\mu_k} \right]^{0.562} \frac{\left| \vec{u}_k - \vec{u}_l \right|}{d_b} \right\}^{-1} \tag{13}$$

This correlation was obtained by fitting predictions of turbulence kinetic energy to data from experiments on homogeneous sedimenting and bubbly systems [18, 19, 20, 21]. The term K_{kl} is the momentum exchange coefficient and the model will be discussed in section 2.3. Equations (7) and (8) are closure models for the turbulent viscosity $\mu_{t,k}$ and the production of turbulent kinetic energy G_k of phase k. The turbulent parameters are set using standard empirical values for k-ε turbulence modeling where $C_{1\varepsilon} = 1.44$, $C_{2\varepsilon} = 1.92$, $C_\mu = 0.09$, $\sigma_k = 1.0$, and $\sigma_\varepsilon = 1.3$.

4.2.3. Interfacial Momentum Exchange

The interfacial momentum exchange terms in the momentum conservation equations for each phase consist of drag and virtual mass force terms. The drag force for the gas and liquid is modeled, respectively, as:

$$\vec{K}_{cd}(\vec{u}_c - \vec{u}_d) = \frac{3}{4} \rho_c \alpha_d \alpha_c \frac{C_D}{d_b} \left| \vec{u}_c - \vec{u}_d \right| (\vec{u}_c - \vec{u}_d)$$

$$\vec{K}_{dc}(\vec{u}_d - \vec{u}_c) = \frac{3}{4} \rho_c \alpha_d \alpha_c \frac{C_D}{d_b} \left| \vec{u}_d - \vec{u}_c \right| (\vec{u}_d - \vec{u}_c) \tag{14}$$

where C_D is the drag coefficient. The virtual mass force $\vec{F}_{vm}$ is modeled as:

$$\vec{F}_{vm} = 0.5 \alpha_d \rho_c \left(\frac{d\vec{u}_c}{dt} - \frac{d\vec{u}_d}{dt} \right) \tag{15}$$

and the coefficient of 0.5 is used for a spherical bubble.

4.2.4. Drag Coefficient Model

Two drag coefficient models are used in this study for gas-liquid flows. The drag coefficient model proposed by Schiller and Naumann [22] is:

$$C_D = \begin{cases} 24(1+0.15\,\text{Re}^{0.687})/\text{Re} & \text{Re} \leq 1000 \\ 0.44 & \text{Re} > 1000 \end{cases} \tag{16}$$

where $\text{Re} = \rho_c |\vec{u}_d - \vec{u}_c| d_b / \mu_c$ is the bubble Reynolds number based on a characteristic (effective) bubble diameter, relative velocity between the two phases, and the liquid density and dynamic viscosity. Another drag coefficient relation proposed by White [23] and used in this study is expressed by:

$$C_D = C_\infty + \frac{24}{\text{Re}} + \frac{6}{1+\sqrt{\text{Re}}} \qquad 0 \leq \text{Re} \leq 2 \times 10^5 \tag{17}$$

where C_∞ is the drag coefficient when the bubble Reynolds number goes to infinity. In our calculation C_∞ is set to 0.5.

4.2.5. Bubble Pressure Model

The bubble pressure (BP) model represents the transport of momentum arising from bubble-velocity fluctuations, collisions, and hydrodynamic interactions. The BP model is reported in the literature to play an important role in bubble-phase stability [24]. Biesheuvel and Gorissen [25] proposed a bubble pressure model of the form:

$$P_d = \rho_c C_{BP} \alpha_d (u_d - u_c)(u_d - u_c) \left(\frac{\alpha_d}{\alpha_{dcp}} \right) \left(1 - \frac{\alpha_d}{\alpha_{dcp}} \right) \tag{18}$$

The gradient of Eq. (18) is added to the right hand side of the gas momentum Eq. (4). A positive value of $dP_d/d\alpha_d$ acts as a driving force for bubbles to move from areas of higher α_d to areas of lower α_d and facilitates stabilization of the bubbly-flow regime. The virtual mass

coefficient C_{BP} of an isolated spherical bubble is 0.5. The bubble pressure is proportional to the slip velocity and gas holdup. The gas holdup at close packing α_{dcp} is set equal to 1.0 in this study.

As we will show for the low superficial gas velocity case, the BP model must be employed with a bubble induced turbulence (BIT) model to obtain numerical stability at high grid resolutions. Sato et al. [26] proposed a BIT model proportional to the bubble diameter and slip velocity of the rising bubbles:

$$\mu_{t,c} = \rho_c C_{BT} \alpha_d d_b \left| \vec{u}_d - \vec{u}_c \right| \tag{19}$$

where the value of the proportionality constant C_{BT} is 0.6. Equation (19) replaces Eq. (7) when the BIT model is applied. The BIT model yields an effective viscosity in the liquid (continuous) phase that is the sum of the molecular viscosity of the continuous phase and the turbulent viscosity calculated from the BIT model, whereas the effective viscosity for the dispersed phase is assumed to equal the molecular viscosity of the dispersed phase.

4.2.6. Simulation Conditions

The Marker and Cell (MAC) method has been selected in CFDLib to solve the incompressible gas-liquid two-phase flow. A velocity inlet boundary condition is used to introduce gas flow uniformly at the bottom of the bubble column. A no-slip boundary condition is applied for both phases at the walls and ambient pressure is specified at the top of the domain. The convergence criterion is set to 1×10^{-8} for all dependent variables. All simulations use a time step according to the Courant-Friedrich-Lewy (CFL) stability criterion to march the solution forward and the results are time-averaged from 20 to 90 s, which includes 7000 time realizations. To be consistent with the findings of Rampure et al. [11] and

45

Mudde et al. [14], an effective bubble size of 0.5 cm is used to represent the dispersed gas phase.

4.3. Results and Discussion

4.3.1. High Superficial Gas Velocity

Simulations are performed to match the experimental conditions of Rampure et al. [11] for a cylindrical bubble column with $H_d = 1.0$ m and $W = 0.2$ m, as shown in Figure 4.1. The static water height (H_c) in the column is 1.0 m and air flows uniformly through the bottom of the column at 0.1 m/s. The geometry in Figure 4.1 is modeled in Cartesian coordinates as a 2D slice through the centerplane of the cylinder. The application of a 2D Cartesian simulation has been shown to provide adequate representation of the flow physics when compared to 3D cylindrical or rectangular bubble column simulations [4, 12].
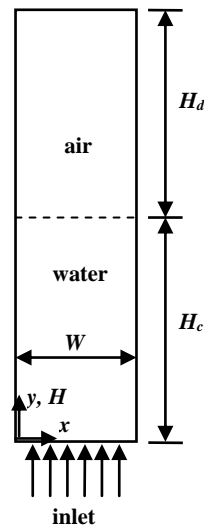
Figure 4.1. Schematic of the simulation domain used in this study.

46

4.3.1.1. Grid Resolution Study

Six different grid resolutions are tested using CFDLib to simulate the 2D representation of the domain in Figure 4.1. The number of computational cells along the horizontal and vertical directions is increased while maintaining a square computational cell; a summary of grid resolutions is presented in Table 4.1. The effects of grid resolution on the numerical predictions of the time-averaged gas holdup are examined and compared to previous results by the authors using FLUENT [12]. For the FLUENT and CFDLib simulations, the Schiller-Naumann drag coefficient model is used.

Figure 4.2 shows the predictions of the time-averaged gas holdup using FLUENT for axial locations of H = 0.15 m and 0.65 m above the distributor plate [12]. Results from the experiments of Rampure et al. [11] are compared to the simulations for varying grid resolution, and the simulations are plotted in terms of $r = x/2$. FLUENT best predicts the experimental data using the 30×300 grid resolution whereas the 10×100 grid resolution gives completely unphysical flow dynamics that fail to capture experimental phenomena. For the cases of 15×150 and 20×200 cells, the numerically predicted values overestimate the maximum gas holdup at the centerline and underestimate it toward the walls. Grid independent solutions for this gas-liquid bubble column flow were not obtained [12]. FLUENT was not able to satisfy convergence for the resolution of 60×600 cells, even with a small time step size of 0.0001 s. The radial profiles for all predicted time-averaged gas holdup values using FLUENT are generally symmetric, except for the lowest resolution case of 10×100 cells.

Table 4.1. Number of cells and cell size *x*- and *y*-directions for the high superficial gas velocity simulations.

# cells ($x \times y$)	$\Delta x = \Delta y$ (cm)
10×100	2.00
15×150	1.33
20×200	1.00
30×300	0.66
40×400	0.50
60×600	0.33
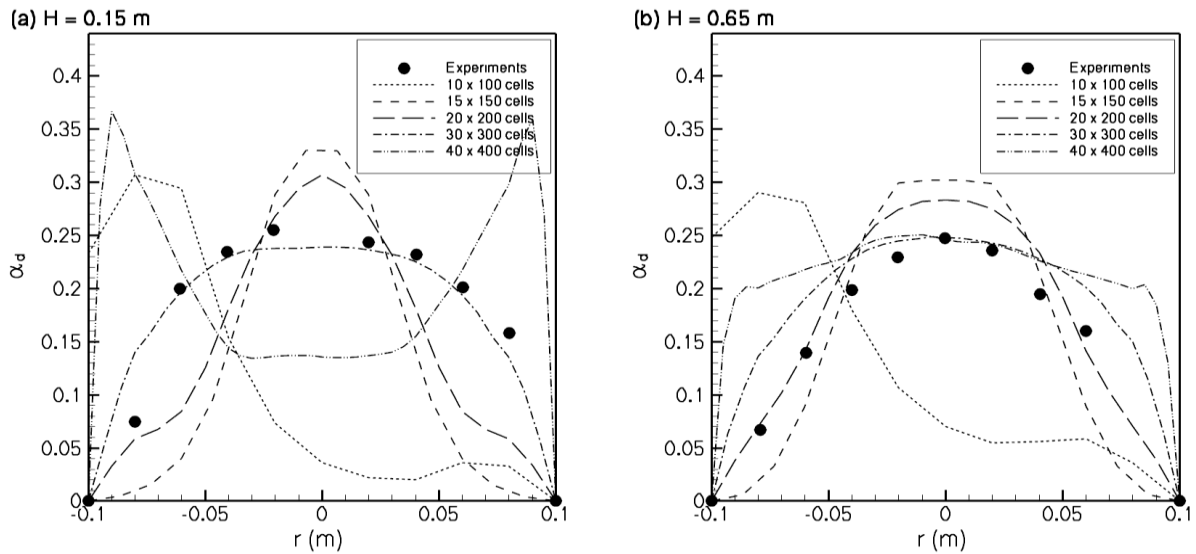
Figure 4.2.   Time-averaged gas holdup versus radial position, comparing FLUENT simulations [12] using different grid resolutions to experimental data by Rampure et al. [11] at heights of (a) H = 0.15 m and (b) H = 0.65 m.
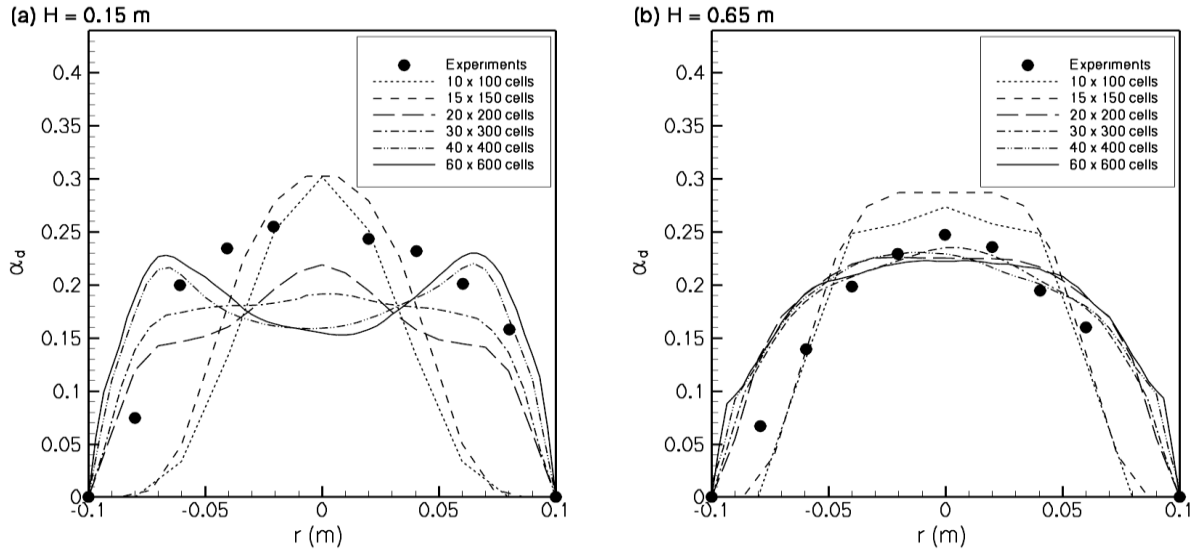
Figure 4.3. Time-averaged gas holdup versus radial position, comparing CFDLib simulations using different grid resolutions to experimental data by Rampure et al. [11] at heights of (a) H = 0.15 m and (b) H = 0.65 m.

Similar trends are observed from the CFDLib simulations, shown in Figure 4.3 for axial heights of H = 0.15 m and 0.65 m. At low axial heights, both FLUENT (Figure 4.2a) and CFDLib (Figure 4.3a) overpredict the gas holdup near the centerline for low grid resolutions, e.g., 15×150 grid cells. For higher grid resolutions such as 40×400 cells, both codes predict two local maxima for the gas holdup. The gas holdup predictions using CFDLib at H = 0.65 m (Figure 4.3b) indicate grid convergence for the 4 largest grid resolutions, which was not observed when using FLUENT. Figure 4.4 presents time-averaged gas holdup contours for both FLUENT and CFDLib that elucidate the large gas-deficient region in the center of the column near the inlet.

49
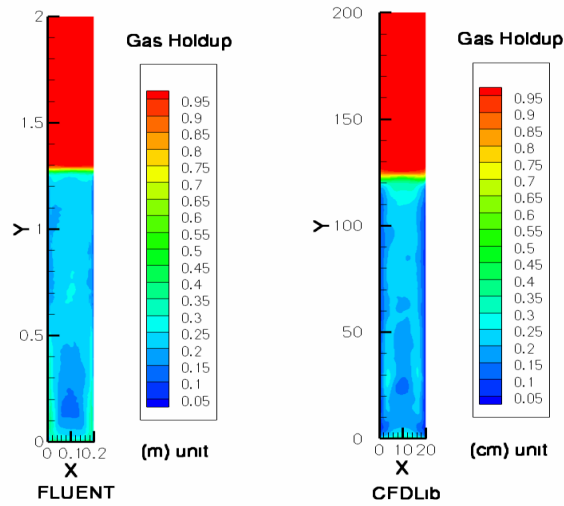
Figure 4.4. Time-averaged gas holdup contour plot, comparing FLUENT with CFDLib simulations for the high superficial gas velocity case and 40 × 400 cells.

4.3.1.2. Bubble Pressure Model Study

The effect of the bubble pressure model using CFDLib is examined to determine how it affects flow stability. The grid resolutions shown in Table 4.1 are used and new simulations for the time-averaged gas holdup evoking the BP model are presented below. Figure 4.5a shows that as grid resolutions become finer, two off-center high gas holdup regions are observed, which is similar to the FLUENT simulations (Figure 4.2a) and CFDLib simulations without the BP model (Figure 4.3a) at the lower axial height. The influence of the BP model at the higher axial height (Figure 4.5b) is also negligible. Figure 4.6 directly compares simulations with and without the BP model for several grid resolutions. It is interesting to note that gas holdup predictions at the higher axial location are very similar with and without the BP model for the 3 largest grid resolutions. A grid resolution of 80 × 800 was also tested using CFDLib but the simulations diverged, even with the BP model. The previous work of Law et al. [12] suggested that cell sizes smaller than the effective bubble diameter may cause numerical stability issues and result in a diverged simulation.

50
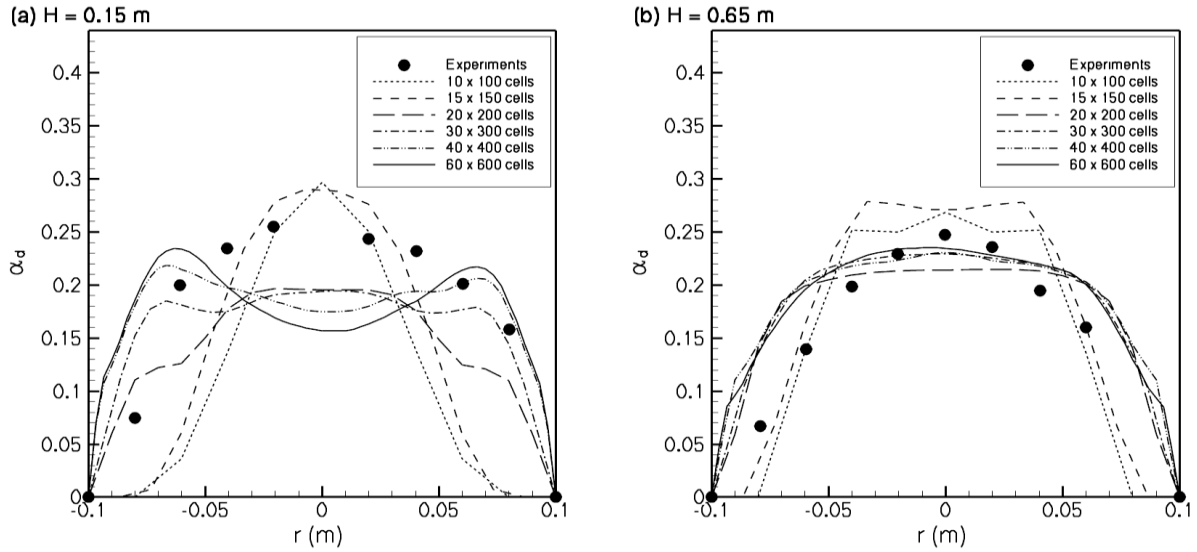
Figure 4.5. Time-averaged gas holdup versus radial position, comparing CFDLib simulations using the bubble pressure model to experimental data by Rampure et al. [11] at heights of (a) H = 0.15 m and (b) H = 0.65 m.

4.3.1.3. Drag Coefficient Model Study

Drag coefficient models are investigated to determine the effects on gas holdup. The grid resolution for this portion of the study is 40×400 grid cells and the bubble pressure model is not employed. Figure 4.7 presents the predicted time-averaged gas holdup for the Schiller-Naumann and White models at two axial heights. The White model compares very well with the experimental results [11] at the lower axial height. However, the Schiller-Naumann model compares qualitatively better to experiments than the White model at the higher axial liquid height, predicting a more parabolic profile (Figure 4.7b). As an additional comparison, Figure 4.8 presents predictions using CFDLib employing the White model, with and without the bubble pressure model. It is evident that the BP model has no discernible affects on the bubble dynamics. In general, the time-averaged gas holdup profiles are more homogeneous using the White model as compared to the Schiller-Naumann model.
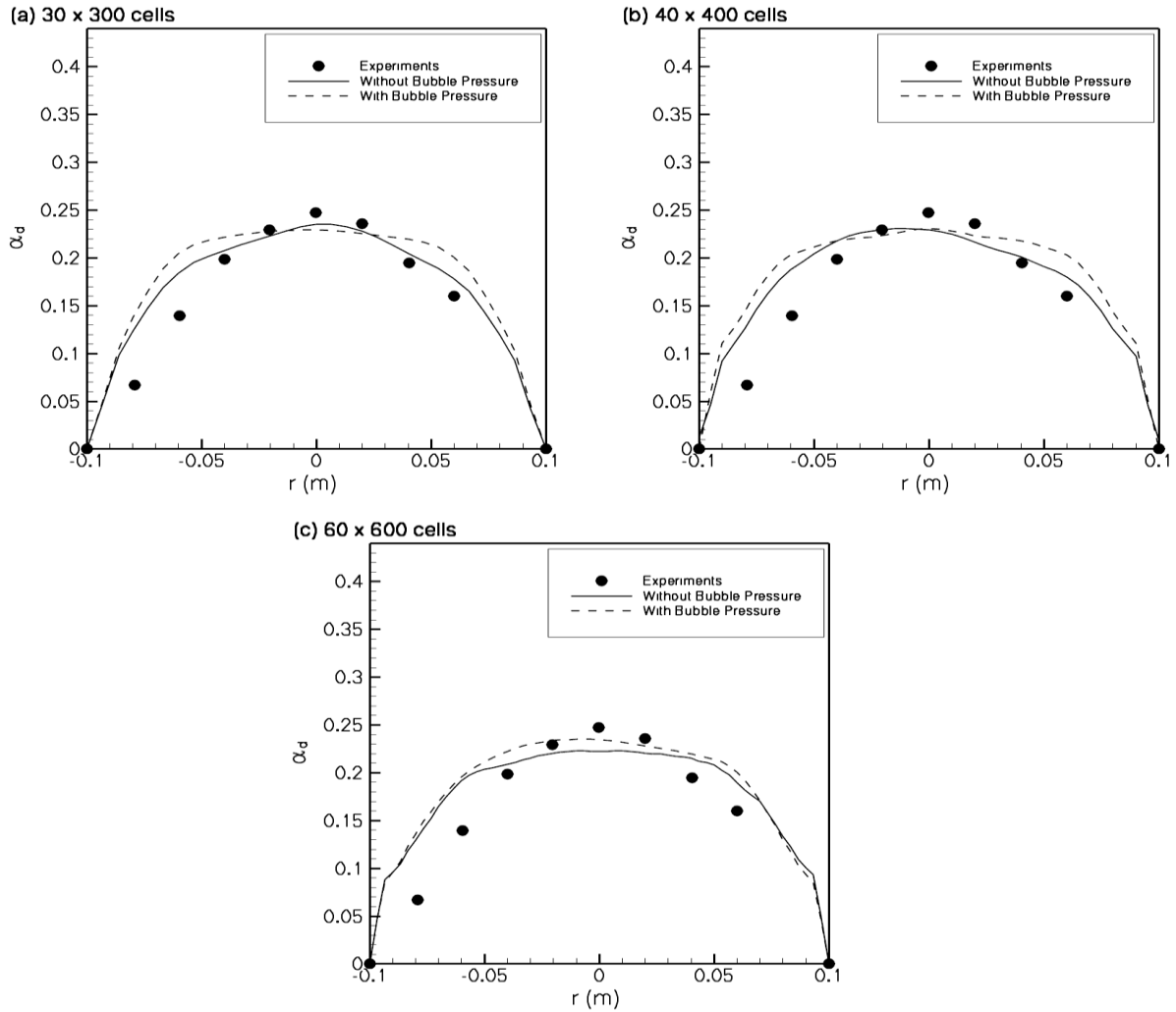
Figure 4.6. **Time-averaged gas holdup versus radial position, comparing CFDLib simulations with and without the bubble pressure model to experimental data by Rampure et al. [11] at a height of H = 0.65 m using (a) 30 × 300, (b) 40 × 400 and (c) 60 × 600 grid cells.**
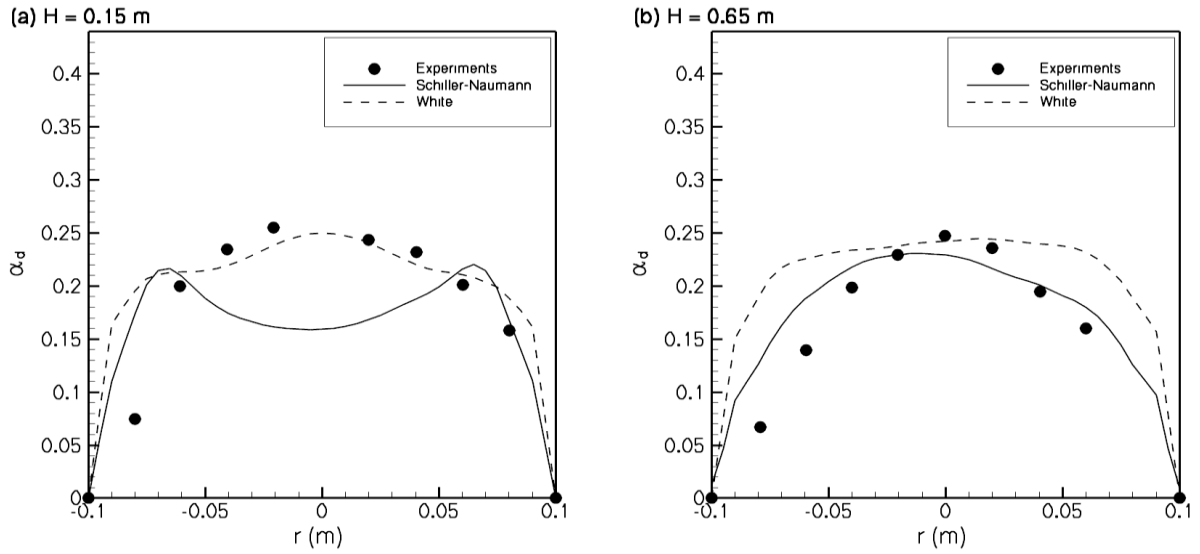
Figure 4.7. **Time-averaged gas holdup versus radial position, comparing CFDLib simulations using the Schiller-Naumann and White drag coefficient models for 40 × 400 grid cells without using the BP model to experimental data by Rampure et al. [11] at heights of (a) H = 0.15 m and (b) H = 0.65 m.**
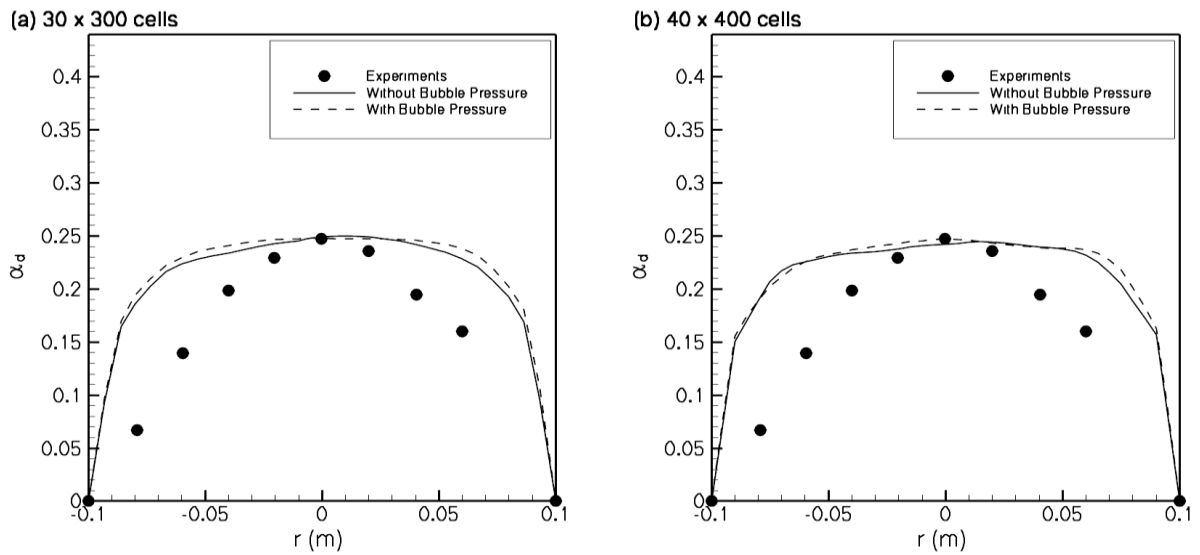
Figure 4.8. **Time-averaged gas holdup versus radial position, comparing CFDLib simulations using the White drag coefficient model with and without the BP model to experimental data by Rampure et al. [11] at a height of H = 0.65 m using (a) 30 × 300 and (b) 40 × 400 grid cells.**

Figure 4.9 presents time-averaged gas holdup contours for a grid resolution of 40 × 400 cells without using the BP model, comparing the two drag models. Two high gas holdup

regions form off-center using the Schiller-Naumann model at lower axial heights, whereas the White model predicts a more homogeneous gas holdup throughout the entire liquid bed. Furthermore, the bed expansion is higher with the White model than with the Schiller-Naumann model. The results suggest that the accuracy of the drag models may be dependent on the flow regime and further studies in the next section will further explore this notion.
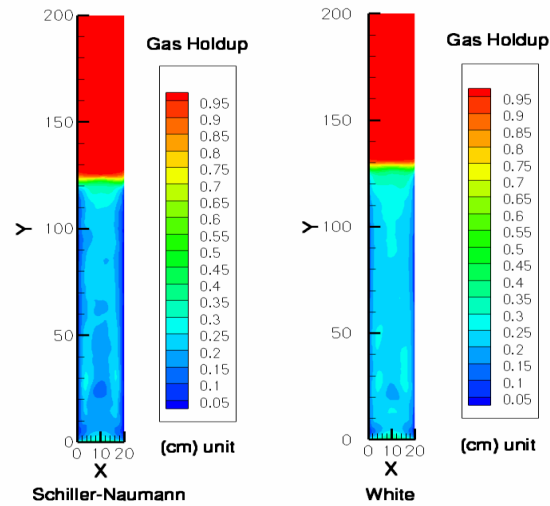
Figure 4.9. **Time-averaged gas holdup contour plots comparing CFDLib simulations using Schiller-Naumann and White drag coefficient models for 40 × 400 grid cells without using the BP model.**

4.3.2. Low Superficial Gas Velocity

Simulations are performed to match the experimental conditions of Mudde et al. (1997) for a rectangular bubble column that is H_c = 1.1 m, H_d = 0.4 m, and W = 0.15 m (see Figure 4.1). The rectangular column used in the experiments of Mudde et al. [14] had a depth of 0.0127 m; however, in the present study the column is modeled in a two-dimensional (2D) Cartesian system. Air flows uniformly through the bottom of the column at 0.01 m/s, which is 10 times slower than the high superficial gas velocity case.

4.3.2.1. Grid Resolution Study

Three different grid resolutions are tested using FLUENT and CFDLib to simulate the 2D representation of the Mudde et al. [14] domain in Figure 4.1. The effects of grid resolution on the numerical predictions of the time-averaged gas holdup are examined employing the Schiller-Naumann drag coefficient model without using the BP model. The number of computational cells along the horizontal and vertical directions is increased while maintaining a square computational cell. Table 4.2 shows that for the coarse and medium grid resolutions, where the cell size is larger than the effective bubble diameter (0.5 cm), the simulations converge regardless of numerical code using the Schiller-Naumann drag coefficient model without the BP model. However, neither FLUENT nor CFDLib are able to predict a converged solution for 60 × 600 cells when using the Schiller-Naumann drag model without the BP model.

Table 4.2. Grid resolutions and models tested for the low superficial gas velocity case.

Grid Resolution	Cell Size (cm)	FLUENT SN Drag	CFDLib SN Drag			CFDLib White Drag		
			Without BP	BP	BP and BIT	Without BP	BP	BP and BIT
15 × 150	1.00	C	C	C	C	C	C	C
30 × 300	0.50	C	C	C	C	C	C	C
60 × 600	0.25	D	D	D	C	D	D	C

        Key: SN – Schiller-Naumann
             BP – Bubble pressure model
             BIT – Bubble induced turbulence model
             C – Converged solution
             D – Diverged solution

4.3.2.2. Bubble Pressure Model Study

Table 4.2 shows that when the BP model is implemented in CFDLib using the Schiller-Naumann drag coefficient model, the 60 × 600 cell solution still diverges. Table 4.2

further shows that the only means by which a stable time-dependent solution is possible with the 60×600 cell domain is by using CFDLib, while employing both the BP and BIT models, as recommended by Monahan et al. ([4], [27]). This study confirms that the BP and BIT models provide numerical stability to the numerical predictions of gas-liquid bubble columns under low superficial gas velocity flows. Hence, the remaining figures show simulations with both the BP and BIT models employed in CFDLib. Figure 4.10 compares experimental results of Mudde et al. [14] with the predictions of the time-averaged axial liquid velocity using CFDLib with the Schiller-Naumann drag coefficient model for axial locations of H = 0.30 m and 0.75 m above the distributor plate. Simulations for the 30×300 and 60×600 grids are shown. The simulations for both grids compare well with the experiments at H = 0.30 m (Figure 4.10a), but more variation between the simulations and experiments is observed at the center of column when H = 0.75 m (Figure 4.10b). The discrepancy is due to experimental error as reported by Mudde et al. [14] and was also observed in the work by Rafique and Duduković [13].
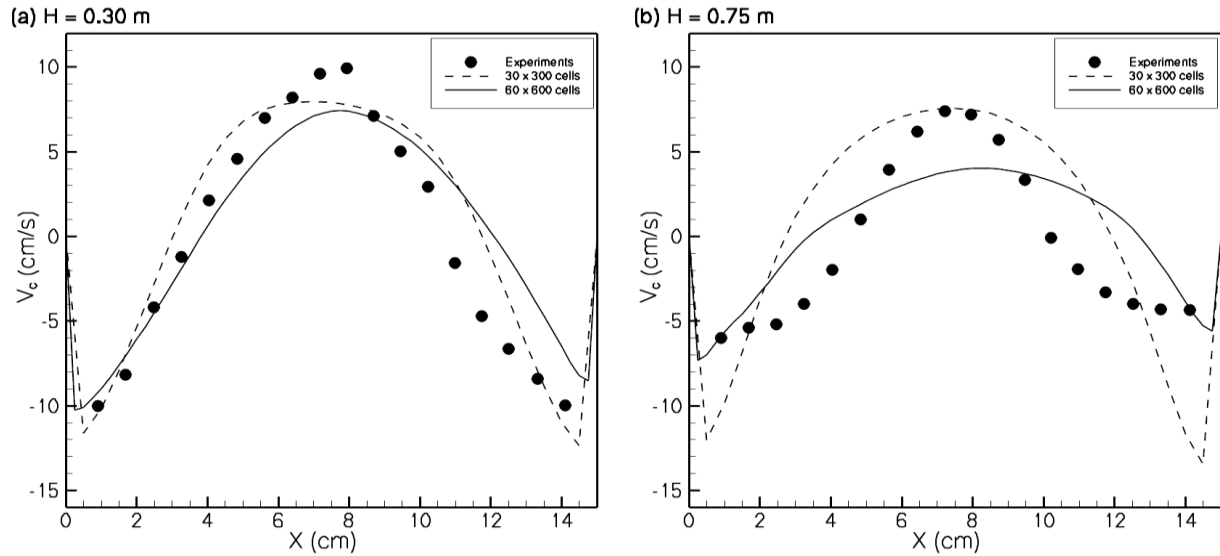
Figure 4.10. Time-averaged axial liquid velocity versus horizontal position, comparing CFDLib simulations using the Schiller-Naumann drag coefficient model with the BP and BIT models for different grid resolutions to experimental data by Mudde et al. [14] at heights of (a) H = 0.30 m and (b) H = 0.75 m.

Predictions of the gas holdup profile using CFDLib with the Schiller-Naumann drag coefficient model and the BP and BIT models are shown in Figure 4.11. Unfortunately, Mudde et al. [14] did not present experimental gas holdup data and thus, comparisons cannot be made. Although the gas holdup plots in the magnified scale of Figure 4.11 (e.g., relative to Figure 4.8) show two maxima, the variation in gas holdup is on the order of 1%. Hence α_d can be approximated as uniform, indicating that the flow field is extremely homogeneous at this low superficial gas velocity. It should be noted that the homogeneous behavior is only produced when both the bubble pressure and bubble induced turbulence models are used. The uniform gas holdup profile at low superficial gas velocity is consistent with observations in the literature [2].
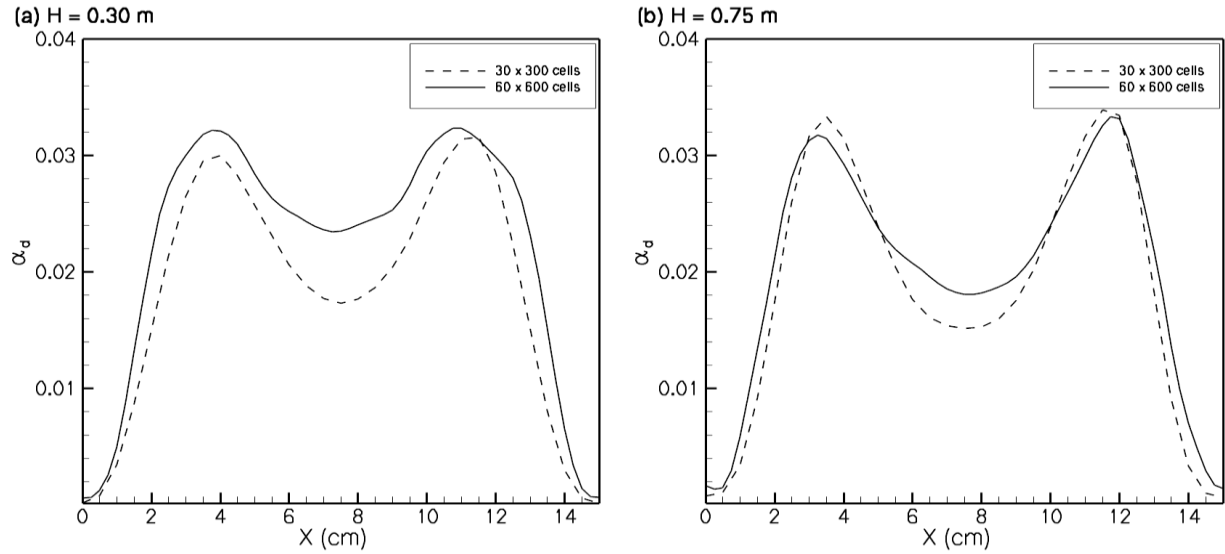
Figure 4.11. Time-averaged gas holdup versus horizontal position, comparing CFDLib simulations using the Schiller-Naumann drag coefficient model with the BP and BIT models for different grid resolutions at heights of (a) H = 0.30 m and (b) H = 0.75 m.

4.3.2.3. Drag coefficient model study

The White drag coefficient model is implemented in CFDLib to study the effect of the model on the numerical predictions. Different grid resolutions with or without the BP and BIT models are simulated. Table 4.2 shows that for the coarse and medium grid resolutions, where the cell size is larger than the effective bubble diameter (0.5 cm), the simulations converge using the White drag coefficient model with or without the BP model. However, neither simulation with or without the BP model is able to predict a converged solution for 60×600 cells. A stable time-dependent solution is possible using CFDLib with the White drag coefficient model and both the BP and BIT models. Figure 4.12 compares the experimental axial liquid velocity data of Mudde et al. [14] to the CFDLib simulations using the Schiller-Naumann and White drag coefficient models with 60×600 grid cells and the BP and BIT models. The White model matches the experimental data better than the Schiller-

58
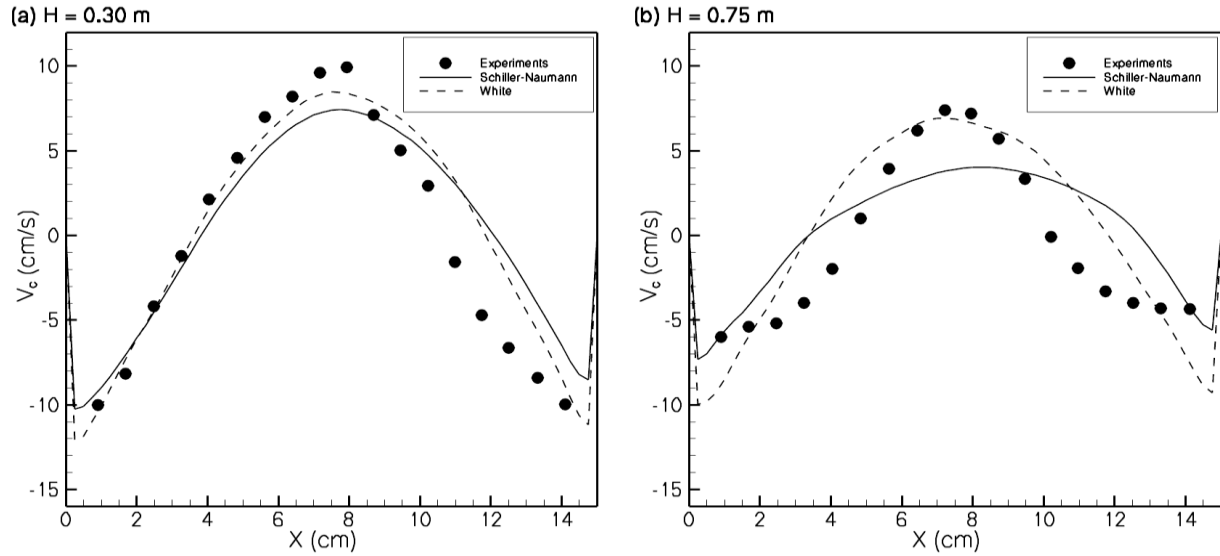
Figure 4.12. Time-averaged axial liquid velocity versus horizontal position, comparing CFDLib simulations using the Schiller-Naumann and White drag coefficient models for 60 × 600 grid cells with the BP and BIT models to experimental data by Mudde et al. [14] at heights of (a) H = 0.30 m and (b) H = 0.75 m.

Naumann model at both axial heights. The better prediction by the White model can be attributed to the drag coefficient being a function of bubble Reynolds number instead of a constant value when the bubble Reynolds number exceeds 1000; this is the case when the Schiller-Naumann model is used (Eq. (16)). Time-averaged gas holdup distributions are more homogeneous across the bubble column, especially towards the centerline and closer to the walls, when the White model is used as shown in Figure 4.13. The larger homogeneous gas holdup region predicted by the White model can be associated with the higher axial liquid velocity predictions (Figure 4.12) as compared to the Schiller-Naumann drag coefficient model. Thus, the White drag coefficient model is better suited for low gas velocity flows where the bubble Reynolds number may moderately exceed a value of 1000.
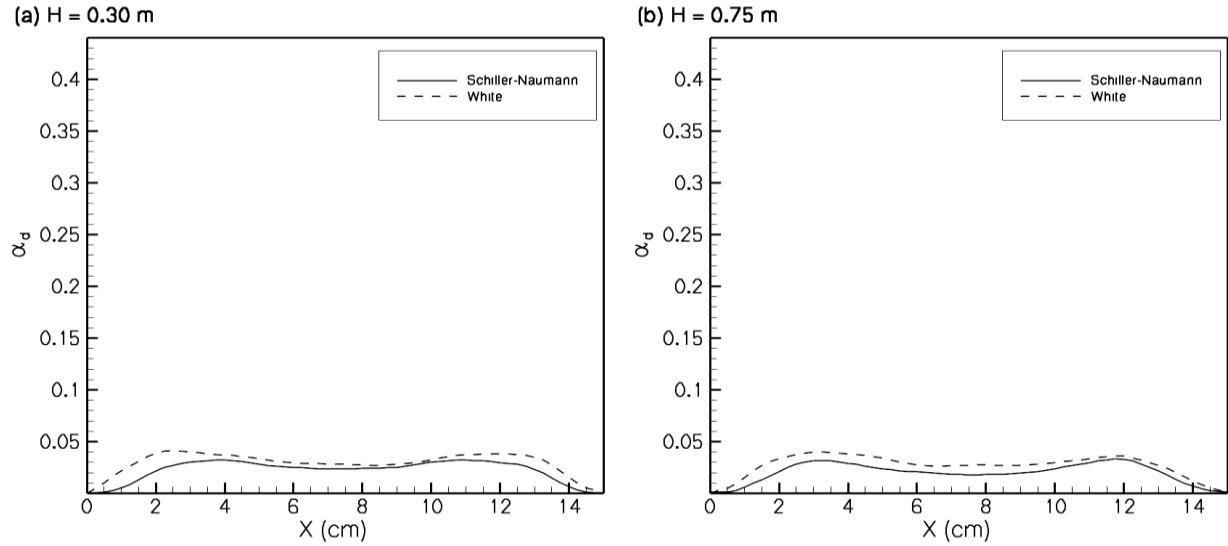
Figure 4.13. Time-averaged gas holdup versus horizontal position, comparing CFDLib simulations using the Schiller-Naumann and White drag coefficient models for 60 × 600 grid cells with the BP and BIT models at heights of (a) H = 0.30 m and (b) H = 0.75 m. Note that the scale is 10 times smaller than previous plots of gas holdup.

4.4. Numerical Stability

The section of results and discussion presented the diverged simulations as the mesh spacing became much smaller than bubble diameter size for the high and low superficial gas velocity cases. Two-phase flow equations with single pressure model are known for their ill-posedness because they have complex characteristics values [28]. Well-posedness of the two-phase flow equations is defined as the systems of equations are stable in the sense of von Neumann. Kashiwa and Rauenzahn [29] reported that ill-posed initial-value problem of two-phase flow equations with single-pressure model can be resolved by the use of a properly hyperbolic operator as a means of removing destabilizing truncation error due to forward-time differencing of the state in order to deliver well-behaved numerical problem. Stewart [30 , 31] stated that nonetheless two-fluid equations' ill-posedness, they can be solved numerically without non-convergence and give well-behaved results if interfacial drag is present and mesh spacing is not unreasonably fine, which further substantiates the findings in

60

the present study that the simulations diverge and results are not well-behaved at fine mesh spacing. However, the present work shows that the addition of the BP and BIT models into the two-phase flow equations for the low superficial gas velocity case provides a stable time-dependent solution at fine mesh spacing.

4.5. Conclusions

The gas-liquid flow dynamics in a bubble column were simulated using CFDLib in a two- dimensional Cartesian coordinate system with different grid resolutions to test the effect of using a bubble pressure model and two different drag coefficient models. Simulations at two axial heights above the inlet were compared to the experimental measurements of Rampure et al. [11] and Mudde et al. [14] for high and low superficial gas velocities, respectively. From previous FLUENT simulations [12], finer grid resolutions were not possible if the cell size was smaller than the bubble diameter for the high superficial gas velocity case. On the other hand, the CFDLib simulations produced grid-independent solutions at finer grid resolutions but still failed at a grid resolution of 80×800 cells. Overall, the CFDLib solutions were more physical compared with the FLUENT simulations. The White drag coefficient model predicted homogeneous gas holdup across the bubble column without using the bubble pressure model. The Schiller-Naumann model predicted off-center regions of high gas holdup at lower axial liquid heights. The Schiller-Naumann and White models compared qualitatively well with experiments at lower and higher axial liquid heights, respectively. For the low superficial gas velocity case, the higher grid resolution simulation converged when both the BP and BIT models were used in CFDLib. The BP and BIT models provide numerical stability to the simulation, so that cell sizes smaller than the effective bubble diameter can be used. The gas holdup profile was shown to

be uniform for the low superficial gas velocity, as expected. The White drag coefficient model predicted the time-averaged axial liquid velocity qualitatively better than the Schiller-Naumann model.

In summary, the CFDLib simulations provided physical and grid-independent predictions with the experiments as the grid resolution became finer. It was shown that the BP model did not affect the flow field predictions for the high superficial gas velocity case. Furthermore, the drag coefficient models appear to be sensitive to column location, where the White model works better at low axial heights and the Schiller-Naumann model works better at high axial heights. Finally, for the low superficial gas velocity case, the BP model was needed to model the pressure field and the BIT model added numerical stability to the system. The drag model had minimal effect on the flow predictions for a homogeneous flow field.

Notation

a coefficient in turbulence model equation

$C_{1\varepsilon}, C_{2\varepsilon}, C_\mu$ turbulence model parameters

62

C_{BP}	virtual mass coefficient
C_{BT}	bubble induced turbulence constant
C_D	drag coefficient
d_b	bubble diameter (m)
E	turbulence energy exchange rate coefficient (g/cm^{3}s)
F_{vm}	virtual mass force
G_k	production of turbulent kinetic energy for phase k (m^2/s^3)
g	acceleration due to gravity (m/s^2)
H	height from gas distributor
H_c	initial liquid height
H_d	initial gas height
K_{kl}	interfacial momentum exchange term between phase k and l (kg/m^3)
k	turbulent kinetic energy per unit mass (m^2/s^2)
p	pressure (Pa)
u	velocity (m/s)
r	radial coordinate (m)
Re	Reynolds number
V_c	axial liquid velocity (m/s)
W	column width
x	horizontal coordinate (cm)

Greek Symbols

α_{dcp}	gas holdup at close packing
α	holdup

β	coefficient in turbulence model equation
ε	turbulent energy dissipation rate for continuous phase (m^2/s^3)
μ	molecular dynamic viscosity for continuous phase (Pa-s)
μ_t	turbulent dynamic viscosity for continuous phase (Pa-s)
ρ	density (kg/m^3)
$\sigma_k, \sigma_\varepsilon$	turbulent Schmidt number for k and ε, respectively
τ	effective stress (N/m^2)
τ_{kl}	time constant

Subscripts

c	continuous phase
d	dispersed phase
k	represents either continuous or dispersed phase
l	if k is continuous phase, then l is dispersed phase, and vice versa

References

[1] Sanyal, J., Vasquez, S., Roy, S., Duduković, M.P., 1999. Numerical simulation of gas-liquid dynamics in cylindrical bubble column reactors. Chemical Engineering Science, 54, 5071-5083.

[2] Joshi, J.B., 2001. Computational flow modeling and design of bubble column reactors. Chemical Engineering Science, 56(21-22), 5893-5933.

[3] Joshi, J.B., Vitankar, V.S., Kulkarni, A.A., Dhotre, M.T., Ekambara, K., 2002. Coherent flow structures in bubble column reactors. Chemical Engineering Science, 57(16), 3157-3183.

[4] Monahan, S.M., Vitankar, V.S., Fox, R.O., 2005. CFD predictions for flow-regime transitions in bubble columns. AIChE Journal, 51, 1897-1923.

[5] Pan, Y., Duduković, M.P., 2000. Numerical investigation of gas-driven flow in 2-D bubble columns. AIChE Journal, 46, 434-449.

[6] Sokolichin, A., Eigenberger, G., 1994. Gas-liquid flow in bubble columns and loop reactors: I. Detailed modeling and numerical simulation. Chemical Engineering Science, 49, 5735-5746.

[7] Delnoij, E., Lammers, F.A., Kuipers, J.A.M., van Swaaij, W.P.M., 1997a. Dynamic simulation of dispersed gas-liquid two-phase flow using a discrete bubble model. Chemical Engineering Science, 52(9), 1429-1458.

[8] Delnoij, E., Kuipers, J.A.M., van Swaaij, W.P.M., 1997b. Dynamic simulation of gas-liquid two-phase flow: Effect of column aspect ratio on the flow structure. Chemical Engineering Science, 52(21/22), 3759-3772.

[9] Delnoij, E., Kuipers, J.A.M., van Swaaij, W.P.M., 1997c. Computational fluid dynamics applied to gas-liquid contactors. Chemical Engineering Science, 52(21/22), 3623-3638.

[10] Lin, T-J., Reese, J., Hong, T., Fan, L.-S., 1996. Quantitative analysis and computation of two-dimensional bubble columns. AIChE Journal, 42, 301-318.

[11] Rampure, R.M., Buwa, V.V., Ranade, V.V., 2003. Modeling of gas-liquid/gas-liquid-solid flows in bubble columns: Experiments and CFD simulations. The Canadian Journal of Chemical Engineering, 81, 692-706.

[12] Law, D., Battaglia, F., and Heindel, T.J., 2006. Numerical simulations of gas-liquid flow dynamics in bubble columns. Proceedings of the ASME Fluids Engineering Division, IMECE2006-13544, Chicago, IL.

[13] Rafique, M., Duduković, M.P., 2006. Influence of different closures on the hydrodynamics of bubble column flows. Chemical Engineering Communications, 193, 1–23.

[14] Mudde, R.F., Lee, D.J., Reese, J., Fan, L.-S., 1997. Role of coherent structures on Reynolds stresses in a 2-D bubble column. AIChE Journal, 43, 913-926.

[15] Hirt, C.W., Amsden, A.A., Cook, J.L., 1974. An arbitrary Lagrangian-Eulerian computing method for all flow speeds. Journal of Computational Physics, 14, 227-253.

[16] Kashiwa, B.A., VanderHeyden, W.B., 2000. Toward a general theory for multiphase turbulence. LA-13773-MS Report

[17] Launder, B.E., Spalding, D.B., 1974. The numerical computation of turbulent flows. Computer Methods in Applied Mechanical Engineering, 3, 269-289.

[18] Lance, M., Bataille, J., 1991. Turbulence in the liquid phase of a uniform bubbly air-water flow. Journal of Fluid Mechanics, 222, 95-118.

[19] Mizukami, M., Parthasarathy, R.N., Faeth, G.M., 1992. Particle-generated turbulence in homogeneous dilute dispersed flows. International Journal of Multiphase Flow, 18, 397-412.

[20] Parthasarathy, R.N., Faeth, G.M., 1990a. Turbulence modulation in homogeneous dilute particle-lade flows. Journal of Fluid Mechanics, 220, 485-514.

[21] Parthasarathy, R.N., Faeth, G.M., 1990b. Turbulent dispersion of particles in self-generated homogenous turbulence. Journal of Fluid Mechanics, 220, 515-537.

[22] Schiller, L., Naumann, A., 1933. Uber die grundlegenden berechnungen bei der schwerkraftaufbereitung. Zeitung des vereins deutscher ingenieure, 77- 318.

[23] White, F.M., Viscous fluid flow, McGraw-Hill, New York, 1974.

[24] Spelt, P.D.M., Sangani, A., 1998. Properties and averaged equations for flows of bubbly liquids. Applied Science Reserve, 58, 337-386.

[25] Biesheuvel, A., Gorissen, W.C.M., 1990. Void fraction disturbances in a uniform bubbly fluid. International Journal of Multiphase Flow, 16, 211-231.

[26] Sato, Y., Sadatomi, M., Sekoguchi, K., 1981. Momentum and heat transfer in two-phase bubble flow I. International Journal of Multiphase Flow, **7**, 167-177.

[27] Monahan, S.M., Fox, R.O., 2007. Linear stability analysis of a two-fluid model for air-water bubble columns. Chemical Engineering Science, 62, 3159-3177.

[28] Ransom, V.H., Hicks, D.L., 1984. Hyperbolic two-pressure models for two-phase flow, Journal of Computational Physics, 53, 124-151.

[29] Kashiwa, B.A., VanderHeyden, W.B., 2000. Toward a general theory for multiphase turbulence. LA-13773-MS Report.

[30] Stewart, H.B., 1979. Stability of two-phase flow calculation using two-fluid models, Journal of Computational Physics, 33, 259-770.

[31] Stewart, H.B., 1981. Fractional step methods for thermohydraulic calculation, Journal of Computational Physics, 40, 77-90.

CHAPTER 5. VALIDATING GAS-LIQUID FLOW SIMULATIONS IN AN EXTERNAL LOOP AIRLIFT REACTOR

A paper will be submitted to the Journal of Fluids Engineering.

Deify Law[1], Samuel T. Jones[2], Theodore J. Heindel[2], and Francine Battaglia[1]
Department of Mechanical Engineering
[1]Virginia Polytechnic Institute and State University, Blacksburg, VA 24061
[2]Iowa State University, Ames, IA 50011

Abstract

The external loop airlift reactor (ELALR) is a modified bubble column reactor that is composed of two vertical columns that are interconnected with two horizontal connectors, and are often preferred over traditional bubble column reactors because they can operate over a wider range of conditions. In the present work, the gas-liquid flow dynamics in an ELALR are simulated using CFDLib with an Eulerian-Eulerian ensemble-averaging method in two-dimensional (2D) and three-dimensional (3D) coordinate systems. In addition, models are employed for the interphase momentum transfer and turbulence behavior. The CFD simulations for temporal and spatial averaged riser gas holdup and riser superficial liquid velocity are compared to experimental measurements from a 10.2 cm diameter ELALR over a range of superficial gas velocities from 1.0 to 20 cm/s. The effect of specifying a mean bubble diameter size for the CFD modeling is examined. The objectives are to validate 2D and 3D simulations with the experimental data in order to determine how well the models predict the hydrodynamics in an external loop airlift reactor.

5.1. Introduction

Airlift reactors are widely used in many bioprocessing applications due to their excellent heat and mass transfer characteristics, simple construction, and ease of operation [1]. The airlift reactor is made of two sections interconnected at the top and bottom. One section (the riser) is gassed, while the other (the downcomer) is not. As a consequence of the density difference between the bubbly mixture in the riser and liquid in the downcomer, liquid circulation develops [2]. Two basic classifications of airlift reactors are the internal loop and external loop reactors. An internal loop reactor is a modified bubble column that has been subdivided into a riser and downcomer by the addition of a baffle or draught tube. The external loop airlift reactor (ELALR) is composed of a riser and downcomer that are joined together with two horizontal connectors (refer to Figure 5.1). Airlift reactors are preferred over traditional bubble column reactors due to well directed liquid circulation, thus facilitating the cultivation of shear sensitive organisms; as a result these reactors are widely used in the biochemical industry and for waste water treatment [3]. Airlift reactor hydrodynamics are studied experimentally and computationally for scale-up and design considerations. Full-scale experimentation in airlift reactors is expensive and therefore, a more cost-effective approach is by using validated computational fluid dynamics (CFD) models.

There have been extensive studies, performed experimentally [4, 5, 6, 7, 8, 9, 10, 11, 12] and computationally [3, 8, 13], that provide a better understanding of external loop airlift reactor hydrodynamics. Bentifraouine et al. [4] studied the effects of gas-liquid separator and liquid height on the global hydrodynamic parameters of an ELALR. The study revealed that two openings at the top junction between the riser and downcomer are able to generate doubling of the liquid circulation velocity and a 30% decrease in the gas holdup. Gavrilescu et al. [6]

observed that the cross-sectional area ratio of downcomer-to-riser affects the gas holdup due to the influence of the geometry ratio on liquid circulation velocity. Merchuk et al. [7] measured local gas holdup and liquid recirculation rate in an airlift reactor and determined relationships between the measured liquid velocity and the gas flow rate, and between the local gas velocity and the total flow rate of the mixture. Snape et al. [5] conducted experiments to study the effects of liquid phase properties and sparger design in an ELALR and found that the Zuber and Findlay drift flux model fit the riser gas holdup data for the heterogeneous flow regime but failed to predict gas holdup data for the transitional flow regime. Dhaouadi et al. [9] measured the solid effects on hydrodynamics and heat transfer in an ELALR and found that an increase of solid holdup leads to a decrease of liquid velocity and heat transfer. Other researchers such as Zhang et al. [10] and Choi et al. [12] measured the effects of different reactor configurations and operating conditions on the hydrodynamic parameters of an external loop airlift reactor.

For computational studies, two methods commonly used for bubble column predictions are the Eulerian-Eulerian model or the Eulerian-Lagrangian model. The Eulerian-Eulerian model treats dispersed (gas bubbles) and continuous (liquid) phases as interpenetrating continua, and describes the motion for gas and liquid phases in an Eulerian frame of reference [14, 15, 16, 17, 18]. In the Eulerian–Lagrangian model, the continuous phase is described in an Eulerian representation, while the dispersed phase is treated as discrete bubbles and each bubble is tracked by solving the equations of motion for individual bubbles [19, 20, 21]. The authors [22] have previously demonstrated that by using the Eulerian-Eulerian two-fluid model, predictions of gas holdup and gas velocity were in good agreement with experiments in the literature for bubble column flows, provided that appropriate turbulence models and grid resolutions were used.

Numerical simulations of external loop airlift reactors employing an Eulerian-Eulerian model [3, 8, 13] were surveyed and literature on Eulerian-Lagrangian simulations of airlift reactor hydrodynamics were not found. Wang et al. [8] conducted two-dimensional steady-state simulations of a cylindrical external loop airlift reactor using an Eulerian-Eulerian method and showed that the lateral forces and interphase turbulence have noticeable influence on predicting the hydrodynamic behavior. In addition, Cao et al. [13] performed three-dimensional transient simulations of a rectangular external loop airlift reactor and obtained good agreement between the predicted hydrodynamic parameters and experiments, except in a high gas flow rate regime. Roy et al. [3] conducted three-dimensional steady-state simulations of a cylindrical ELALR and found agreement between the CFD Eulerian-Eulerian predictions for gas holdup, axial liquid velocity, and mixing time with experiments. It should be noted that Wang et al. [8] and Cao et al. [13] conducted experiments in addition to numerical simulations.

In the present work, the gas-liquid flow dynamics in an ELALR are simulated using CFDLib in two- and three-dimensions. The Schiller-Naumann drag coefficient model is used and the turbulence model employed is either the bubble-pressure model with bubble induced turbulence (BP+BIT) or the multiphase k-ε model. An appropriate effective bubble diameter size is determined based on the superficial gas velocity in a parametric study for both 2D and 3D simulations. Temporal and spatial averaged gas holdup over a region in the riser and downcomer are computed and compared to experimental measurements for an ELALR of the same geometry. The objectives are to validate the CFD simulations with experimental data in order to determine an appropriate set of model parameters for future design analyses.

5.2. Experimental Procedures

A schematic representation of the ELALR used in this study is shown in Figure 5.1. The ELALR consists of two main parts, a 2.4 m cast acrylic riser with a 10.2 cm inner diameter (ID) and a 2.4 m cast acrylic downcomer with a 2.5 cm ID. The downcomer and riser sections are connected with two 13.3 cm long acrylic tubes with 2.5 cm ID and located at $H = 5$ and 127 cm, where H is the reactor height above the aeration plate. The initial unaerated liquid height is set in all experiments to $H = 142.2$ cm (14 riser diameters). Gas is injected at the riser base through a stainless steel distributor plate having 1 mm diameter holes that are uniformly distributed over the entire plate area to produce an open area ratio of 2.22%. A gas plenum is located beneath the aeration plate and filled with large glass beads (i.e., marbles) to promote uniform gas distribution into the riser.

The top of the riser and downcomer sections are joined together with a ball valve (valve B in Figure 5.1) as they enter the column vent; this allows for the possibility of gas flow out of the downcomer. A gate valve (valve A in Figure 5.1) is installed in the middle of the downcomer section so that when closed, the ELALR approximates a semi-batch bubble column. Hence, three downcomer configurations are possible and referenced in this study: both the downcomer gate valve and vent are closed (BC mode for bubble column), the gate valve is open and the vent is closed (CV mode for closed vent), and both the gate valve and vent are open (OV mode for open vent).

Two mass flow meters are used to measure the gas flow rate to cover low and high gas flow rate ranges, where the gas is filtered compressed air. Two pressure transducers are installed in the riser and located at $H = 10.2$ and 110.5 cm. An inclined U-tube manometer is attached to the downcomer section with connections located at $H = 5$ and 67.13 cm. The mass flow meters

and pressure transducers are interfaced to a computer-controlled data acquisition system. Average inlet gas flow rate and riser section pressures are computed from measurements taken over a 2 second interval at a frequency of 1000 Hz.

Gas holdup in the riser section (α_R) is measured between the two pressure transducers and is determined from the reactor pressure drop assuming that acceleration effects are negligible [1]. Thus the total pressure drop in the reactor corresponds to the hydrostatic head; in this case,

$$\alpha_R = 1 - \frac{\Delta P}{\Delta P_o} \tag{1}$$

where α_R is the dispersed phase (gas) volumetric fraction, ΔP is the difference between the average local pressure at the two pressure transducers when $U_g > 0$, and ΔP_o is the corresponding average pressure difference when $U_g = 0$ (i.e., the liquid hydrostatic head).

Gas holdup in the downcomer section (α_D) is measured using an inclined U-tube manometer, and is determined by the change in height of the water columns in the manometer, assuming acceleration effects to be negligible. Additional experimental details can be found elsewhere [23, 24].

Measurement uncertainties are estimated following the method provided by Figliola and Beasley [25]. The typical uncertainties associated with U_g are ± 1 to 5%, with the larger uncertainties corresponding to the lowest velocity measurements. The corresponding absolute gas holdup uncertainty is estimated to be approximately ± 0.001–0.015.

5.3. Numerical Formulation

Refer to Chapter 3 for the governing equations and closure models.

5.4. Simulation Conditions

Simulations are performed using a fixed grid and the computational domain is selected to match the experimental conditions. Referring to Figure 5.1, the geometry is modeled from $H = 0$ (just above the aeration plate) to the bottom of vent B. The computational inlet condition assumes a uniform inlet velocity U_g to approximate the experimental condition of a large number of uniformly distributed holes.

No-slip and outflow conditions are applied at the walls and top of the column, respectively. If the vent is closed, the no-slip condition is applied, otherwise the outflow condition is used at the outlet of the open vent airlift reactor. An effective bubble size d_b, depending on the superficial gas velocity, is used to represent the dispersed gas phase. The Schiller-Naumann drag coefficient model is used, which was determined based on the study in Chapter 4. The convergence criteria are set to 1×10^{-8} for changes in the residuals of every dependent variable. All the simulations use an adaptive time step to march the solution forward; the flow achieves a pseudo-steady state after 20 s. The time-averaging process includes results from 20 s to 90 s for a total of 7000 realizations. All the hydrodynamic predictions such as average gas holdup and average riser superficial liquid velocity are spatially averaged from 10 to 110 cm above the plate. The simulations are performed at 1, 5, 10, 15, and 20 cm/s superficial gas velocities. The central processing unit (CPU) time information is also tabulated in Table 5.1 for 2D and 3D simulations of a bubble column reactor from 5 to 10 seconds of simulation time. The 3D simulations require twice as much computational time than the 2D simulation. It is also noted that the 3D time step is less than the 2D time step.

Table 5.1 CPU information for 2D and 3D simulations of a bubble column reactor

	2D	3D
CPU (s)	2397	36946
Number of cells	2772	13332
Time step (s)	0.004	0.002
Number of time step	1351	9330
CPU per time step per cell	0.00064	0.0003
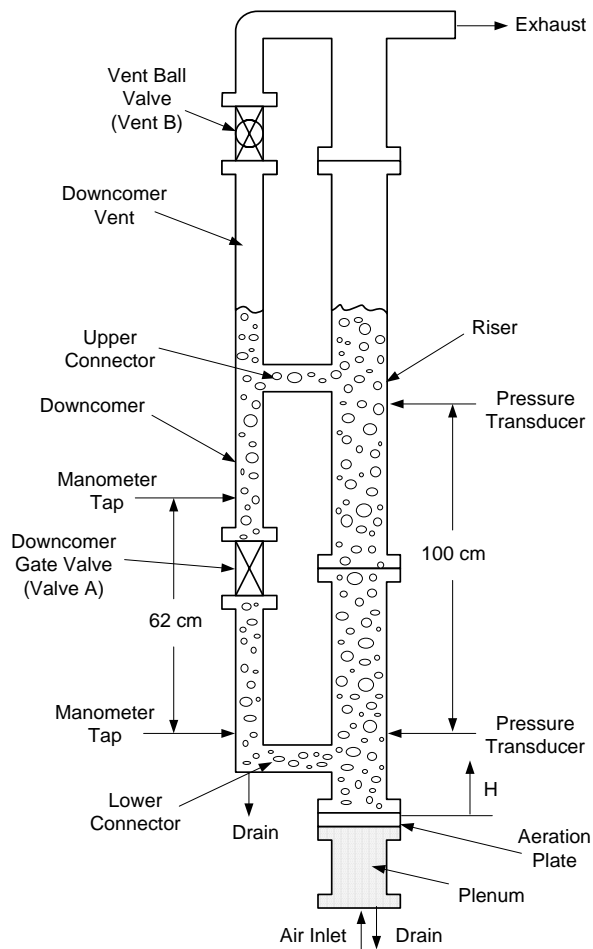
Figure 5.1. Geometrical model of air-water external loop airlift reactor [24].

5.5. Results and Discussions

5.5.1. Bubble Column (BC) Study

The BC mode simulations are conducted for the riser column only; as mentioned, the external loop airlift reactor approximates a semi-batch bubble column when both valve A and vent B are closed. For the BC study, the computational models are tested to determine the effects of selecting an effective bubble diameter, turbulence models, and 2D versus 3D domains. The 2D and 3D computational domains are simulated using a Cartesian coordinate system, where the 2D domain represents the center plane of the riser. An extensive grid resolution study of bubble column flow simulations was previously performed by Law et al. [22]. Herein, the 2D simulations use 13333 single-block structured cells with $\Delta x = 0.408$ cm and $\Delta z = 0.45$ cm, whereas the 3D grid uses 48000 multi-block structured cells with cell size variations of $\Delta x = 0.40–0.50$ cm, $\Delta y = 0.40–0.50$ cm, and $\Delta z = 0.8$ cm. The grid edges Δx and Δy lay in horizontal planes and Δz is in the vertical direction.
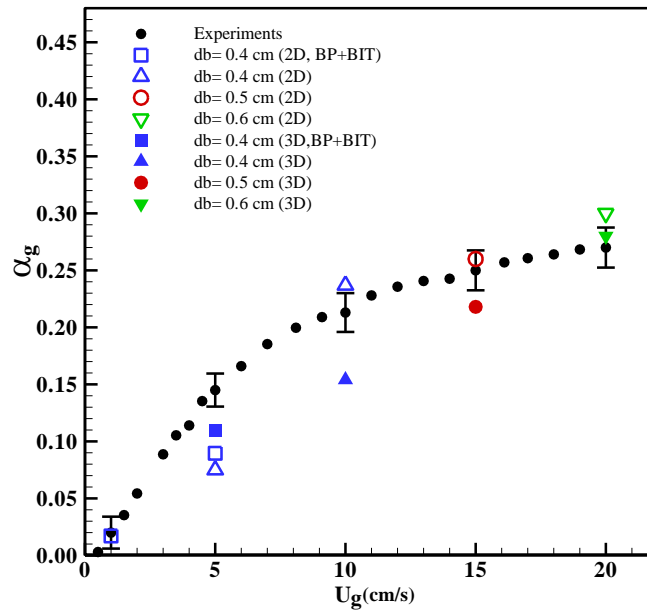
Figure 5.2. Comparison of average gas holdup simulations with experiments for the BC mode at different superficial gas velocities. Unless specified otherwise, the k-ε turbulence model is used.

Figure 5.2 compares the average gas holdup for the 2D and 3D simulations with the experiments. The error bars in this figure represent the maximum uncertainty in the gas holdup measurements and are only shown for cases associated with the CFD calculations, although they are applicable at all experimental data points. It should be noted that the error bars represent the maximum uncertainty in the measured gas holdup, but in most cases, this uncertainty encompasses a smaller range. The selection of the effective bubble diameter size is guided by experimental observations, which were between 0.4 and 0.5 cm [24], depending on the superficial gas velocity. As a starting point, the effective bubble diameter used in the 2D simulations is 0.4 cm for $U_g = 1$, 5, and 10 cm/s; $d_b = 0.5$ cm for $U_g = 15$ cm/s; and $d_b = 0.6$ cm for $U_g = 20$ cm/s. As will be shown, the reason for using larger effective bubble diameters with increasing superficial gas velocity is that for a fixed inlet velocity, the overall gas holdup decreases with increasing bubble size. Furthermore, the superficial gas velocity guides which turbulence model is appropriate; the simulations shown in Figure 5.2 employ the multiphase k-ε model unless otherwise specified. Figure 5.2 shows that the simulations predict the experiment well at $U_g = 1$ cm/s using the BP+BIT model, which is expected for a homogeneous flow [22]. Overall, the 2D predictions agree well with the experiments except at $U_g = 5$ cm/s, which is considered a transitional flow regime [26]. Both turbulence models, the BP+BIT model and the multiphase k-ε model, were tested at 5 cm/s superficial gas velocity. The BP+BIT model predicts a slightly larger gas holdup as compared to the multiphase k-ε model, but neither 2D case compares well with the experiments. Also, the effective bubble diameter used for $U_g = 20$ cm/s is larger than that observed in the experiments. These potentially erroneous results

motivate performing simulations using a 3D domain to determine how the turbulence models and effective bubble diameter affect the predictions.

The parametric study for the 3D simulations begins with addressing the poor predictions using the 2D domain for $U_g = 5$ cm/s. Testing both the BP+BIT model and the k-ε model, it was found that the 3D simulation using the BP+BIT compares quantitatively well with the experimental data, as shown in Figure 5.2. However, the simulation employing the k-ε model failed to produce a stable solution, which suggests that the 5 cm/s transitional flow is very sensitive to the computational model. Four additional cases were simulated using the 3D modeling. For $U_g = 10$ cm/s, the 3D simulation underpredicts the experimental gas holdup. At $U_g = 15$ cm/s, the 3D simulation slightly underpredicts the experiment using $d_b = 0.5$ cm. Finally, the 3D simulation for $U_g = 20$ cm/s slightly overpredicts the measured gas holdup using an effective bubble diameter of 0.6 cm as compared to the 2D simulation. The last two findings further substantiate that using an effective bubble diameter within the experimental observations is important.
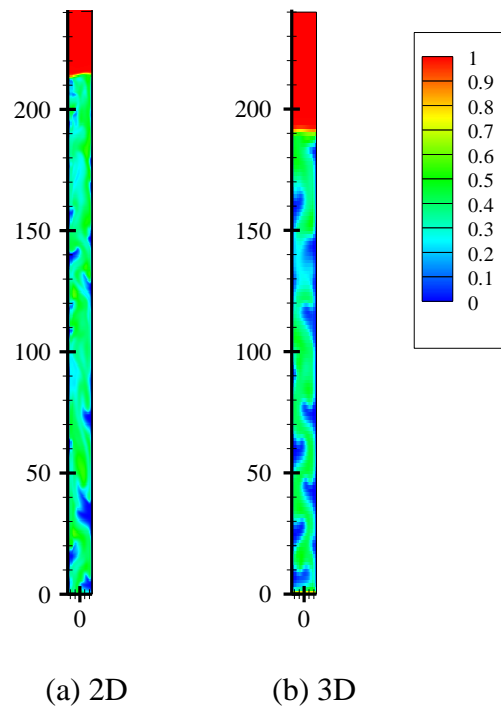
Figure 5.3. **Instantaneous gas holdup contours for the BC mode at U_g = 15 cm/s comparing (a) 2D and (b) 3D simulations.**

Figure 5.3 shows the comparison of the instantaneous gas holdup at U_g = 15 cm/s for the 2D and 3D simulations. It is obvious that the bubbles tend to spiral upwards in the 3D model of the riser, which has also been observed experimentally [27], whereas the 2D model constricts the flow to a single plane, causing bubbles to rise more vertically. Figure 5.4 shows the average gas holdup profiles for the 2D and 3D simulations at 3 vertical locations in the riser above the aeration plate. The 2D prediction shows a more uniform gas holdup across the riser column, which resembles gas holdup trends for a homogeneous flow. In contrast, the 3D gas holdup profiles are more parabolic, which is expected for this heterogeneous flow regime. In addition, the gas holdup profiles converge with increasing height for both the 2D and 3D simulations because the gas-liquid flow becomes fully developed. The parabolic gas holdup profiles

predicted by the 3D simulation for the BC mode are also consistent with experimental observations by Joshi [28].
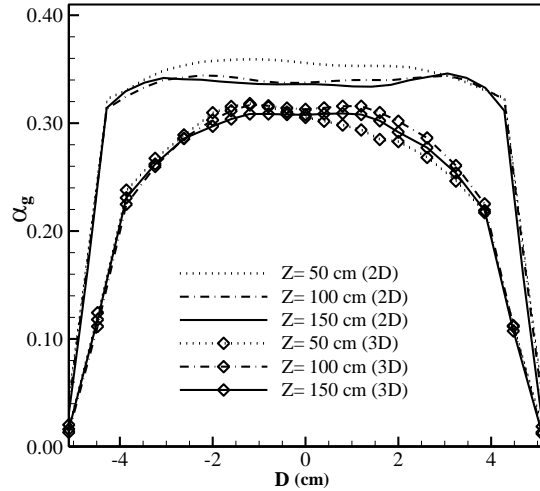
Figure 5.4. Average gas holdup profiles for the BC mode at U_g = 15 cm/s comparing 2D and 3D simulations at different heights above the aeration plate.

5.5.2. Comparison of Different ELALR Configuration Modes

A comparison of the three ELALR modes is investigated. The simulations are conducted at U_g = 10 cm/s in a 2D Cartesian coordinate system. The intention is to understand the flow dynamics within the reactor operating with different downcomer configurations. Figure 5.5(a-c) presents instantaneous gas holdup for the BC, CV, and OV configuration modes, respectively. The instantaneous gas holdup exhibits an axial oscillation in the liquid bed for all modes. The BC instantaneous gas holdup is similar to that of the riser column of CV mode. Note that the oscillations observed in the axial direction translate to horizontal oscillations if the vertical location is fixed and a time series is recorded. For both the CV and OV modes, a large gas bubble region is observed in the downcomer in the vicinity of the horizontal connector at H = 127 cm. The CV mode, in which vent B is closed, causes a gas-rich pocket in the upper connector and thus, a higher riser height (approximately to H = 190 cm). The OV mode, in which

both the valve and vent are open, allows for bubble formation and circulation within the downcomer and thus lowers the riser height.

(a) BC   (b) CV   (C) OV
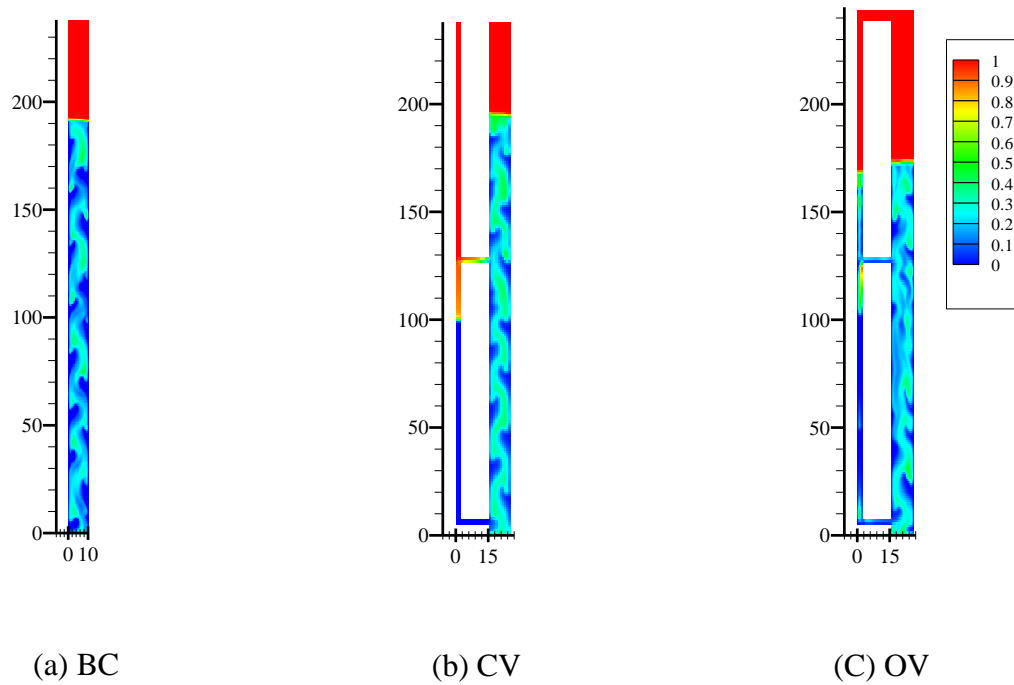
Figure 5.5.   Instantaneous gas holdup contours at U_g = 10 cm/s comparing (a) BC, (b) CV, and (c) OV modes of operation.

| (a) experiment | (b) schematic | (c) simulation |
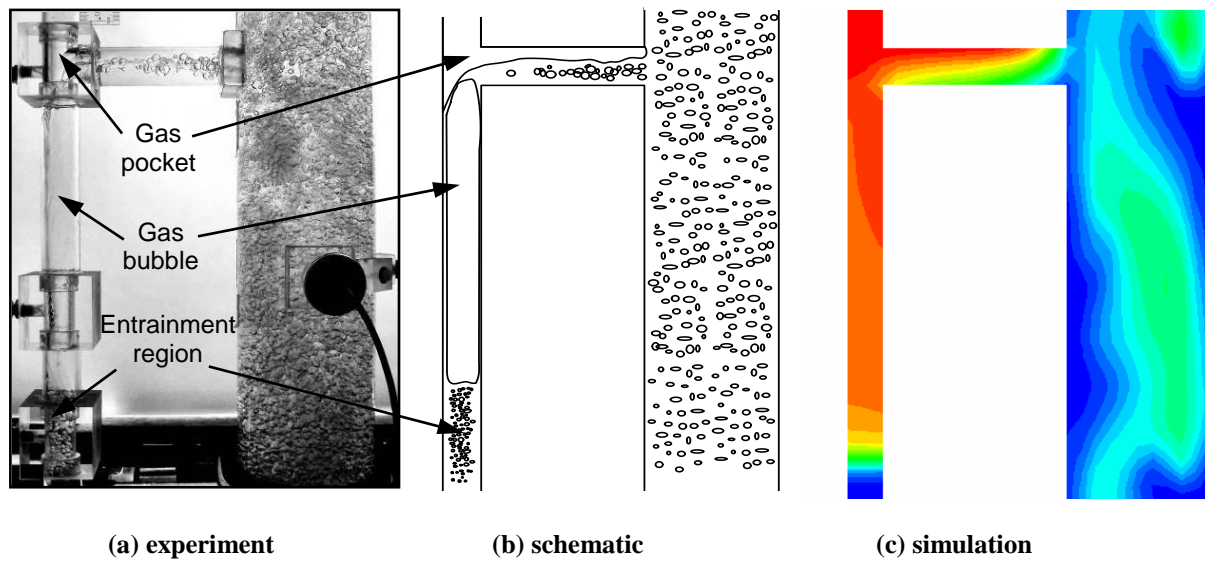
Figure 5.6.   **Instantaneous gas holdup for the CV mode at U_g = 10 cm/s superficial gas velocity comparing the gas-rich regimes for the (a) experiment, (b) schematic and (c) simulation.**

As shown in Figure 5.6 and Figure 5.7 for the CV and OV modes, respectively, similar gas bubble formations near the upper connection of the downcomer are observed experimentally and qualitatively compare well with the CFD predictions of gas holdup. The experiments and simulations show that a meandering bubble plume flows through the riser column in the CV and OV modes. In the CV mode (Figure 5.6), when the vent is closed, a large gas bubble forms in the downcomer near the upper connector and restricts liquid from traveling through the connector and rising through the downcomer. Comparing Figure 5.6 and Figure 5.7, the gas bubble significantly reduces near the connector when the vent is open (OV mode). Furthermore, the OV mode induces better mixing whereby liquid moves through the upper connector and expands through the downcomer. It is particularly encouraging that the 2D simulations qualitatively compare very well with the experiments in Figure 5.6 and Figure 5.7 because the hydrodynamics are very complex.
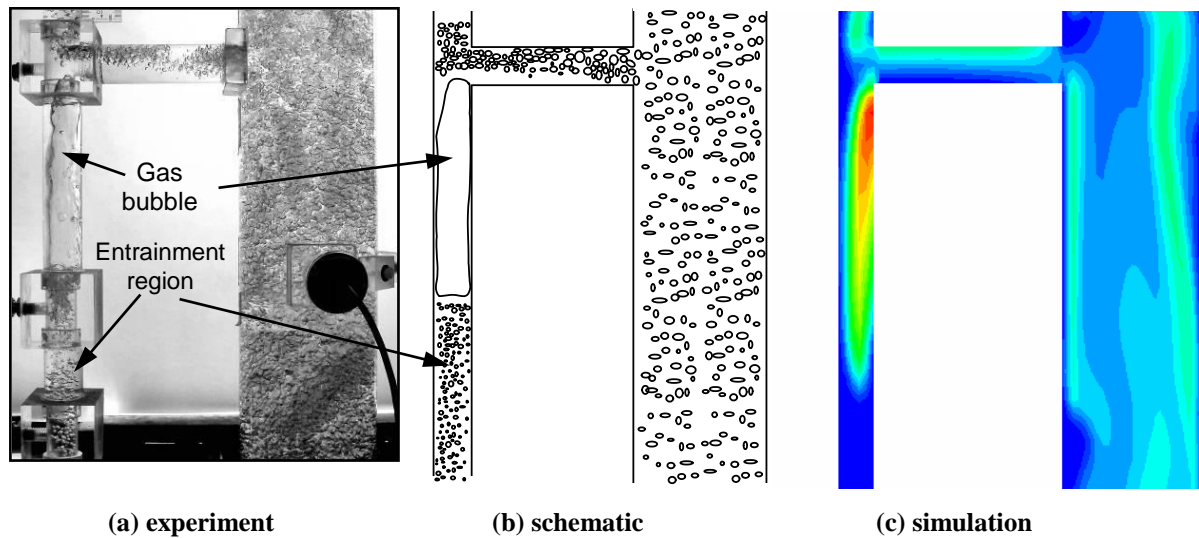
Figure 5.7. Instantaneous gas holdup for the OV mode at U_g = 10 cm/s superficial gas velocity comparing the gas-rich regimes for the (a) experiment, (b) schematic and (c) simulation.

5.5.3. External Loop Airlift Reactor Study for OV Mode

The 2D and 3D computational domains are simulated to compare with experiments of the external loop airlift reactor. The 2D simulation used 7574 block structured cells with Δx = 0.408–0.50 cm and Δz = 0.90–1.25 cm whereas the 3D simulation used cells with Δx = 0.408–0.50 cm, Δy = 0.408–0.50 cm, and Δz = 1.0 cm. The 3D simulation runs on 74-block structured grid shown in Figure 5.8. A FORTRAN code was written to generate the block of structured grids in the plot3d format. The inter-block communication is processed by the code written by Padial et al. [29] for CFDLib. The connectors and downcomer are approximated as rectangular tubes (Figure 5.8 (a)) with a square cross-sectional area 2.215 cm × 2.215 cm that conserves the cross-sectional area of the corresponding 2.5 cm diameter circular geometry of the experiments (refer to Figure 5.1). Figure 5.8 (b) shows the grid for the full three-dimensional domain.

(a) X-Y cross-section   (b) Three-dimensional
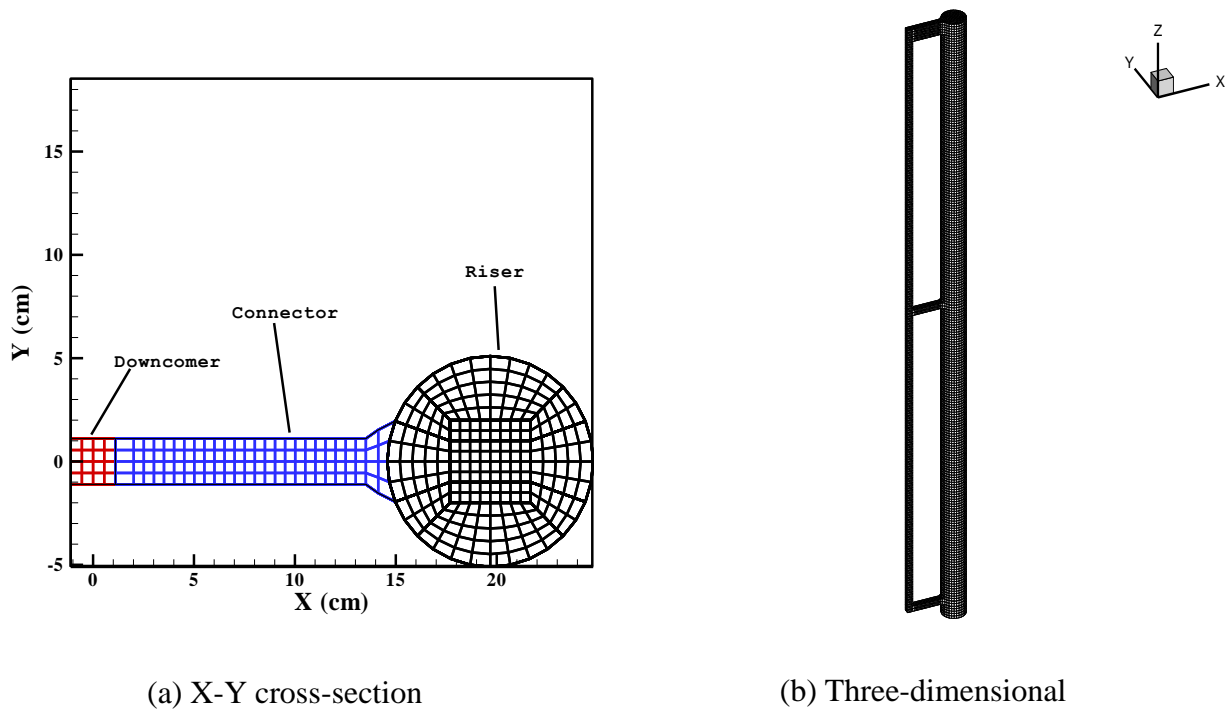
Figure 5.8. Views of the grid resolution for a (a) X-Y cross-section and (b) the three-dimensional domain of the external loop airlift reactor used for the simulations.

Figure 5.9 compares average gas holdup for the 2D and 3D simulations with the experiments at various superficial gas velocities for the riser and downcomer. The bubble diameter was chosen for each inlet gas velocity based on the results shown in Figure 5.2. Predictions are in good agreement with both the riser and downcomer experiments except the 3D simulation at U_g= 10 cm/s, which is a transitional flow regime whereby the computational models do not perform well (see section 4.3.2). The BP+BIT model is employed at U_g= 1 and 5 cm/s whereas the multiphase k-ε model was employed at higher superficial gas velocities. Figure 5.10 compares 2D and 3D average superficial riser liquid velocity simulations with the experiments. The 3D simulations compare quantitatively better with the experiments than the

2D simulations for all inlet gas velocities. These results elucidate the importance for using 3D simulations for a complex reactor geometry.

(a) 2D simulation   (b) 3D simulation
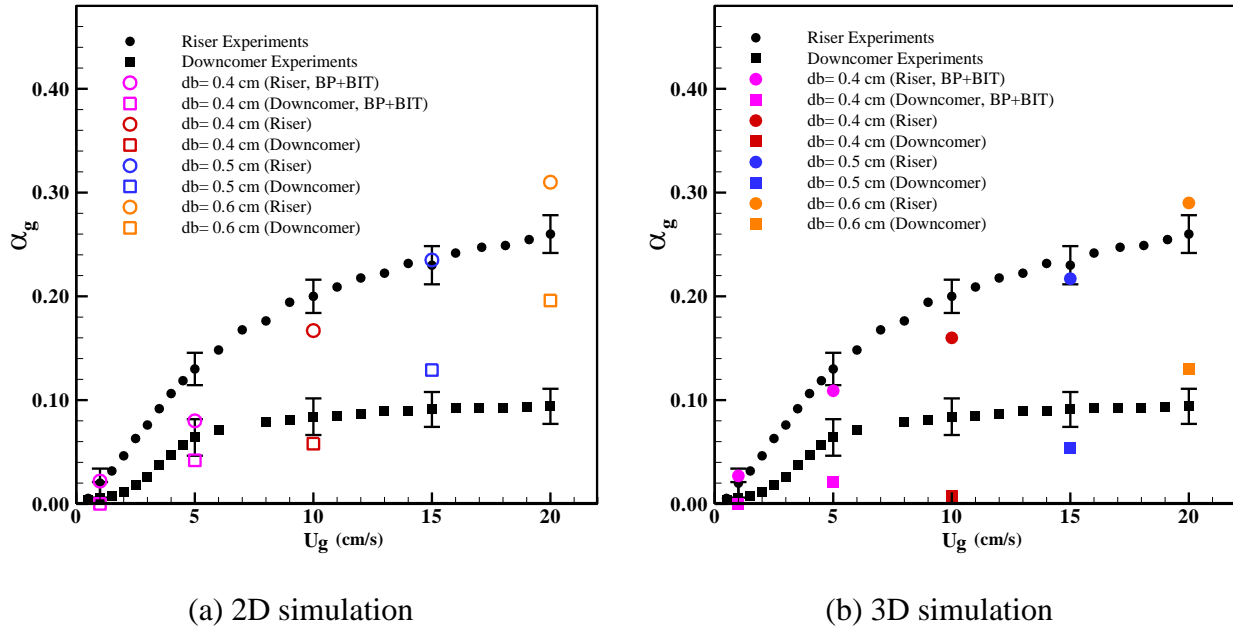
Figure 5.9. Comparison of (a) 2D and (b) 3D average gas holdup simulations with experiments for the external loop airlift reactor at different superficial gas velocities. Unless specified otherwise, the k-ε turbulence model is used.

(a) 2D simulation   (b) 3D simulation
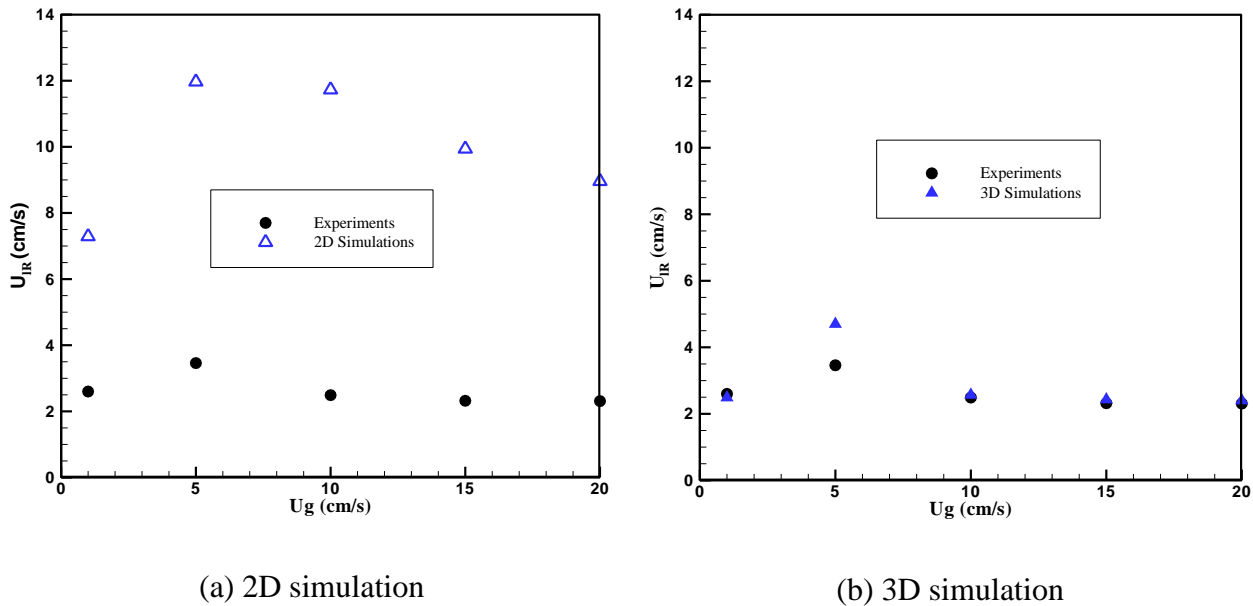
Figure 5.10. Comparison of (a) 2D and (b) 3D average riser superficial liquid velocity simulations with experiments for the external loop airlift reactor at different superficial gas velocities.

Figure 5.11 compares instantaneous gas holdup contours at 10, 15, and 20 cm/s superficial gas velocities. Figure 5.11 presents the gas-liquid flows for a transitional flow (U_g= 10 cm/s) and a slug flow (U_g= 20 cm/s). The flow profile at 15 cm/s superficial gas velocity is a combination slug-transitional flow. The details of the flow regimes will be discussed in the next section. It was observed that the 2D dynamic liquid heights are higher than the 3D predictions for both riser and downcomer for all cases. In addition, the gas-rich pocket region in the downcomer near the upper connector increased as the superficial gas velocity increased. For instance, the gas bubble region spans from 110 to 120 cm height at 10 cm/s, from 100 to 120 cm height at 15 cm/s, whereas it spans from 80 to 120 cm height at 20 cm/s superficial gas velocity with respect to the 3D simulations.
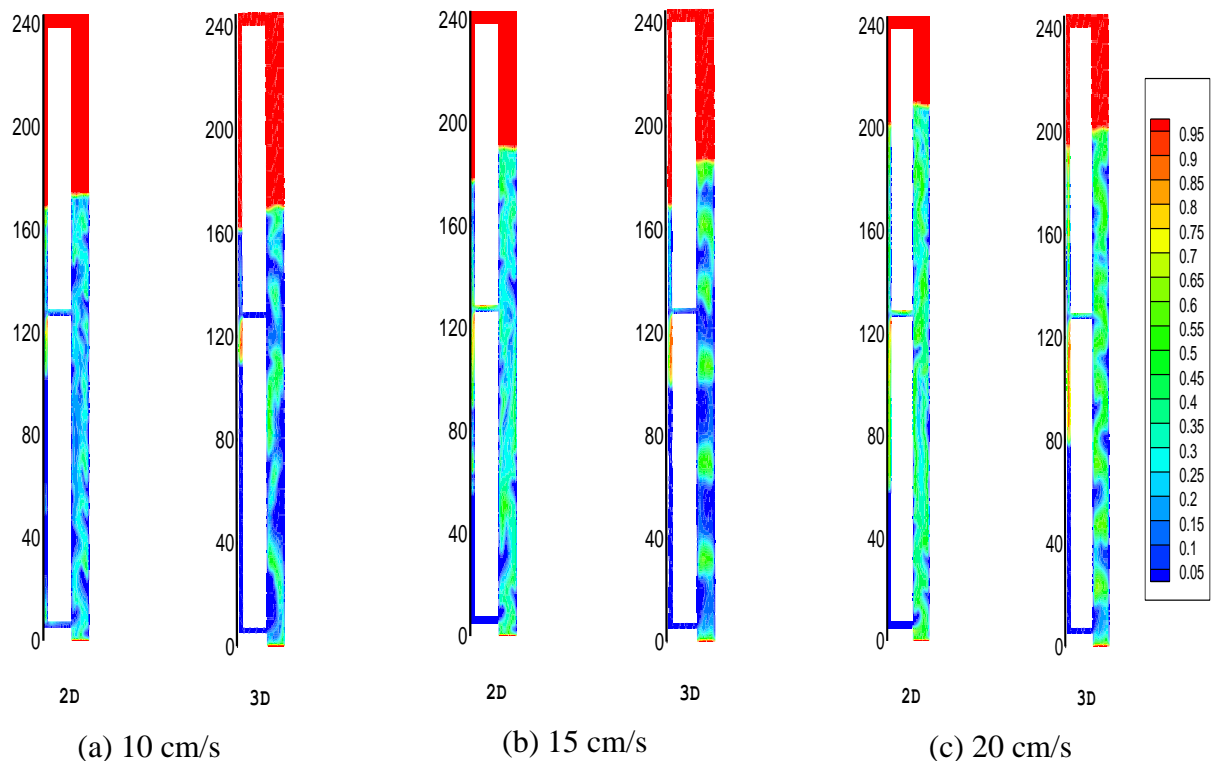
Figure 5.11. Instantaneous gas holdup contours comparing 2D and 3D at (a) 10, (b) 15, and (c) 20 cm/s superficial gas velocities of external loop airlift reactor.

A comparison of the riser hydrodynamic variables at different heights above the distributor plate of external loop airlift reactor between 2D and 3D simulations is investigated. The intention is to understand the flow dynamics within the reactor operating at different velocities. The hydrodynamic variables of average gas holdup (α_{gR}) and axial velocity of the liquid (V_{lR}) and gas phases (V_{gR}) are presented for 2D and 3D simulations at 67, 97, and 117 cm heights above the plate for 10 cm/s (Figure 5.13), 15 cm/s (Figure 5.14), and 20 cm/s (Figure 5.15) superficial gas velocities. According to the flow regime map by Shah and Deckwer [30] as shown in Figure 5.12, the flow regimes of a 10.2 cm diameter reactor at 10, 15, and 20 cm/s superficial gas velocities fall within transitional flow, the onset of slug flow, and slug flow regimes, respectively. Figure 5.13 and Figure 5.14 show that the liquid and gas axial velocity profiles at 117 cm above the distributor plate concentrate toward the left of the riser column as compared with the heights at 67 and 97 cm. That is due to the flow approaching the upper connector that is positioned at the left of the riser column as shown in Figure 5.1. In addition, at U_g=10 cm/s (Figure 5.13) the 3D simulations show a more parabolic gas holdup profile than the 2D simulations, which tend to be more uniform. In general, the time-averaged gas holdup profiles in the riser are comparable for both 2D and 3D simulations in terms of magnitude. The 3D simulations also predict a slightly lower axial liquid and gas velocity as compared with the 2D simulations because of the azimuthal contribution.
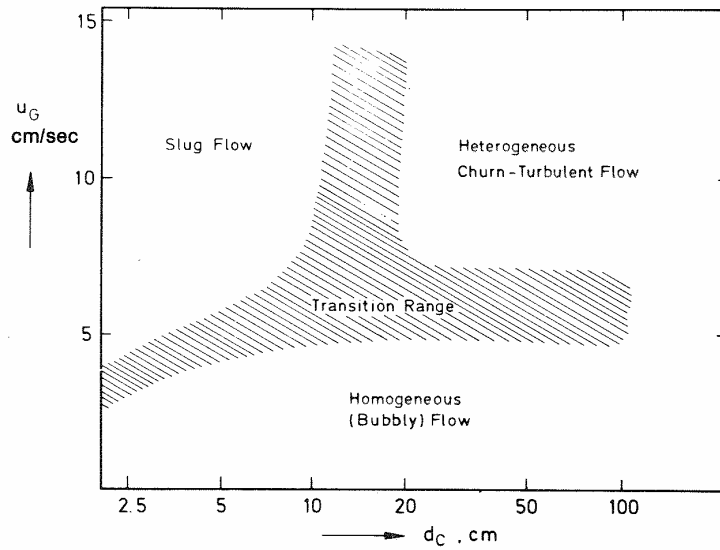
Figure 5.12. Flow regime map by Shah and Deckwer [30].

The 3D simulations at 15 cm/s superficial gas velocity exhibit meandering gas bubbles as well as a slug flow as compared with the 2D simulations and may be attributed to flow moving azimuthally, which is restricted in 2D. For instance, the meandering flow behavior is more profound at 10 and 15 cm/s superficial gas velocities than the 20 cm/s superficial gas velocity as shown in Figure 5.15 due to the transition from a transitional to a pure slug flow regime.

2D Simulations   **3D Simulations**
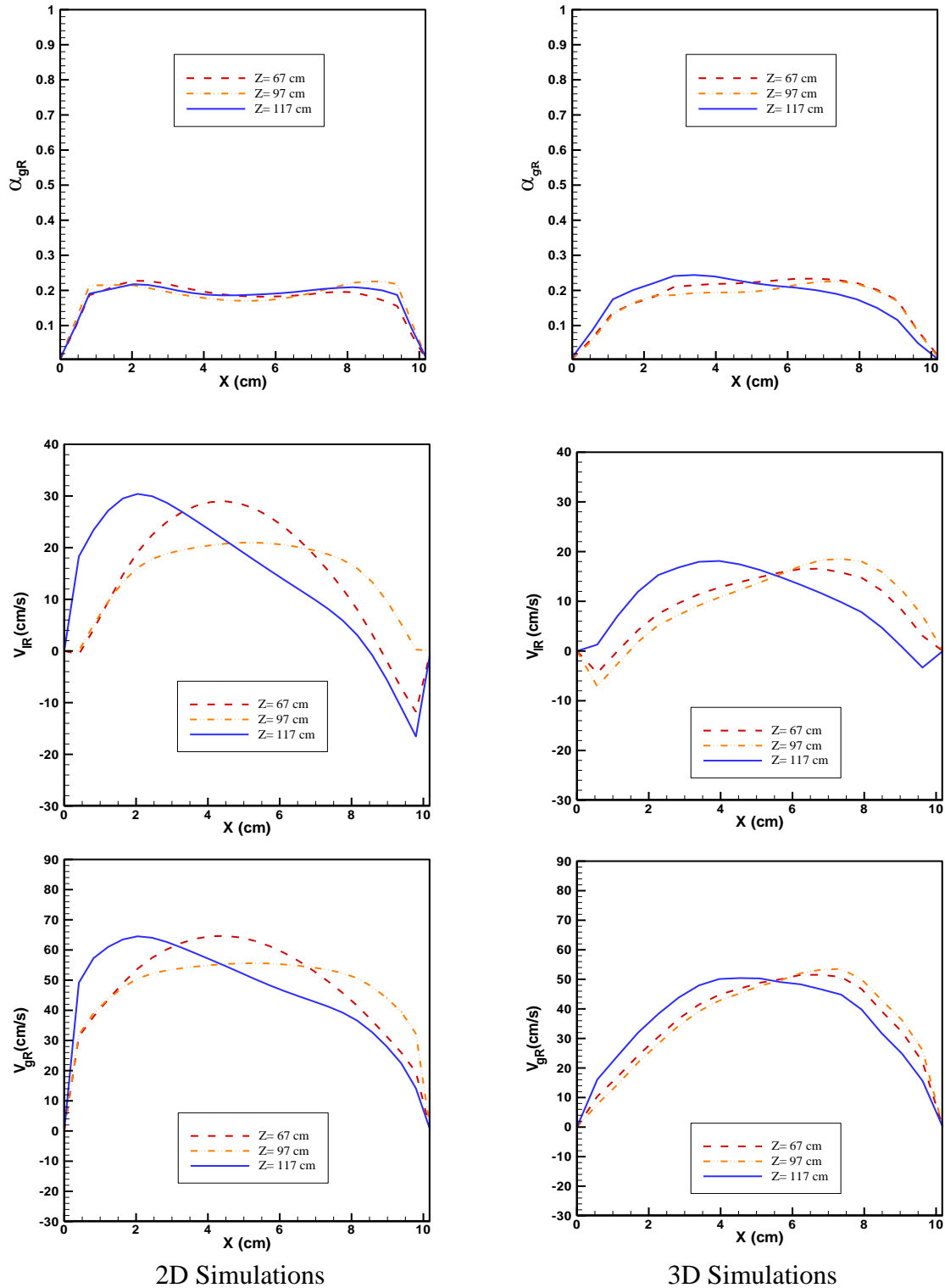
Figure 5.13. Comparison of 2D (left column) and 3D (right column) simulations for 10 cm/s superficial gas velocities time-averaged riser gas holdup (top row), riser axial liquid velocity (middle row), and riser axial gas velocity (bottom row) simulations at 67, 97, and 117 cm heights for the external loop airlift reactor.
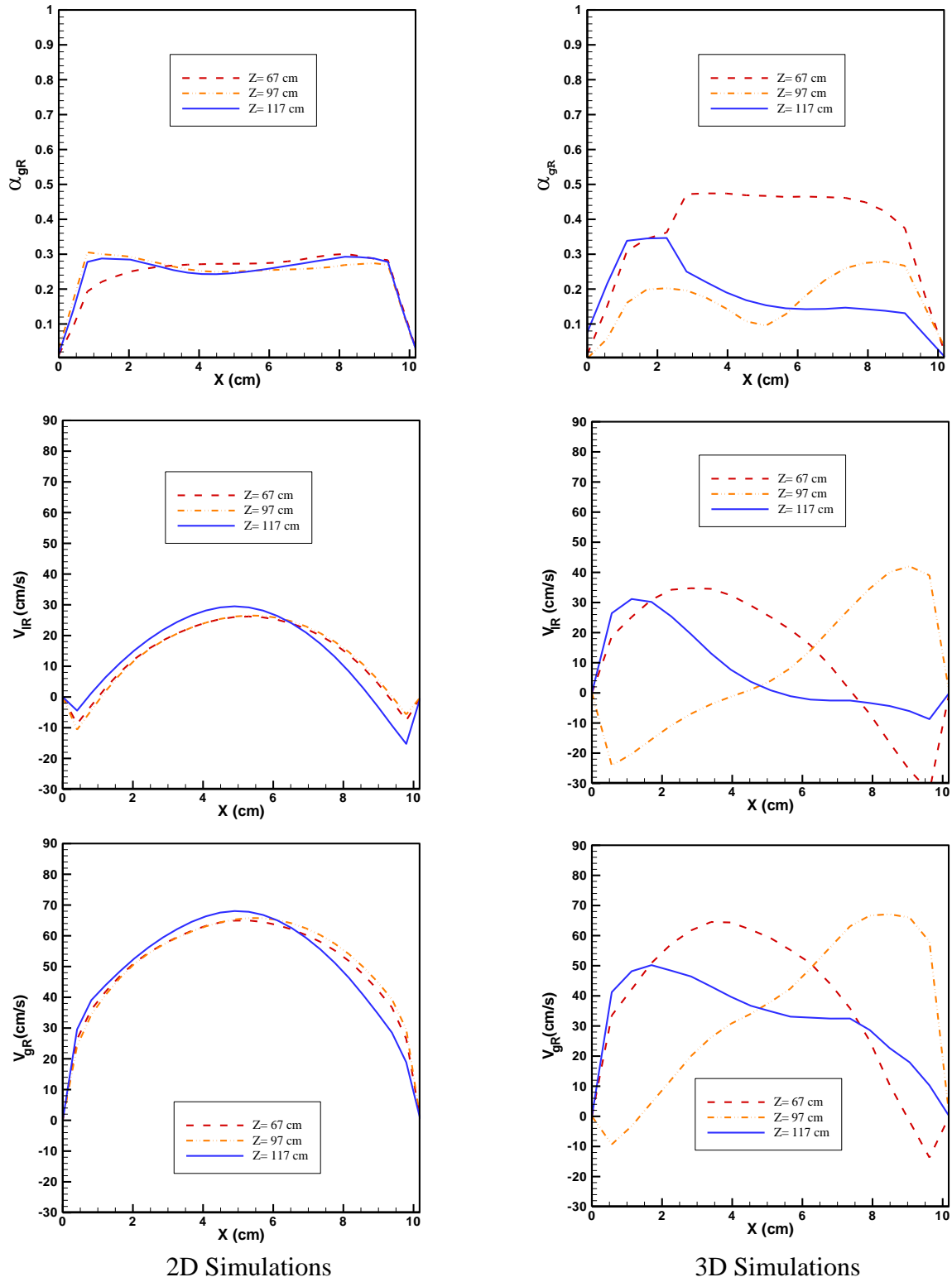
Figure 5.14. Comparison of 2D (left column) and 3D (right column) simulations for 15 cm/s superficial gas velocities time-averaged riser gas holdup (top row), riser axial liquid velocity (middle row), riser axial gas velocity (bottom row) simulations at 67, 97, and 117 cm heights for the external loop airlift reactor.

2D Simulations   3D Simulations
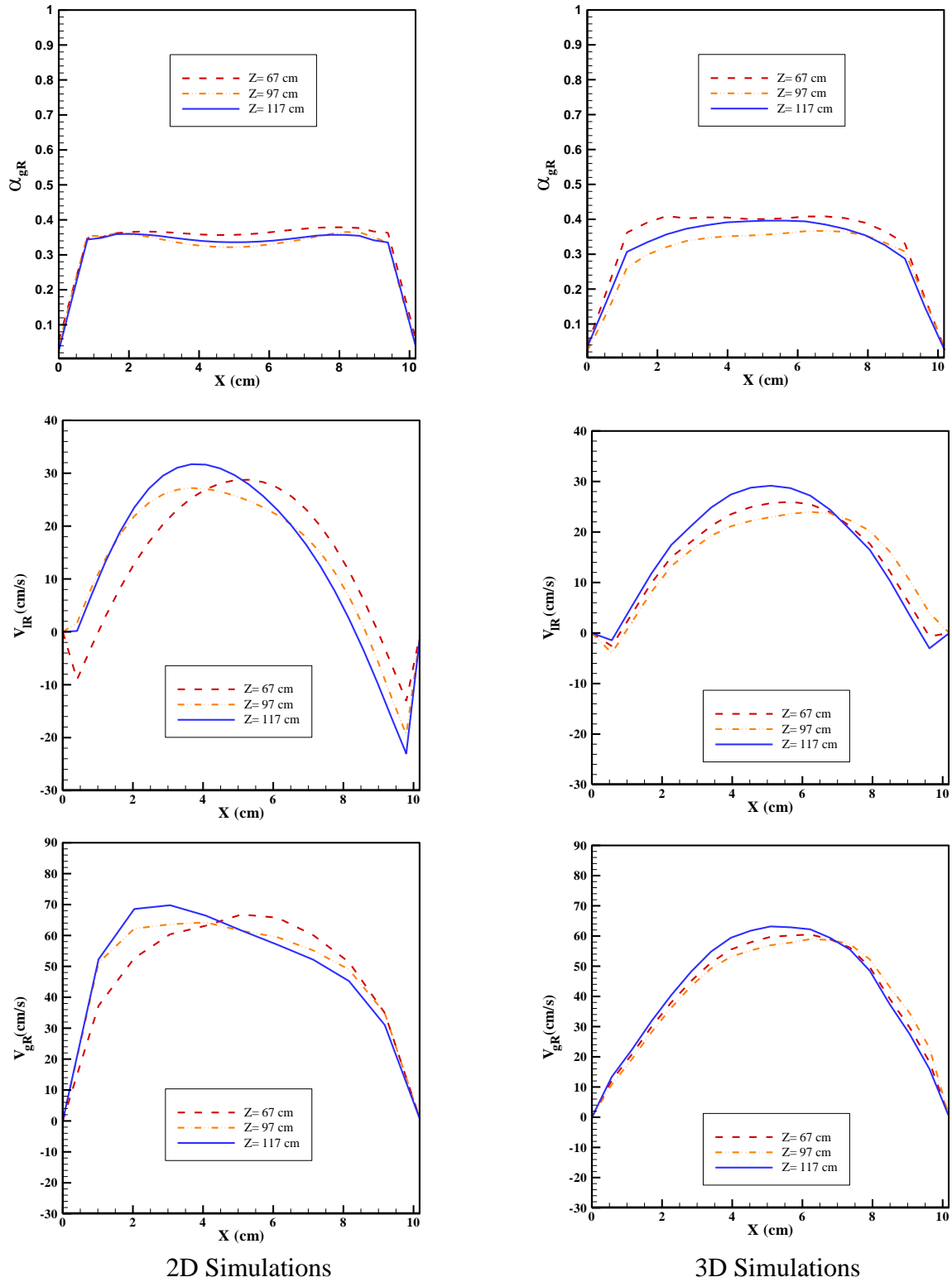
Figure 5.15. Comparison of 2D (left column) and 3D (right column) simulations for 20 cm/s superficial gas velocities time-averaged riser gas holdup (top row), riser axial liquid velocity (middle row), riser axial gas velocity (bottom row) simulations at 67, 97, and 117 cm heights for the external loop airlift reactor.

91

5.6. Conclusions

The gas-liquid flow dynamics in an external loop airlift reactor were simulated using CFDLib in two- and three-dimensional Cartesian coordinates using the Schiller-Naumann drag coefficient model. The turbulence modeling choices of the BP+BIT or multiphase k-ε model and a parametric study on the appropriate effective bubble diameter size were performed. Simulations of the airlift reactor operating with different downcomer configurations were also investigated. Temporal and spatial averaged gas holdup was computed and compared to experimental measurements for the ELALR. For the BC mode, the 2D numerical predictions agreed well with experiments except at $U_g = 5$ cm/s, which was considered a transitional flow regime. The approximate bubble diameter size used in the simulations was found to be close to experimental observation (within 0.4 and 0.5 cm), and this notion was further substantiated when the simulations were performed for a 3D domain. It was concluded that when performing 2D and 3D simulations, care must be taken when specifying the effective bubble diameter size, especially at high flow rates.

Similar findings in terms of bubble diameter size and turbulence models were found for the external loop airlift reactor study. The bubble diameter size for the simulations increased as superficial gas velocity increased for the external loop airlift reactor, which qualitatively corresponds to experimental observations. To conclude, the 3D external loop airlift reactor simulations compared quantitatively well with experiments especially for the riser superficial liquid velocity as compared with the counterpart 2D simulations. The 3D simulations also predicted flow profiles that are in agreement with the profiles of flow regime map. This

observation indicated that the azimuthal flow captured by 3D simulations improved the numerical predictions with experiments.

References

[1] Chisti, M.Y., 1989, "Airlift Bioreactors", Elsevier Applied Biotechnology Series, Elsevier Applied Science, London.

[2] Mudde, R.F., and Van Den Akker, H.E.A., 2001, "2D and 3D Simulations of an Internal Airlift Loop Reactor on the Basis of a Two-Fluid Model", Chemical Engineering Science, 56, pp. 6351-6358.

[3] Roy, S., Dhotre, M.T., and Joshi, J.B., 2006, "CFD Simulation of Flow and Axial Dispersion in External Loop Airlift Reactor", Chemical Engineering Research and Design, 84(A8), pp. 677-690.

[4] Bentifraouine, C., Xuereb, C., and Riba, J.-P., 1997, "Effect of Gas Liquid Separator and Liquid Height on the Global Hydrodynamic Parameters of an External Loop Airlift Contactor", Chemical Engineering Journal, 66(2), pp. 91-95.

[5] Snape, J.B., Zahradnik, J., Fialova, M., and Thomas, N.M., 1995, "Liquid-Phase Properties and Sparger Design Effects in an External-Loop Airlift Reactor", Chemical Engineering Science, 50(20), pp. 3175-3186.

[6] Gavrilescu, M., and Tudose, R.Z., 1996, "Effects of Downcomer-to-Riser Cross Sectional Area Ratio on Operation Behavior of External Loop Airlift Bioreactors", Bioprocess Engineering, 15(2), pp.77-85.

[7] Merchuk, J.C., and Stein, Y., 1981, "Local Holdup and Liquid Velocity in Air-Lift Reactors", AIChE Journal, 27(3), pp. 377-388.

[8] Wang, T., Wang, J., and Jin, Y., 2004, "Experimental Study and CFD Simulation of Hydrodynamic Behaviours in an External Loop Airlift Slurry Reactor", The Canadian Journal of Chemical Engineering, 82(6), pp. 1183-1190.

[9] Dhaouadi, H., Poncin, S., Hornut, J.M., and Wild, G., 2006, "Solid Effects on Hydrodynamics and Heat Transfer in an External Loop Airlift Reactor", Chemical Engineering Science, 61(4), pp. 1300-1311.

[10] Zhang, T., Wang, J., Wang, T., Lin, J., and Jin, Y., 2005, "Effect of Internal on the Hydrodynamics in External-Loop Airlift Reactors", Chemical Engineering and Processing, 44(1), pp. 81-87.

[11] Nikakhtari, H., and Gordon, A.H., 2005, "Hydrodynamic and Oxygen Mass Transfer in an External Loop Airlift Bioreactor with a Packed Bed", Biochemical Engineering Journal, 27(2), pp. 138-145.

[12] Choi, K.H., 2007, "Effects of Aerated Liquid Level above Downcomer on Hydrodynamic Characteristics of an External-Loop Airlift Reactor", Chemical Engineering Communications, 194(9), pp. 1215-1228.

[13] Cao, C., Dong, S., and Guo, Q., 2007, "Experimental and Numerical Simulation for Gas-Liquid Phases Flow Structure in an External-Loop Airlift Reactor", Industrial and Engineering Chemical Research, 46, pp. 7317-7327.

[14] Monahan, S.M., Vitankar, V.S., and Fox, R.O., 2005, "CFD Predictions for Flow-Regime Transitions in Bubble Columns", AIChE Journal, 51, pp. 1897-1923.

[15] Pan, Y., Dudukovic, M.P., 2000, "Numerical Investigation of Gas-Driven Flow in a 2-D bubble columns", AIChE Journal, 46, pp. 434-449.

[16] Rampure, R.M., Buwa, V.V., and Ranade, V.V., 2003, "Modeling of Gas-Liquid/Gas-Liquid-Solid Flows in Bubble Columns", Chemical Engineering Communications, 193, pp. 1-23.

[17] Sanyal, J., Vasquez, S., Roy, S., and Dudukovic, M.P., 1999, "Numerical Simulation of Gas-Liquid Dynamics in Cylindrical Bubble Column Reactors", Chemical Engineering Science, 54, pp. 5071-5083.

[18] Sokolichin, A., and Eigenberger, G., 1994, "Gas-Liquid Flow in Bubble Columns and Loop Reactors: I. Detailed Modeling and Numerical Simulation", Chemical Engineering Science, 49, pp. 5735-5746.

[19] Delnoij, E., Lammers, F.A., Kuipers, J.A.M., and van Swaaij, W.P.M., 1997a, "Dynamic Simulation of Dispersed Gas-Liquid Two-Phase Flow using a Discrete Bubble Model", Chemical Engineering Science, 52(9), pp. 1429-1458.

[20] Delnoij, E., Kuipers, J.A.M., and van Swaaij, W.P.M., 1997b, "Dynamic Simulation of Gas-Liquid Two-Phase Flow: Effect of Column Aspect Ratio on the Flow Structure", Chemical Engineering Science, 52(21/22), pp. 3759-3772.

[21] Delnoij, E., Kuipers, J.A.M., and van Swaaij, W.P.M., 1997c, "Computational Fluid Dynamics Applied to Gas-Liquid Contactors", Chemical Engineering Science, 52(21/22), pp. 3623-3638.

[22] Law, D., Battaglia, F., and Heindel, T.J., 2008, "Model Validation for Low and High Superficial Gas Velocity Bubble Column Flows", Chemical Engineering Science, 63, pp. 4605-4616.

[23] Jones, S.T., and Heindel, T.J., 2006, "The Effect of a Modified Downcomer on the Hydrodynamics in an External Loop airlift Reactor", Proceedings of the ASME Joint U.S.-European Fluids Engineering Summer Meeting, FEDSM2006-98011, Miami, FL.

[24] Jones, S.T., 2007, "Gas-Liquid Mass Transfer in an External Airlift Loop Reactor for Syngas Fermentation", Ph.D. Thesis, Dept. of Mechanical Engineering, Iowa State University, Ames, IA.

[25] Figliola, R.S., and Beasley, D.E., 2000, "Theory and Design for Mechanical Measurement", 3rd ed, John Wiley & Sons Inc, New York.

[26] Shah, Y.T., and Deckwer, W-D, 1983, "Hydrodynamics of Bubble Columns", Handbook of Fluids in Motion, Ann Arbor, MI: Ann Arbor Science, pp. 583-620.

[27] Chen, R.C., Reese, J., and Fan, L.-S., 1994, "Flow Structure in a Three-Dimensional Bubble Column and Three-Phase Fluidized Bed," AIChE Journal, 40(7), pp. 1093-1104.

[28] Joshi, J.B., 2001, "Computational Flow Modeling and Design of Bubble Column Reactors", Chemical Engineering Science, 56 (21-22), pp. 5893-5933.

[29] Padial, N.T., VanderHeyden, W.B., Rauenzahn R.M., Yarbro, S.L., 2000, "Three-Dimensional Simulation of a Three-Phase Draft-Tube Bubble Column", Chemical Engineering Science, 55, pp. 3261-3273.

[30] Shah, Y.T., & Deckwer, W.-D., 1983, "Hydrodynamics of Bubble Columns." Handbook of Fluids in Motion, Cheremisinoff, N.P., and Gupta, R., eds. Ann Arbor, MI: Ann Arbor Science, pp. 583-620.

CHAPTER 6. POPULATION BALANCE SIMULATIONS OF EXTERNAL LOOP AIRLIFT REACTOR FLOWS

6.1. Introduction

In bubble column and external loop airlift reactors, the gas phase exists as a dispersed bubble phase in a continuous liquid phase. The gas phase is characterized by one of the two characteristics regimes depending on the condition of dispersion, namely, the homogeneous and heterogeneous regimes. The homogeneous regime occurs at a relatively low superficial gas velocity (less than about 5-8 cm/s) and is relatively independent of the reactor diameter. Uniformly sized bubbles characterize this regime and the gas holdup is almost uniform in the azimuthal direction. The heterogeneous regime occurs at a relatively high superficial gas velocity for reactor diameters greater than 20 cm. This regime is characterized by non-uniformly sized bubbles and higher gas holdup at the center of the column as compared with the near wall region.

It was observed that an appropriate mean bubble diameter size had to be determined by trial and error method for satisfactory numerical predictions with experiments for the heterogeneous flow regime of the bubble column (BC) mode simulations in Chapter 5. This limitation does not represent the experimental observations where there is a distinct bubble size distribution for the heterogeneous flow regime. The bubble size distribution is caused by bubble break-up and coalescence phenomena. To resolve this limitation, an implementation of the bubble population balance closure models and fixed pivot equations [1] into the two-fluid Eulerian-Eulerian model of air-water bubble column flows is needed to remove the guess of mean bubble size for the computational fluid dynamics (CFD)

predictions with experiments for heterogeneous flow. The implemented population balance models (PBM) will be validated with the experimental data of Degaleesan et al. [2] and the FLUENT population balance simulations performed by Chen et al. [3]. The validated PBM code will also be used to perform 2D and 3D simulations of external loop airlift reactor flows.

6.1.1. Bubble Break-Up

Bubble break-up occurs through bubble interactions with turbulent eddies. The turbulent eddies for break-up are equal to or marginally smaller than the bubble size. Larger eddies simply convect the bubbles without generating break-up whereas very small eddies do not contain sufficient energy to cause the break-up. Similarly, the bubble break-up is modeled by bubble collision rate and probability of bubbles that will result in break-up. The break-up model developed by Luo and Svendsen [4] will be employed in the present study.

6.1.2. Bubble Coalescence

The bubble coalescence process is analyzed by examination of bubble collision events and the probability of collisions resulting in coalescence. Bubble coalescence is modeled by considering bubble collisions due to turbulence and coalescence efficiency of collisions. Coalescence of two bubbles in turbulent flows occurs in three steps. Initially, bubbles collide and trap a small amount of liquid between them. Then, this liquid drains until the liquid film separating the bubbles reaches a critical thickness and film rupture will occur. The coalescence rate is associated with coalescence efficiency, which is to determine whether a given collision will result in coalescence. Two bubbles will coalesce provided that they remain in contact for a period of time sufficient for the liquid film between them to thin

to the critical value necessary for rupture. In this study, the coalescence model from Prince and Blanch [5] will be used.

6.2. Previous Work on Population Balance Simulations of Bubble Columns

Several authors performed CFD population balance simulations of bubble column flows for the heterogeneous regime during the last few years. Olmos et al. [6] conducted 2D axisymmetric CFD simulations of a bubble column of diameter 10 cm and height 135 cm using 10 bubble size groups with the commercial CFD package, CFX. The break-up model from Luo and Svendsen [4] and coalescence model from Prince and Blanch [5] were used. Their simulations had reasonable agreement with the experimental axial liquid velocity data but over-predicted the experimental global gas holdup. Similarly, Wang et al. [7] also performed 2D CFD simulations of a bubble column with the population balance closure models using CFX software. Experimental global gas holdup reported by Degaleesan et al. [2] were compared and Wang et al. [8] found reasonable predictions using the population balance model for a heterogeneous flow.

Chen et al. [3] studied the effect of bubble break-up and coalescence closure models on CFD predictions using a 2D axisymmetric assumption with FLUENT. They considered the models of Luo and Svendsen [4] and Prince and Blanch [5] for bubble coalescence and the models of Luo and Svendsen [4] and Martinez- Bazan [8] for bubble break-up. They concluded that the choice of these models does not substantially affect the simulations. Their simulations had comparable agreement with the experimental axial liquid velocity data and a large discrepancy was observed between the experimental gas holdup results and simulations at the central region of the bubble column due to the axisymmetric assumption for the computation of two-phase flow.

6.3. Population Balance Modeling Equations

Population balance is a method for computing the size distribution of the dispersed gas bubble and accounting for the break-up and coalescence effects in bubble column flows. This model considers that several bubble groups with different diameters d_i can be represented by an equivalent phase with the Sauter mean diameter d_g. The implementation of fixed pivot equations [1] and population balance closure models [4, 5] into the CFDLib code to take into account of the non-uniform bubble size distribution are presented as follows.

The general form of the population balance equation for the gas phase bubble size fraction f_i is:

$$\frac{\partial\left(\rho_g \alpha_g f_i\right)}{\partial t} + \nabla \cdot \left(\rho_g \alpha_g f_i \vec{u}_g\right) = S_i \tag{1}$$

where S_i is the source term due to bubble coalescence and break-up; f_i is defined as the ith size group fraction, which has a relationship with the gas holdup as follows:

$$n_i \mathcal{V}_i = \alpha_g f_i \tag{2}$$

where n_i is the ith group number density ($1/cm^3$) and $\mathcal{V}_i$ is the ith group volume (cm^3).

The Sauter mean diameter d_g represents the diameter of a bubble that has the same volume to surface ratio as the entire collection of bubbles, where:

$$\frac{1}{d_g} = \sum_{i=1}^{N_g} \frac{f_i}{d_i} \tag{3}$$

and N_g is the number of bubble size groups. The source term S_i for the ith size group is:

$$S_i = B_{breakup} - D_{breakup} + B_{coalescence} - D_{coalescence} \tag{4}$$

The right hand of the Eq. (4) are the birth (B) and death (D) sources due to bubble break-up and coalescence, respectively. These terms will be discussed next for a bubble size i.

6.3.1. Bubble Break-Up Model

The birth and death sources to break-up for the ith size group based on the fixed pivot technique [1] are:

$$B_{breakup} = \rho_g \alpha_g \sum_{j>i}^{N_g} B_j f_j$$

$$D_{breakup} = -\rho_g \alpha_g f_i \sum_{j<i}^{N_g} B_j \tag{5}$$

where B_j is the specific rate at which bubbles of the jth size group break into bubbles of the ith size group for $j > i$ and from the ith size group to the jth size group for $j < i$. Eq. (5) is substituted into Eq. (4) for the breakup terms. The total source due to the break-up is zero when summed over all size groups. The mass of a particular group can be related to the diameter as follows:

$$m_i = \frac{\pi}{6} \rho_g d_i^3 \tag{6}$$

Luo and Svendsen [4] developed a theoretical model for the bubble break-up in turbulent suspensions. The model is based on the theory of isotropic turbulence and the number density of a particular bubble size. For example, the break-up rate B_j of bubble size j^{th} into size i^{th} is:

$$B_j = \frac{1}{2} \left(f_{BV} \right) C_B \left(1 - \alpha_g \right) \left(\frac{\varepsilon}{d_j^2} \right)^{1/3} \int_{\xi_{min}}^{1} \frac{(1+\xi)^2}{\xi^{11/3}} \exp\left(-\frac{12\left(\left(f_{BV} \right)^{2/3} + \left(1 - \left(f_{BV} \right) \right)^{2/3} - 1 \right)\sigma}{\beta \rho_l \varepsilon^{2/3} d_j^{5/3} \xi^{11/3}} \right) d\xi \tag{7}$$

and f_{BV}, which is the breakup volume fraction, is related to the mass of bubble size groups as follows:

$$f_{BV} = \frac{m_j}{m_i} \tag{8}$$

σ is the surface tension constant, ξ is the dimensionless size of eddies in the inertial subrange of isotropic turbulence, and ρ_l is the liquid density. The lower limit of the integration is given by the ratio of Kolmogorov length scale to bubble size j:

$$\xi_{min} = 11.4 \frac{1}{d_j} \left(\frac{1}{\varepsilon} v_l^3 \right)^{1/4}$$

(9)

where ε is the liquid phase eddy dissipation rate and v_l is the liquid kinematic viscosity. The exponential term compares the bubble surface energy to the impact energy of the eddy to bubble. The integration can be computed with the trapezoidal rule, which was implemented into the CFDLib code as part of this research. In Eq. (7), the empirical constant $\beta = 2$ is the correlation constant between the mean turbulent velocity of a particular eddy size and the eddy size whereas $C_B = 0.923$ is the constant used to correlate the arrival frequency of eddies on the bubble of a particular diameter size. All empirical constants are only applicable for the air-water system.

6.3.2. Bubble Coalescence Model

The birth and death sources to the ith size group due to coalescence based on the fixed pivot technique [1] are:

$$B_{coalescence} = \left(\rho_g \alpha_g \right)^2 \left(\frac{1}{2} \sum_{j=1}^{i} \sum_{k=1}^{i} C_{jk} f_j f_k \frac{m_j + m_k}{m_j m_k} X_{jki} \right)$$

$$D_{coalescence} = \left(\rho_g \alpha_g \right)^2 \left(-\sum_{j=1}^{N_g} C_{ij} f_i f_j \frac{1}{m_j} \right)$$

(10)

where C_{ij} is the specific coalescence rate between the ith and j^{th} bubble groups. In Eq. (10), X_{jki} is the fraction of mass due to coalescence between the j and k groups that forms group i. The mass fractions for coalescence are:

$$X_{jki} = \begin{cases} \dfrac{m_j + m_k - m_{i-1}}{m_i - m_{i-1}} & m_{i-1} < m_j + m_k < m_i \end{cases}$$

$$X_{jki} = \begin{cases} \dfrac{m_{i+1} - (m_j + m_k)}{m_{i+1} - m_i} & m_i < m_j + m_k < m_{i+1} \end{cases}$$

$$X_{jki} = 0 \quad \text{otherwise}$$

The net source due to coalescence is zero when summed over all size groups provided that $C_{ij} = C_{ji}$ and $\Sigma\, X_{jki} = 1$.

Prince and Blanch [5] assumed that the coalescence of two bubbles occurs in three steps. First, the bubbles collide trapping a small amount of liquid between them; this liquid film drains until the liquid film separating the bubbles reaches a critical thickness; the film then ruptures, and the bubbles join together. The coalescence process is therefore modeled by a collision rate of two bubbles and a collision efficiency η_{ij} relating to the time required for coalescence. In the current implementation, the coalescence model from Prince and Blanch [5] is used for the modeling of collision frequency:

$$C_{ij} = S_{ij} \left(u_{ti}^2 + u_{tj}^2 \right)^{1/2} \eta_{ij} \tag{11}$$

The variables presented on the right hand side of Eq. (11) are defined with their associated equations as follows. The collision efficiency η_{ij} is modeled by comparing the time required for coalescence t_{ij} with the estimated contact time during the collision τ_{ij} [9]:

$$\eta_{ij} = \exp\left(\frac{-t_{ij}}{\tau_{ij}} \right) \tag{12}$$

$$t_{ij} = \left(\frac{\rho_l r_{ij}^3}{16\sigma} \right)^{1/2} \ln\left(\frac{h_o}{h_f} \right) \tag{13}$$

$$\tau_{ij} = \frac{r_{ij}^{2/3}}{\varepsilon^{1/3}} \tag{14}$$

where ρ_l, σ, and ε have the same definitions as in Eq. (7). The estimated initial film thickness is h_o for air-water systems and h_f is the critical film thickness when rupture occurs, which are $h_o = 1 \times 10^{-4}$ m as reported by Kirkpatrick and Locket [10] and $h_f = 1 \times 10^{-8}$ m as reported by Kim and Lee [11]. The equivalent radius r_{ij} is:

$$r_{ij} = \frac{1}{2}\left(\frac{1}{r_i} + \frac{1}{r_j}\right)^{-1} \tag{15}$$

The cross-sectional area S_{ij} of the colliding bubble sizes i and j is defined as:

$$S_{ij} = \frac{\pi}{16}\left(d_i + d_j\right)^2 \tag{16}$$

The turbulent velocity in the inertial subrange of isotropic turbulence is:

$$u_{ti} = \sqrt{2}\left(\varepsilon d_i\right)^{1/3} \tag{17}$$

The inlet bubble size d_b produced at the orifice of the distributor plate is calculated using the correlation of Miyahara et al. [12], where:

$$d_b = f\left(N_w\right)\left(\frac{\sigma d_o}{g\rho_l}\right)^{1/3} \tag{18}$$

and N_w relates the Weber number We, which is a dimensionless number comparing the fluid's inertia to its surface tension, to the Froude number Fr, which is a dimensionless number comparing inertia and gravitational forces:

$$N_w = We / Fr^{1/2} = \frac{d_o^{1.5} U_g \rho_l g^{0.5}}{\sigma} \tag{19}$$

with:

$f(N_w) = 2.9$ for $N_w \leq 1$

$f(N_w) = 2.9\ N_w^{-0.188}$ for $1 \leq N_w \leq 2$

$f(N_w) = 1.8\ N_w^{0.5}$ for $2 \leq N_w \leq 4$

$f(N_w) = 3.6$ for $4 < N_w$

The parameter d_o refers to orifice hole size of the distributor plate.

6.4. Validation of the PBM Implementation

The bubble column geometry and operating conditions of Degaleesan et al. [2] are simulated and validated in the present work after having implemented the population balance model into CFDLib. A 14 cm diameter bubble column is initially filled with 98 cm of water and air is injected at 9.6 cm/s superficial gas velocity, as shown in Figure 6.1. At the inlet, the bubble size is specified as $d_b = 0.4$ cm, based on the hole size of the distributor plate used in the experiments [2] and Eq. (18). Two-dimensional and three-dimensional bubble column simulations using a Cartesian coordinate system are performed and Table 6.1 summarizes the grid resolution, which was determined based on the study in Chapter 4. The Schiller-Naumann drag coefficient model was used. All simulations are time-averaged from 20 to 90 seconds with 7000 realizations. The current study investigates five bubble size distributions, which are tabulated in Table 6.2. The determination of bubble size is based upon the bubble volume interval such that $V_i = nV_{i-1}$ where index i refers to the bubble size group, $n = 2$ for 10 and 12 bubble sizes, and $n = 4$ for 6 and 8 bubble sizes as shown in Table 6.2. The 2D CPU per time step per cell with 10 bubble diameter sizes are approximately 10 times greater than the 2D one bubble diameter size shown in Table 5.1. Table 6.1 also presents the CPU information of 2D and 3D PBM bubble column simulations. The 2D 10 bubble size simulations increase the CPU per time step per cell approximately by 10 times as compared

with the 2D one bubble size simulation. Similar findings regarding CPU information are observed for the 3D simulations.

Table 6.1 Grid resolutions and CPU information used for the PBM bubble column study

|	2D		3D	
Δx (cm)	1.0		1.0	
Δy (cm)	-		1.0	
Δz (cm)	1.0		2.0	
Total cells	2772		13332	
Number of bubble size	1	10	1	10
CPU (s)	2397	34560	36946	201600
Time step (s)	0.004	0.0007	0.002	0.0005
Number of time step	1351	1666	9330	3760
CPU per number of time step per cell	0.00064	0.0075	0.0003	0.004
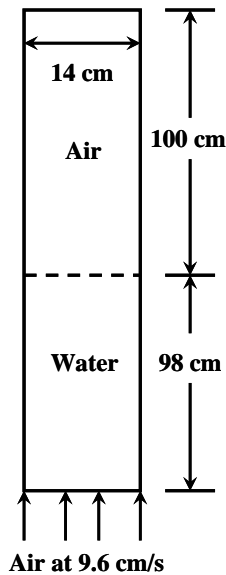
Figure 6.1. Schematic of bubble column geometry and conditions of Degaleesan et al. [2]

**Table 6.2 Assigned bubble sizes of each group for the population balance simulations**

Group	Bubble Size d_i (cm)											
1	0.4											
6	0.159	0.252	0.4	0.635	1.008	1.6						
8	0.1	0.159	0.252	0.4	0.635	1.008	1.6	2.54				
10	0.126	0.159	0.2	0.252	0.317	0.4	0.504	0.635	0.8	1.008		
12	0.1	0.126	0.159	0.2	0.252	0.317	0.4	0.504	0.635	0.8	1.008	1.27

Figure 6.2 presents the comparison of 2D and 3D average axial liquid velocity simulations that are averaged between 20 and 110 cm above the plate with the experiments [2]. The simulations are conducted using the population balance method for 5 bubble size distributions, including a single bubble size, and an isotropic turbulence model. All of the multiple bubble size simulations compare better with the experiments at the near wall region than the one bubble size simulation. For the $n = 2$ bubble volume size interval, the 2D predictions for the 10 size group predicts lower axial liquid velocities as compared with the one bubble size simulation and followed by the 12 size group and likewise for the 6 and 8 size groups in Figure 6.2 (a). The 2D axisymmetric population balance simulations performed by Chen et al. [3] with FLUENT over-predict the experiments, shown as a solid line in Figure 6.2. It should be noted that the 12 size group of the current work uses the same bubble size distribution as Chen et al. [3]. In Figure 6.2 (b), the 3D multi-bubble simulations compare well with experiments [2] and simulations [3], and the single bubble size simulation significantly overpredicts the centerline liquid velocity. The 3D simulation using 8 bubble sizes does not differ significantly from the 10 bubble size simulation. All 3D simulations compare better with the experiments at the near wall region than the 2D simulations. The discontinuities of average axial liquid velocity profiles shown in Figure 6.2 are attributed to the insufficient grid resolution near the wall boundary. Similarly, the average gas holdup profiles are plotted in Figure 6.3 for the 2D and 3D simulations. Figure 6.3 (a) shows that the 2D single bubble size prediction of gas holdup has a different profile than the multiple bubble simulations, whereby a high gas holdup is predicted at the near wall region. The 2D PBM results are comparable with each other among the different bubble size groups and the profiles collapse with increasing bubble size groups. For the 3D simulations, the PBM

106

simulations predict a higher gas holdup as compared with the single bubble size simulation. The gas holdup profiles predicted by the PBM are also comparable with each other in the Figure 6.3 (b).
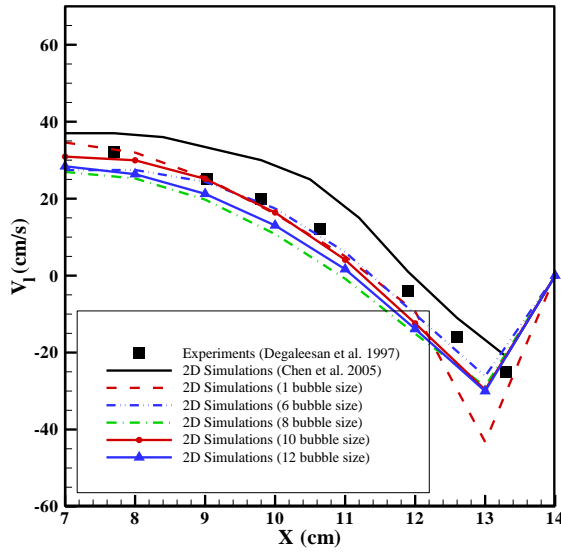
(a) 2D simulations
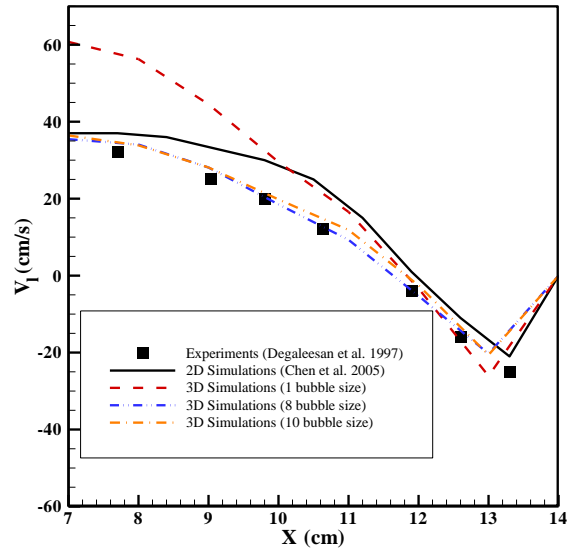
(b) 3D simulations

Figure 6.2. Comparison of (a) 2D and (b) 3D average axial liquid velocity predictions over 20 to 110 cm heights of each bubble size group with experiments at 9.6 cm/s superficial gas velocity with 14 cm bubble column diameter.
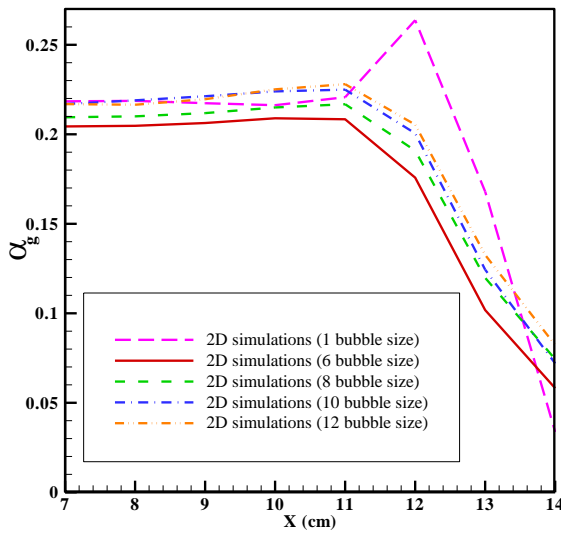
(a) 2D simulations
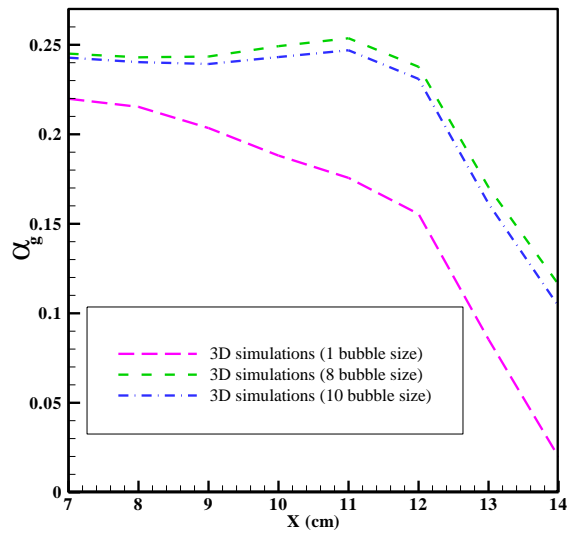
(b) 3D simulations

Figure 6.3. Comparison of (a) 2D and (b) 3D average gas holdup predictions over 20 to 110 cm heights of each bubble size group at 9.6 cm/s superficial gas velocity with 14 cm bubble column diameter.

As other means of comparison, the 2D and 3D time-averaged bubble size distributions predicted for each size group and the simulations of Chen et al. [3] are shown in Figure 6.4 at $Z = 40$ cm. The variable f refers to the size fraction of a particular bubble size and the sum of f for all bubble sizes is unity. The 2D predictions for the 10 and 12 bubble size groups have comparable bubble size distribution profiles with the profile of Chen et al. [3] because they assumed the same bubble volume size interval ($n = 2$). The 6 and 8 size groups ($n = 4$) of the 2D system predict a higher size fraction for bubble sizes between 0.4 cm-1.5 cm as compared with the 10 and 12 size groups. The bubble size distribution profile predicted by each group generally exhibits a log-normal distribution profile, where the mean bubble size is around 0.75 cm. For the 3D simulations, the 10 bubble size group has a peak size fraction at a bubble diameter of 0.4 cm, which is smaller than the 2D predictions. The smaller predicted bubble size of 3D simulations is because of the flows captured at the azimuthal direction and that results in more of the bubble break-up phenomenon. The 3D bubble size fractions also display a log-normal distribution profiles.
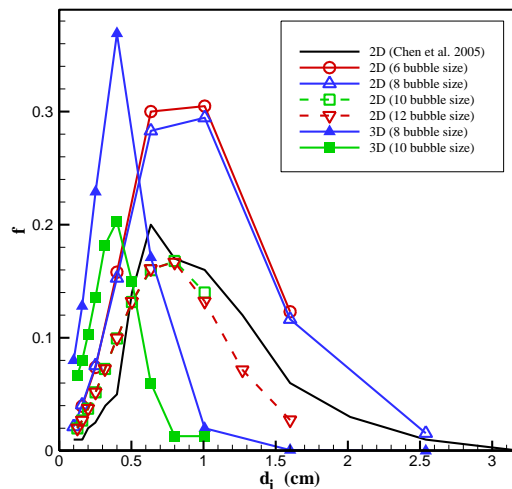

Figure 6.4. Comparison of 2D and 3D time-averaged bubble size distributions predicted by each size group and Chen et al. [3] at 40 cm height of the bubble column.

109

Figure 6.5 shows contours of the 2D instantaneous gas holdup at 90 s simulated for each bubble size group. The one bubble size simulation has a more homogeneous gas holdup as compared with the multi-bubble size simulations, and the multi-bubble size simulations do not show significant differences between each other. The multi-bubble size simulations show streams of gas bubbles moving in an oscillatory motion, which is obscured for the one bubble size profile.


1 bubble size   6 bubble sizes   8 bubble sizes   10 bubble sizes   12 bubble sizes
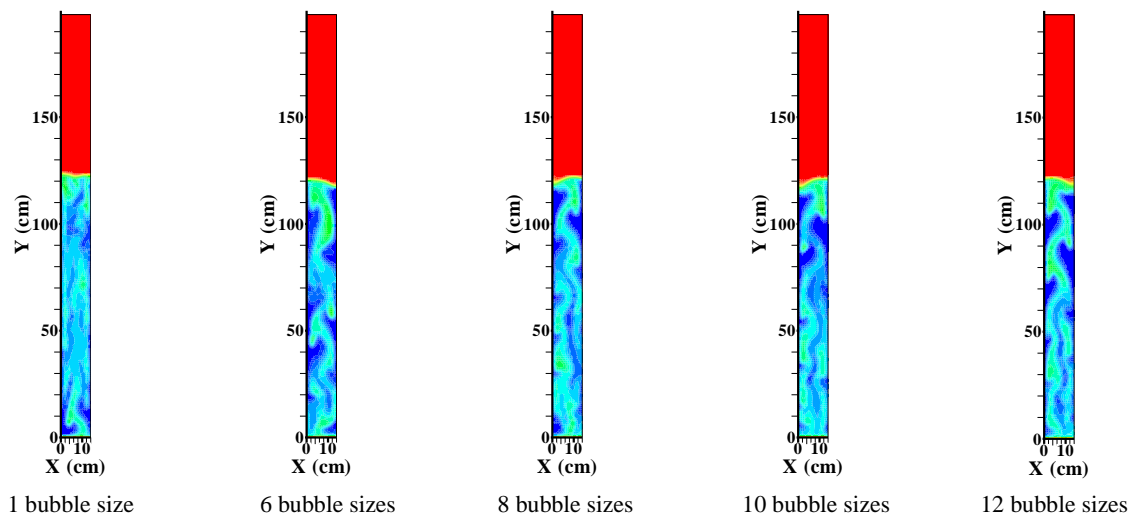
Figure 6.5. Comparison of 2D instantaneous gas holdup contours for each bubble size group at 90 s.

Figure 6.6 compares instantaneous gas holdup predicted using 2D and 3D simulations for 8 and 10 bubble size groups. The 3D predicts a more homogenous gas holdup profile as well as a gas-rich region around the centerline of the column compared to the 2D simulations. The 3D simulations do not present a noticeable difference in terms of the gas holdup between the 8 and 10 bubble sizes, as was noted for he 2D cases.
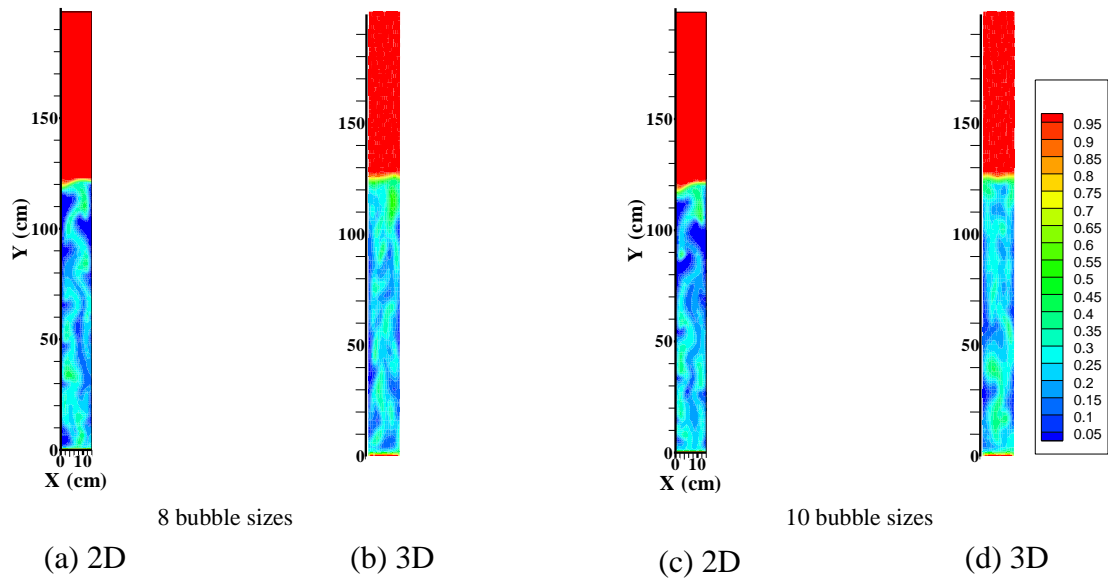
Figure 6.6. Comparison of 2D and 3D PBM instantaneous gas holdup contours at 90s.

Table 6.3 Grid resolutions used for the external loop airlift reactor PBM simulations

|	2D	3D
Δx (cm)	0.408-0.50	0.408-0.50
Δy (cm)	-	0.408-0.50
Δz (cm)	0.90-1.25	1.0
Total cells	9980	183154

6.5. External Loop Airlift Reactor

After validating the implemented PBM code with the bubble column experiments by Degaleesan et al. [2], 2D and 3D simulations are performed for the external loop airlift reactor. The grid resolutions for the 2D and 3D simulations are presented in Table 6.3. A six bubble size group for d_i = 0.222, 0.353, 0.56, 0.889, 1.41, and 2.24 cm is used with the PBM simulations of the external loop airlift reactor to compare with one bubble size of 0.56 cm which is the characteristic bubble size due to the distributor plate (refer to Eq. (18)).

Figure 6.7 (a) shows that the 2D simulations using 1 bubble size and 6 bubble sizes are quite comparable with each other for the gas holdup predictions in the riser, whereas the PBM predicts gas holdup in the downcomer than the single bubble size prediction. Figure 6.7 (b) compares the same simulations for the riser superficial liquid velocity with the experiments [13]. The inconsistent trend of riser superficial liquid velocity from 10 to 15 and from 15 to 20 cm/s superficial gas velocity as shown in Figure 6.7 (b) could be due to the 10 cm/s is at a transitional flow regime. Figure 6.8 presents 2D instantaneous gas holdup contours for the single bubble size and PBM at 10, 15, and 20 cm/s superficial gas velocities. It has to be noted the length of stationary gas bubble at the downcomer near the upper connector is longer predicted by the single bubble size method than that of the multi-bubble size simulations, and the length also increases with the superficial gas velocity for the single bubble size method.

Similarly, the comparison of 3D single bubble size and PBM simulations with experiments are presented for the average gas holdup and riser superficial liquid velocity in Figure 6.9. The 3D PBM simulations predict higher gas holdup and riser superficial liquid velocities than the single bubble size in the riser and predict lower downcomer gas holdup than the single bubble size simulations. In general, the 3D PBM gas holdup and riser superficial liquid velocity simulations agree well with experiments. Figure 6.10 compares 3D instantaneous gas holdup contours for the single bubble size and PBM methods at 15 and 20 cm/s superficial gas velocities. Likewise, the 3D PBM predictions of the stationary gas bubble length in the downcomer near the upper connector are closer to the experimental observations [13] in which the length does not vary substantially at high superficial gas velocities such as from 15 to 20 cm/s. However, the stationary bubble predicted using the 3D

single bubble size increases significantly with the inlet superficial gas velocity. In addition, Jones [13] observed that there are gas bubbles at the bottom region of the downcomer and this phenomenon is only predicted by the 3D multi-bubble size simulations shown in Figure 6.10 whereas the 3D single bubble size simulations predict zero gas holdup. The 3D PBM instantaneous gas holdup contour at 15 cm/s superficial gas velocity also presents more of the slug flow profile than the single bubble size simulation and that agrees better with the prediction of the flow regime map by Shah and Deckwer [14] (refer to Figure 5.12).

Figure 6.11 presents a qualitative comparison of 3D one and six bubble size instantaneous gas holdup predictions with experiment near the upper connector in the downcomer at 20 cm/s superficial gas velocity. The six bubble size simulation near the upper connector in the downcomer predicts a slightly shorter gas bubble length whereas the one bubble size simulation predicts a much longer length than the experiment. Figure 6.12 shows the 2D and 3D bubble size fractions formed at the riser. The ELALR 3D simulations predict smaller bubble sizes than the 2D simulations and this finding is consistent with the results shown in Figure 6.4 for the bubble column. The average experimental bubble size at the riser reported by Jones [13] is within 0.4 and 0.5 cm and this observation is in good agreement with the average bubble size predicted by the 3D PBM simulations that is also within 0.4 and 0.5 cm.
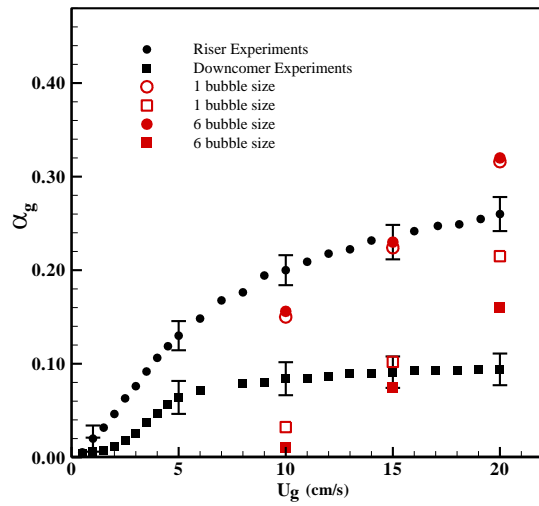
(a) Average Gas Holdup
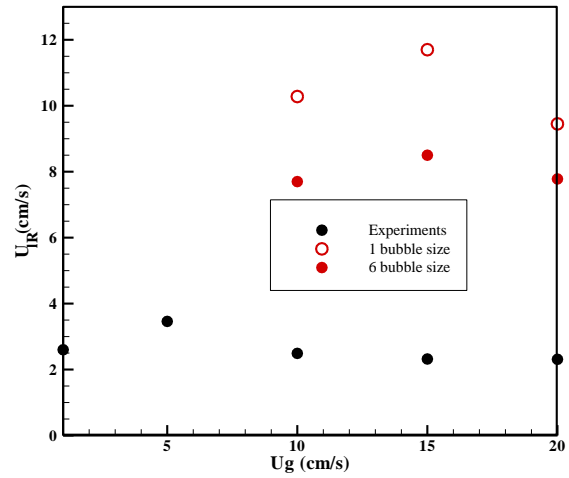
(b) Average Riser Superficial Liquid Velocity

Figure 6.7. **Comparison of 2D (a) average gas holdup and (b) average riser superficial liquid velocity population balance simulations with experiments and single bubble size simulations for the external loop airlift reactor at 10, 15, and 20 cm/s superficial gas velocities.**

1 size   6 sizes   1 size   6 sizes   1 size   6 sizes
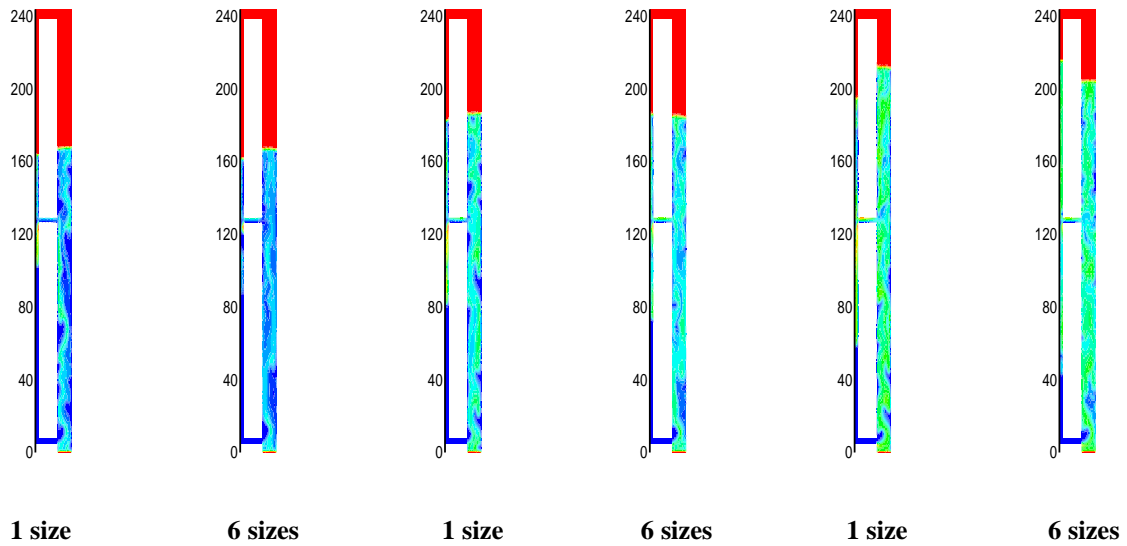
(a) 10 cm/s   (b) 15 cm/s   (c) 20 cm/s

Figure 6.8. Comparison of 2D single and six size instantaneous gas holdup contours at (a) 10, (b) 15, and (c) 20 cm/s superficial gas velocities.
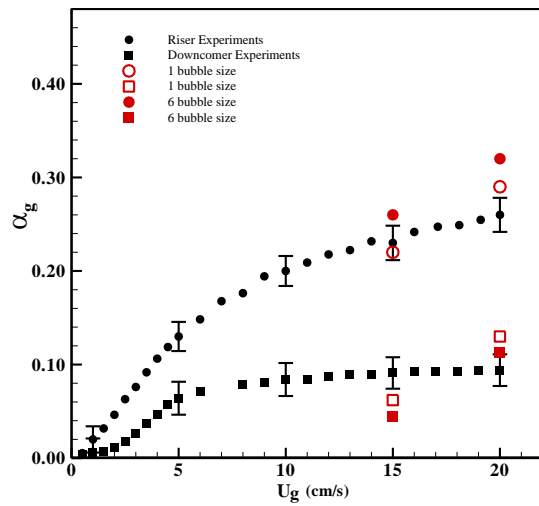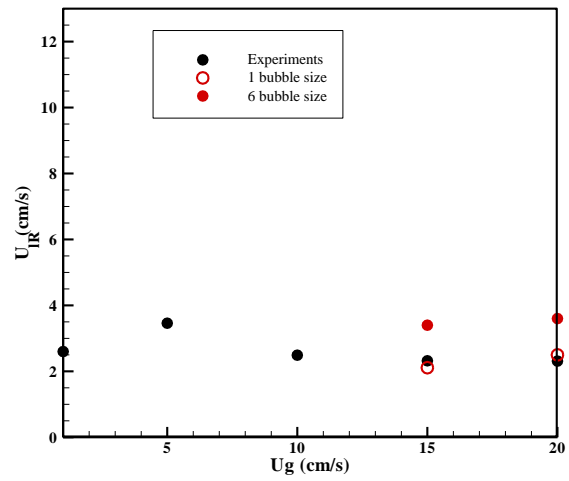
(a) Average Gas Holdup   (b)Average Riser Superficial Liquid Velocity

Figure 6.9. **Comparison of 3D (a) average gas holdup and (b) average riser superficial liquid velocity 6 bubble size simulations with experiments and single bubble size simulations for the external loop airlift reactor at 15 and 20 cm/s superficial gas velocities.**
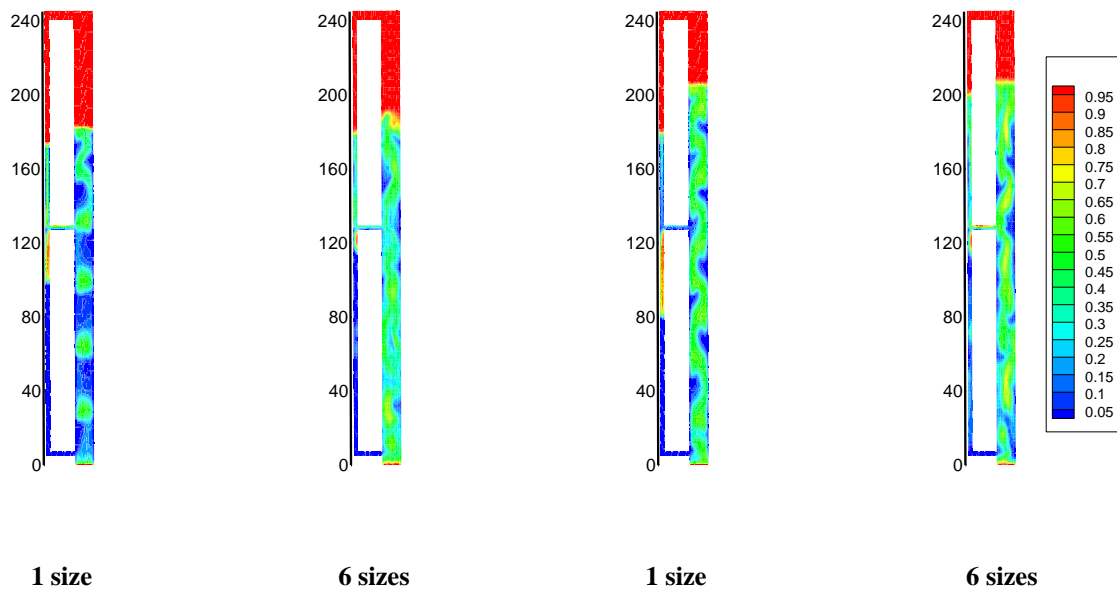
1 size   6 sizes   1 size   6 sizes

(a) 15 cm/s   (b) 20 cm/s

Figure 6.10. Comparison of 3D single size and six size instantaneous gas holdup contours at (a) 15 and (b) 20 cm/s superficial gas velocities.

(a) 1 size   (b) 6 sizes   (c) Experiment
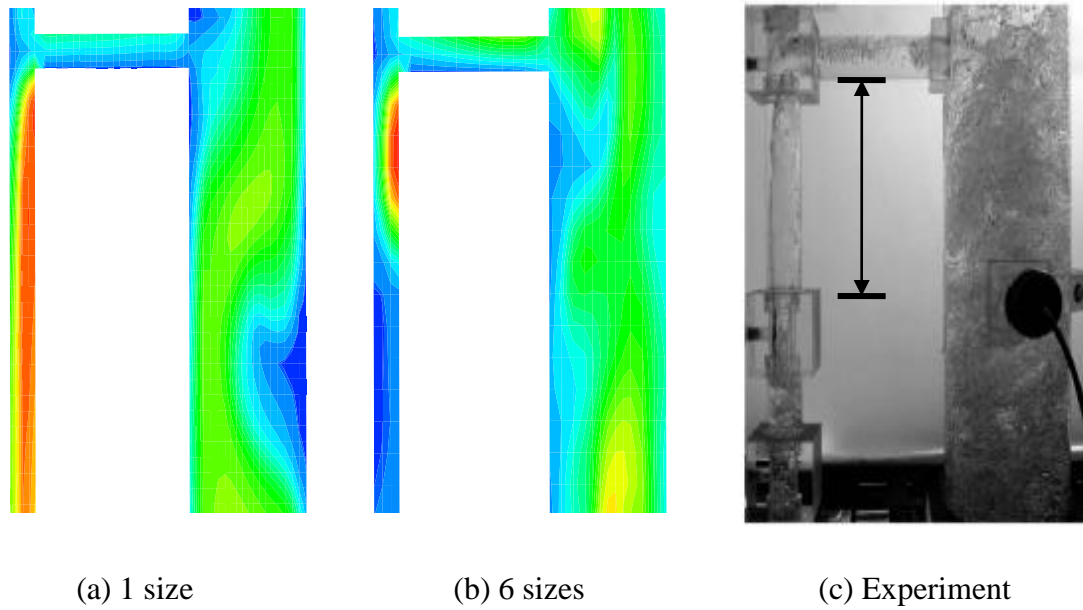
Figure 6.11. Comparison of 3D (a) 1 size and (b) 6 size instantaneous gas holdup simulations with (c) experiment at 20 cm/s superficial gas velocity near the upper connector, where the arrows indicate the approximate length of experimental bubble near the upper connector in the downcomer.
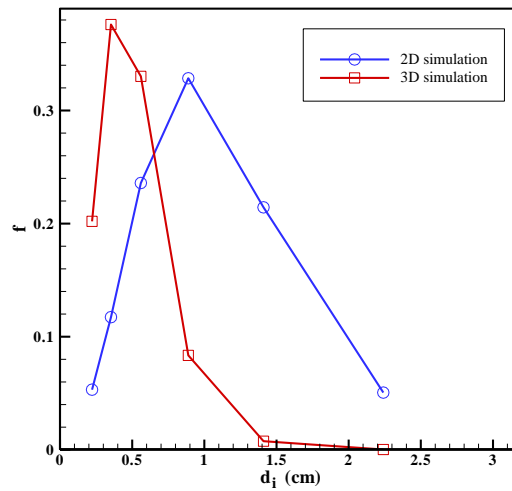

Figure 6.12. Comparison of 2D and 3D simulated bubble sizes for the external loop airlift reactor at the riser at 20 cm/s superficial gas velocity.

6.6. Conclusions

Population balance model simulations for a bubble column and external loop airlift reactor flows were conducted with bubble break-up and coalescence closure models using the fixed pivot method. The PBM simulations were validated with the experimental data of Degaleesan et al. [2] and the results predicted using multiple bubble sizes were in good agreement with the experimental liquid velocity [2] and simulated bubble size distribution profile of Chen et al. [3]. In addition, the PBM simulations compared better with the experiments than the single bubble size simulations. The predicted axial liquid velocity profiles among the different bubble size groups did not present noticeable differences and this justified using a lower number of bubble size groups for PBM simulations. Using the same bubble volume size interval of $n = 2$, the higher number of bubble size groups predicted lower axial liquid velocity and this applied for the bubble size groups for $n = 4$ as well.

The 2D external loop airlift reactor simulations did not present noticeable differences in the results among the single bubble size versus the multiple bubble size group simulations. The 3D multi-bubble size simulations of external loop airlift reactor were performed and the results were again comparable with the one-sized simulation. However, the 3D multi-bubble size simulations had a closer agreement with experimental findings [13] than the single bubble size simulations regarding the physics of gas bubbles in the downcomer such as the negligible increase of the gas bubble length near the upper connector and gas holdup predictions in the bottom region of the downcomer. The 3D PBM simulations also yielded a better prediction of the average bubble size at the riser with the experiments.

References

[1] Kumar, S., Ramkrishna, D., 1996, "On the Solution of Population Balance Equations by Discretization—I. A Fixed Pivot Technique", Chemical Engineering Science, 51, pp. 1311-1332.

[2] Degaleesan, S., Dudukovic, M., Pan, Y., 2001, "Experimental Study of Gas-Induced Liquid Flow Structures in Bubble Columns", Fluid Mechanics and Transport Phenomena, pp. 1913-1931.

[3] Chen, P., Sanyal, J., Dudukovic, M.P., 2005, "Numerical Simulation of Bubble Column Flows: Effect of Different Breakup and Coalescence Closures", Chemical Engineering Science, 60, pp. 1085-1101.

[4] Luo, H., Svendsen, H.F., 1996, "Theoretical Model for Drop and Bubble Breakup in Turbulent Dispersions", American Institute of Chemical Engineering Journal, 42, pp. 1225-1233.

[5] Prince, M.J., Blanch, H.W., 1990, "Bubble Coalescence and Breakup in Air-Sparged Bubble Columns", American Institute of Chemical Engineering Journal, 36, pp. 1485-1499.

[6] Olmos, E., Gentric, C., Vial, C., Wild, G., Midoux, N., 2001, "Numerical Simulation of Multiphase Flow in Bubble Column Reactors: Influence of Bubble Coalescence and Breakup", Chemical Engineering Science, 56, pp. 6359-6365.

[7] Wang, T.F., Wang, J.F., Jin, Y., 2006, "A CFD-PBM Coupled Model for Gas-Liquid Flows", American Institute of Chemical Engineering Journal, 52, pp. 125-140.

[8] Martinez- Bazan, C., Montanes, J.L., Lasheras, J.C., 1999, "On the Break-Up of an Air Bubble Injected into a Fully Developed Turbulent Flow. Part 1. Breakup Frequency", Journal of Fluid Mechanics, 401, pp. 157-182.

[9] Levich, V.G., 1962, "Physicochemical Hydrodynamics", Prentice Hall, Englewood Cliffs, NJ.

[10] Kirkpatrick, R.D., and Lockett, M.J., 1974, "The Influence of Approach Velocity on Bubble Coalescence", Chemical Engineering Science, 29, pp. 2363-2373.

[11] Kim, W.K., and Lee, K.L., 1987, "Coalescence Behavior of Two Bubbles in Stagnant Liquids", Journal of Chemical Engineering of Japan, 20, pp. 449.

[12] Miyahara, T., Matsuba, Y., Takahashi, T., 1983, "The Size of Bubbles Generated from Perforated Plates", International Chemical Engineering, 23, pp. 517.

[13] Jones, S.T., 2007, "Gas-Liquid Mass Transfer in an External Airlift Loop Reactor for Syngas Fermentation", Ph.D. Thesis, Dept. of Mechanical Engineering, Iowa State University, Ames, IA.

[14] Shah, Y.T., and Deckwer, W-D, 1983, "Hydrodynamics of Bubble Columns", Handbook of Fluids in Motion, Ann Arbor, MI: Ann Arbor Science, pp. 583-620.

CHAPTER 7. CONCLUSIONS AND FUTURE WORK

7.1. Conclusions

The gas-liquid flow dynamics in a bubble column were simulated using CFDLib in a two- dimensional Cartesian coordinate system with different grid resolutions to test the effect of using a bubble pressure model and two different drag coefficient models. The CFDLib simulations provided physical and grid-independent predictions with the experiments as the grid resolution became finer. It was shown that the BP model did not affect the flow field predictions for the high superficial gas velocity case. To improve the flow physics, the Schiller-Naumann drag coefficient model was implemented into CFDLib to compare with the existing White drag model. The drag coefficient models appeared to be sensitive to column location, where the White model worked better at low axial heights and the Schiller-Naumann model worked better at high axial heights. Finally, for the low superficial gas velocity case, the BP model was needed to model the pressure field and the BIT model added numerical stability to the system. The drag model had minimal effect on the flow predictions for a homogeneous flow field whereas the Schiller-Naumann drag model had better predictions with experiments than the White drag model for a heterogeneous flow regime.

Based on the studies for bubble column flows, an external loop airlift reactor was simulated using CFDLib in two- and three-dimensional Cartesian coordinates using the Schiller-Naumann drag model. A 3D grid generation program using plot3d format was written for the complex reactor geometry. The 3D numerical predictions agreed well with experimental data than the 2D simulations. This indicates that a 3D system is required for an external loop airlift reactor flow simulations. The approximate bubble diameter size used in

the simulations was found to be close to experimental observation and was substantiated when the simulations were performed for a 3D domain. It was concluded that when performing 2D and 3D simulations, care must be taken when specifying the effective bubble diameter size, especially at high flow rates.

Population balance models (PBM) of bubble break-up and coalescence effects were implemented into CFDLib, validated with experiments, and simulated with the external loop airlift reactor. The PBM predictions were comparable with the single bubble size simulations; however, the PBM simulations were in closer agreement with experimental observation regarding the physics of the gas bubble in the downcomer than the single bubble size simulations. The 3D PBM simulations also gave better predictions for the average bubble diameter size in the riser. To conclude, a two-fluid Eulerian-Eulerian model coupled with PBM is needed for quantitative as well as physical predictions of gas-liquid external loop airlift reactor flows. Two-dimensional gas-liquid flow simulations are recommended for simple bubble column geometry whereas three-dimensional simulations are required for the complex airlift reactor geometry. For quantitative as well as physical predictions, the PBM simulations of external loop airlift reactor flows are recommended for the high superficial gas velocity flow regime. In general, the $n = 4$ bubble size groups are able to give physical predictions for multiple bubble size simulations.

7.2. Future Work

7.2.1. Computational Simulations of Hydrodynamics for Air-KCl ELALR

External loop airlift reactors are used for synthesis gas (syngas) fermentation, which are a chemical reaction process between a mixture of gases and a non-water chemical solution to convert biomass to energy. Therefore, the computational simulations of

hydrodynamics for air-KCl ELALR are recommended. Jones [1] measured the hydrodynamics of air-KCl solution for the external loop airlift reactors. The computational simulations of hydrodynamics for air-KCl ELALR flows can be validated with experiments [1] to assess the robustness of the CFDLib code and two-phase flow model.

7.2.2. Mass Transfer Study of ELALR

Syngas fermentation is a chemical reaction process between a mixture of gases and a liquid continuum where mass transfer occurs during the process. The oxygen and carbon monoxide gas-liquid mass transfer coefficients at inlet superficial gas velocities ranging from 1 to 20 cm/s were studied by Jones [1]. The mass transfer study of an ELALR is recommended to be studied computationally with an appropriate mass diffusion coefficient model and the simulations and validate with experiments [1].

References

[1] Jones, S.T., 2007, "Gas-Liquid Mass Transfer in an External Airlift Loop Reactor for Syngas Fermentation", Ph.D. Thesis, Dept. of Mechanical Engineering, Iowa State University, Ames, IA.